

A COMPUTATIONAL MODEL FOR TILTING JOURNAL BEARINGS WITH PAD
FLEXIBILITY

A Thesis

by

YINGKUN LI

Submitted to the Office of Graduate and Professional Studies of
Texas A&M University
in partial fulfillment of the requirements for the degree of
MASTER OF SCIENCE

Chair of Committee,	Luis San Andrés
Committee Members,	Dara Childs
	Thomas Strganac
Head of Department,	Daniel McAdams

August 2015

Major Subject: Mechanical Engineering

Copyright 2015 Yingkun Li

ABSTRACT

Tilting pad journal bearings (TPJBs) supporting rotors for high performance turbomachinery have undergone steady design improvements to satisfy more stringent operating conditions that include large specific loads due to smaller footprints, and high surface speeds that produce larger drag power losses and lubricant temperature rise. Simultaneously, predictive models continuously evolve to include minute details on bearing geometry, pads and pivots' configurations, oil delivery systems, etc.

This thesis introduces a fluid film flow model including both pad and pivot flexibility to predict the static and dynamic force performance of typical TPJBs. This performance encompasses journal eccentricity, drag power loss, lubricant temperature rise, fluid film thickness, fluid film pressure, bearing complex stiffnesses, static stiffnesses, damping coefficients and virtual mass coefficients. A finite element (FE) pad structural model (with/without the Babbitt layer) is coupled to a thin film flow model to determine the mechanical deformation of the pad upper surface.

Recently, Gaines and Childs conducted experiments with three TPJB sets, each having three pads, over a range of load and rotational speed conditions. To quantify the effect of pad flexibility on the bearings' dynamic performance, the pad thickness varies from thin to thick, $t=8.5$ mm, 10 mm and 11.5mm. The test data shows that pad flexibility reduces the journal eccentricity and the dynamic force coefficients. The current model with both pad and pivot flexibility delivers predictions correlating favorably with the test data, in particular the bearing stiffnesses, yet it overestimates the bearing damping coefficients.

Predictions for bearing models available in the archival literature show that the maximum pad surface deformation occurs on the loaded pad at both its leading and trailing edges; i.e. under mechanical pressure a pad opens. The deformation at the pad mid-plane ($Z=0$) is slightly larger than that at the pad side edges ($Z=\pm 1/2 L$). Contrary to the effect of pivot flexibility that leads to an increase in journal eccentricity, pad flexibility tends to reduce the journal eccentricity, similar as in tests reported by Gaines.

A soft pad (elastic) decreases significantly the bearing stiffnesses and the damping coefficients by up to 20%.

A parametric study follows to quantify the influence of pad thickness on the rotordynamic force coefficients of two sample TPJBs: one with three pads of increasing preload, ($\bar{r}_p = 0, 0.25$ and 0.5), and another one with four pads of null preload ($\bar{r}_p = 0$). The bearing pads are either rigid or flexible by varying their thickness. For design considerations, dimensionless static and dynamic characteristics of the bearings are presented versus the Sommerfeld number (S).

An appendix introduces a one-dimensional beam equation to approximate the pad deformation accounting for the Babbitt layer. Based on this equation, a dimensionless pad flexibility parameter is defined. Pad flexibility shows a more pronounced effect on the journal eccentricity and the force coefficients of a TPJB with null pad preload than for bearings with large pad preloads (0.25 and 0.5), in particular for operation with a small load or at a high surface speed ($S > 0.8$). With the same pad preload, pad flexibility affects more the dynamic force coefficients for a load on pad (LOP) bearing than those for a load between pad (LBP) bearing.

DEDICATION

For my parents,
Jiantao Li, and Suqin Shi

ACKNOWLEDGEMENTS

First and foremost, I express my sincere gratitude to my advisor Dr. Luis San Andrés for giving me the opportunity to work at the Turbomachinery Laboratory. His patient guidance and continuous support lead me to finish my graduate studying to finally achieve my degree. His immense knowledge helped me overcome any technical problems during my research. I can think of no other better advisor and mentor I could learn from.

I also thank Dr. Dara Childs for his guidance as a professor in rotordynamics as well as a committee member. I also thank Dr. Thomas Strganac for serving as a committee member.

I sincerely appreciate my colleagues at the Turbomachinery Laboratory for their support and encouragement. Sincere thanks to Yujiao Tao for her immense help during my graduate work. I thank Jennifer Gaines for explaining with detail the test results and to give suggestions on predictions. Thanks to all Turbomachinery Laboratory staff. I sincerely thank Bethany Bowen Womack for her care and help.

Lastly and most importantly, I thank my parents, Jiantao Li and Suqin Shi, for their love and unending support through this process. I also thank my aunt, Luoping Li, for her encouragement and caring. Without them, I could not have accomplished so much.

NOMENCLATURE

A	Cross-sectional area of a pad [m^2]
C_B	Bearing radial clearance [m]
C_p	Pad radial clearance [m]
C_{XX}, C_{YY}	Bearing damping force coefficients [$\text{N}\cdot\text{s}/\text{m}$], $c=C\Omega C_p/W$
c_v	Oil specific heat
D	Bearing diameter [m]
E	Material elastic modulus [N/m^2]
E_{eq}	Equivalent elastic modulus of composite material [N/m^2]
e	Journal eccentricity [m]
e_b	Unbalance eccentricity [m] in Ref. [16]
F	Fluid film reaction force [N]
h	Fluid film thickness [m]
$h_x, h_y, h_\delta, h_\xi, h_\eta$	Perturbed film thickness components due to pad motions
I	$L^3/12$. Pad area moment of inertia [m^4]
K_{XX}, K_{YY}	Bearing stiffness force coefficients [N/m], $k=KC_p/W$
L	Bearing length [m]
M_b	Bending moment [$\text{N}\cdot\text{m}$]
M_{cp}	Bending moment at the pad's neutral axis defined in Ref. [19]
M_{XX}, M_{YY}	Bearing virtual mass force coefficients [kg] $m=M\Omega^2 C_p/W$

N	Rotor rotational speed [rev/s], $N=\Omega/60$
N_{node}	Number of nodes
N_{pad}	Number of pads
P	Pressure field acting on the pad surface [Pa]
$P_X, P_Y, P_\delta, P_\zeta, P_\eta$	Perturbed pressure fields due to pad motions [Pa/m]
P_w	Drag power loss [kw]
\bar{p}	Uniform pressure applied on a pad [Pa]
Q_s	Supply oil flow rate [LPM]
R, R_B	Bearing radius [m]
R_d	Distance from a pivot to pad center [m]
R_{eq}, R_n	Neutral axis of arc pad, single and two materials [m]
R_p	Pad radius [m]
r	$(R+t)/R$. Ratio of pad inner & outer radii
r_p	Pad dimensional preload [m], $r_p=C_P-C_B$
R_J	Journal radius [m]
S	Sommerfeld number, $S=\mu NDL(R/C_P)^2/W$
T	Fluid film temperature [°C]
$T_{Babbitt}$	Babbitt temperature [°C]
T_{back}	Temperature at the back of the pad [°C]
T_{in}	Supply oil temperature [°C]
T_{orque}	Bearing drag torque [N.m]
t	Pad thickness [m]

u_P	Pad surface nodal displacement [m]
u_t	Deformation at pad edges [m]
u	Nodal displacements [m]
W	Static load applied on the bearing [N]
Z	$K + i \omega C$. Complex dynamic stiffness coefficients [N/m]
$\tilde{Z}_{\alpha\beta}$	Fluid film complex dynamic stiffness coefficients [N/m, Nm/rad] $\alpha, \beta = X, Y, \delta, \zeta, \eta$
δ_P	Pad tilt angle [rad]
$\Delta\sigma$	Perturbation in parameter σ
ΔW	External dynamic force [N]
η_{piv}	Pad transvers displacement [m]
Θ_p	Pad arc length [rad]
θ_P	Pivot angular position starting from - X axis [rad]
θ_t	Arc length from pad pivot to pad trailing edge [rad]
λ	Inlet heat carry over coefficient
μ	Oil viscosity [Pa.s]
ζ_{piv}	Pad radial displacement [m]
ρ	Oil density [kg/m ³]
Ω	Journal rotational speed [rpm]
Ω^e	Element domain
ω	Excitation frequency [rad/s]

Coordinate Systems

(X,Y)	Journal center global coordinate
(ζ,η)	Pad pivot local coordinate
(r,θ,z)	Cylindrical coordinate of the pad finite element model

Matrices

\mathbf{A}	Matrix contacting element surfaces
$\bar{\mathbf{F}}$	Reduced external force vector
\mathbf{F}	Load vector
\mathbf{f}	Vector of forces on each node
\mathbf{K}	Pad stiffness matrix
$\bar{\mathbf{K}}$	Reduced stiffness matrix
\mathbf{L}	Lower triangular matrix of $\mathbf{K}_p = \mathbf{L}\mathbf{L}^T$
\mathbf{P}	Pressure filed
\mathbf{q}	Pivot displacement vector
\mathbf{S}	Surface traction vector
\mathbf{u}	Nodal displacement vector
$\bar{\mathbf{u}}$	Reduced pad displacement vector

Superscripts

e	Element domain
G	Global matrix
K	k^{th} pad

Subscripts

0 Static equilibrium position

p Pad upper surface

α, β, σ X, Y, δ, ξ, η

Acronyms

DOF Degree of freedom

FE Finite element

LOP Load on pad

LBP Load between pad

TPJB Tilting pad journal bearing

TABLE OF CONTENTS

	Page
ABSTRACT	ii
DEDICATION	iv
ACKNOWLEDGEMENTS	v
NOMENCLATURE.....	vi
TABLE OF CONTENTS	xi
LIST OF FIGURES.....	xiii
LIST OF TABLES	xix
INTRODUCTION.....	1
TASKS	3
LITERATURE REVIEW	4
THE FLUID FLOW MODEL FOR AN OIL LUBRICATED FLUID FILM BEARING	13
DETERMINATION OF PAD SURFACE ELASTIC DEFLECTION	16
PERTURBATION ANALYSIS.....	19
COMPARISON OF PREDICTIONS WITH PUBLICATED RESULTS FOR TEST TPJBS	23
Example 1-Predicted Forced Performance for a Three-Pad LBP TPJB [24].....	24
Example 2-Predicted Forced Performance for a Four-Pad LBP TPJB [26].....	56
CONCLUSIONS	72
REFERENCES	75
APPENDIX A- PAD DEFLECTION AND PAD STIFFNESS COEFFICIENT [35]	80

APPENDIX B-EFFECT OF PAD FLEXIBILITY ON THE FORCE
PERFORMANCE OF THREE-PAD TPJBS (LOP AND LBP CONFIGURATIONS)
AND WITH PRELOAD VARYING FROM 0, 0.25 TO 0.5 [24]..... 87

APPENDIX C-EFFECT OF PAD FLEXIBILITY ON THE FORCE
PERFORMANCE OF FOUR-PAD TPJBS WITH TWO LOAD
CONFIGURATIONS (LBP AND LOP) [26]..... 105

LIST OF FIGURES

	Page
Figure. 1 An ideal four-pad TPJB with pad tilt motion (δ) about its pivot, and pad lateral displacements along the radial (ζ) and transverse (η) directions.	5
Figure. 2 Schematic view of a typical tilting pad with pivot insert. Bending moment $M_{cp2} > M_{cp1}$. (a) before the pad contacting with the pivot insert, and (b) after the pad contacting with the pivot insert [19].	10
Figure. 3 Schematic view of an idealized TPJB. Film thickness (h), pad deflection (u_p), pad rotation (δ) and pivot deflections (ζ, η) greatly exaggerated. Copied from [31].	14
Figure. 4 Typical FE model and mesh for a bearing pad. Copied from [31].	16
Figure. 5 Boundary conditions on pad as modeled in Ref. [17]. u_r, u_θ, u_z , are the nodal displacements along the radial angular and axial directions, respectively. Copied from [31].	17
Figure. 6 Load configuration and angular disposition of each pad as per test TPJBs in Ref. [24].	23
Figure. 7 Photograph of three pads with 1.5 mm thick Babbitt layer and metal thickness noted. As per Ref.[24].	23
Figure. 8 Illustration of three pad TPJB and set up for measurement of pivot stiffness. Copied from [31].	25
Figure. 9 Pivot load versus measured deflection for pads with thickness: thin ($t=8.5\text{mm}$), medium ($t=10\text{mm}$), and thick ($t=11.5\text{mm}$). Data from Gaines [24].	26
Figure. 10 Pivot load versus <i>average</i> deflection for pads with thickness: thin ($t=8.5\text{mm}$), medium ($t=10\text{mm}$), and thick ($t=11.5\text{mm}$).	27
Figure. 11 Derived pivot stiffness versus average deflection for pads with thickness: thin ($t=8.5\text{mm}$), medium ($t=10\text{mm}$), and thick ($t=11.5\text{mm}$).	28
Figure. 12 (a) Journal eccentricity (e_y/C_p) along the load direction and (b) predicted pad maximum deformation (u_{max}/C_p) versus unit load $W/(LD)$. Journal speed $\Omega=6$ krpm and 12 krpm. Predictions (with and	

without pad flexibility) and test data from Gaines [24]. Results shown for thin, medium and thick pads.....	32
Figure. 13 Pad surface deformation. $W/(LD)=1,724$ kPa, $\Omega= 12$ krpm. Hot pad clearance for the TPJB with thin pad sets, medium thick pad sets, and thick pad sets: $C_p= 83.5 \mu\text{m}$, $82.9 \mu\text{m}$ and $81.4 \mu\text{m}$. Results shown for thin, medium and thick pads.	34
Figure. 14 Predicted and measured maximum temperature versus unit load. $\Omega=6$ krpm and 12 krpm; $W/(LD)=172$ kPa to $1,724$ kPa. Predictions from current model. Test data from Gaines [24]. Copied from [31].	35
Figure. 15 Real part of bearing complex stiffnesses, $\text{Re}(Z)$, for TPJBs with pads of thickness (a) $t=8.5$ mm (b) $t=10$ mm (c) $t=11.5$ mm. Shaft speed $\Omega=6$ krpm and unit load $W/(LD)=1,724$ kPa. Test data from Gaines [24] and predictions (with and without pad flexibility). Copied from [31].	38
Figure. 16 Real part of bearing complex stiffnesses, $\text{Re}(Z)$, for TPJBs with pads of thickness (a) $t=8.5$ mm (b) $t=10$ mm (c) $t=11.5$ mm. Shaft speed $\Omega=12$ krpm and unit load $W/(LD)=1,724$ kPa. Test data from Gaines [24] and predictions (with and without pad flexibility). Copied from [31].	40
Figure. 17 Imaginary part of bearing complex stiffnesses, $\text{Im}(Z)$, for TPJBs with pads of thickness (a) $t=8.5$ mm (b) $t=10$ mm (c) $t=11.5$ mm. Shaft speed $\Omega=6$ krpm and unit load $W/(LD)=1,724$ kPa. Test data from Gaines [24] and predictions (with and without pad flexibility). Copied from [31].	42
Figure. 18 Imaginary part of bearing complex stiffnesses, $\text{Im}(Z)$, for TPJBs with pads of thickness (a) $t=8.5$ mm (b) $t=10$ mm (c) $t=11.5$ mm. Shaft speed $\Omega=12$ krpm and unit load $W/(LD)=1,724$ kPa. Test data from Gaines [24] and predictions (with and without pad flexibility). Copied from [31].	44
Figure. 19 Direct stiffnesses (k_{XX} and k_{YY}) versus unit load and two shaft speeds. Predictions (without and with pad flexibility) and test data from Gaines [24]. Results shown for thin, medium and thick pads. Copied from [31].	48
Figure. 20 Predicted film pressure and film thickness at bearing mid plane. Operation with unit load $W/(LD)=172$ kPa and shaft speed $\Omega=6$ krpm. Location of the maximum film pressure for each pad: $\theta_1=33^\circ$ (pad 1), $\theta_2=153^\circ$ (pad 2) and $\theta_3=273^\circ$ (pad 3). Location of the	

minimum film thickness for each pad: $\theta_1=53^\circ$ (pad 1), $\theta_2=173^\circ$ (pad 2) and $\theta_3=301^\circ$ (pad 3). Copied from [31].	49
Figure. 21 Direct damping coefficients (c_{XX} and c_{YY}) versus unit load and two shaft speeds. Predictions (without and with pad flexibility) and test data from Gaines [24]. Results shown for thin, medium and thick pads. Copied from [31].	50
Figure. 22 Direct virtual mass coefficients (m_{XX} and m_{YY}) versus unit load and shaft speed= 6krpm. Predictions (without and with pad flexibility) and test data from Gaines [24]. Results shown for thin, medium and thick pads.	52
Figure. 23 Schematic view of a four-pad TPJB in Ref. [26]. Load between pads.	58
Figure. 24 FE pad model of tilting pad in Ref. [26].	60
Figure. 25 Journal eccentricity ratio (e/C_p) for example TPJB [26]. Current model predictions vs. predictions in Ref. [26]; ($\Omega=4$ krpm; $W/(LD)=688$ kPa to 3,441 kPa).	62
Figure. 26 (a) Fluid film pressure, (b) pad surface deformation, and (c) fluid film thickness. Shaft speed $\Omega=4$ krpm and static load $W/(LD)=3,441$ kPa.	64
Figure. 27 Fluid film pressure at bearing mid-plane. Current predictions. Operating preload on each pad noted. Rotor speed $\Omega=4$ krpm and unit loads $W/(LD)=1,377$ kPa, 2,065 kPa and 3,441 kPa.	65
Figure. 28 Maximum fluid film pressure for example TPJB [26]. Current model predictions vs. predictions in Ref. [26]; ($\Omega=4$ krpm; $W/(LD)=688$ kPa to 3,441 kPa).	66
Figure. 29 Maximum fluid film temperature for example TPJB [26]. Current model predictions vs. predictions in Ref. [26]; ($\Omega=4$ krpm; $W/(LD)=688$ kPa to 3,441 kPa).	67
Figure. 30 Asynchronous direct stiffness coefficients (K_{XX} and K_{YY}) for example TPJB [26]. Current model predictions vs. predictions in Ref. [26]; ($\omega=1$ krpm; $\Omega=4$ krpm; $W/(LD)=688$ kPa to 3,441 kPa).	68
Figure. 31 Asynchronous direct damping coefficients (C_{YY} and C_{YY}) for an example TPJB [26]. Current model predictions vs. predictions in Ref. [26]; ($\omega=1$ krpm; $\Omega=4$ krpm; $W/(LD)=688$ kPa to 3,441 kPa).	70

Figure. A. 1	simplified cantilevered beam model for a pivoted pad	80
Figure. A. 2	Neutral axis of a curved beam.....	82
Figure. A. 3	A curved beam made of two materials applied with bending moments (M_b): (a) shape of the curved beam (b) cross-section of the curved beam	84
Figure. B. 1	Three-pad TPJB journal eccentricity (e/C_p) and maximum pad deformation (u_{max}/C_p) vs. Sommerfeld number (S). Pad stiffness $k_{pad} = 3.15, 7.33, \infty$ (rigid) and pivot stiffness $k_{piv} = 16$. Pad preload: 0, 0.25 and 0.5. LBP and LOP configurations. Specific load $W/(LD)=689$ kPa, rotor speed $\Omega=500$ rpm to 12,000 rpm.	91
Figure. B. 2	Fluid film thickness and pad deformation at bearing mid-plane. Pad stiffness $k_{pad} = 3.15$ and pivot stiffness $k_{piv} = 16$. Pad preload $\bar{r}_p = 0.5$. LBP configurations. Specific load $W/(LD)=689$ kPa, rotor speed $\Omega=12,000$ rpm and Sommerfeld number $S=2.22$	92
Figure. B. 3	Pad surface radial deformation. Pad stiffness $k_{pad} = 3.15$ and pivot stiffness $k_{piv} = 16$. Pad preload $\bar{r}_p = 0, 0.25$ and 0.5. LOP and LBP configurations. Specific load $W/(LD)=689$ kPa, rotor speed $\Omega=12,000$ rpm ($S=2.22$).	93
Figure. B. 4	Three-pad TPJB drag friction coefficient (f) vs. Sommerfeld number (S). Pad stiffness $k_{pad} = 3.15, 7.33, \infty$ (rigid) and pivot stiffness $k_{piv} = 16$. Pad preload: 0, 0.25 and 0.5. LBP and LOP configurations. Specific load $W/(LD)=689$ kPa, rotor speed $\Omega=500$ rpm to 12,000 rpm.	95
Figure. B. 5	Three-pad TPJB stiffness coefficients (k_{XX}, k_{YY}) vs. Sommerfeld number (S). Pad stiffness $k_{pad} = 3.15, 7.33, \infty$ (rigid) and pivot stiffness $k_{piv} = 16$. Pad preload $\bar{r}_p = 0, 0.5$. LBP configuration. Specific load $W/(LD)=689$ kPa, rotor speed $\Omega=500$ rpm to 12,000 rpm [31].	97
Figure. B. 6	Three-pad TPJB stiffness coefficients (k_{XX}, k_{YY}) vs. Sommerfeld number (S). Pad stiffness $k_{pad} = 3.15, 7.33, \infty$ (rigid) and pivot stiffness $k_{piv} = 16$. Pad preload $\bar{r}_p = 0.25$. LBP and LOP configurations. Specific load $W/(LD)=689$ kPa, rotor speed $\Omega=500$ rpm to 12,000 rpm [31].	98
Figure. B. 7	Three-pad TPJB damping coefficients (c_{XX}, c_{YY}) vs. Sommerfeld number (S). Pad stiffness $k_{pad} = 3.15, 7.33, \infty$ (rigid) and pivot	

stiffness $k_{piv} = 16$. Pad preload $\bar{r}_p = 0, 0.5$. LBP configuration. Specific load $W/(LD)=689$ kPa, rotor speed $\Omega=500$ rpm to 12,000 rpm [31].	100
Figure. B. 8 Three-pad TPJB damping coefficients (c_{XX}, c_{YY}) vs. Sommerfeld number (S). Pad stiffness $k_{pad} = 3.15, 7.33, \infty$ (rigid) and pivot stiffness $k_{piv} = 16$. Pad preload $\bar{r}_p = 0.25$. LBP and LOP configurations. Specific load $W/(LD)=689$ kPa, rotor speed $\Omega=500$ rpm to 12,000 rpm [31].	101
Figure. B. 9 Three-pad TPJB virtual mass coefficients (m_{XX}, m_{YY}) vs. Sommerfeld number (S). Pad stiffness $k_{pad} = 3.15, 7.33, \infty$ (rigid) and pivot stiffness $k_{piv} = 16$. Pad preload $\bar{r}_p = 0$ and 0.5. LBP configuration. Specific load $W/(LD)=689$ kPa, rotor speed $\Omega=500$ rpm to 12,000 rpm [31].	102
Figure. B. 10 Three-pad TPJB virtual mass coefficients (m_{XX}, m_{YY}) vs. Sommerfeld number (S). Pad stiffness $k_{pad} = 3.15, 7.33, \infty$ (rigid) and pivot stiffness $k_{piv} = 16$. Pad preload $\bar{r}_p = 0.25$. LBP and LOP configurations. Specific load $W/(LD)=689$ kPa, rotor speed $\Omega=500$ rpm to 12,000 rpm [31].	103
Figure. C. 1 Four-pad TPJB journal eccentricity (e/C_p) vs. Sommerfeld number (S). Pad stiffness $k_{pad} = 4.1, 24.4, \infty$ (rigid) and pivot stiffness $k_{piv} = 8.0$. Pad preload $\bar{r}_p = 0$. LBP and LOP configurations. Specific load $W/(LD)=1,239$ kPa, rotor speed $\Omega=500$ rpm to 6,000 rpm.	108
Figure. C. 2 Pad surface radial deformation. Pad stiffness $k_{pad} = 4.1$ and pivot stiffness $k_{piv} = 8.0$. Pad preload $\bar{r}_p = 0$. LOP and LBP configurations. Specific load $W/(LD)= 1,239$ kPa, rotor speed $\Omega=6,000$ rpm ($S=2.22$).	110
Figure. C. 3 Four-pad TPJB drag friction coefficient (f) vs. Sommerfeld number (S). Pad stiffness $k_{pad} = 4.1, 24.4, \infty$ (rigid) and $k_{piv} = 8.0$. Pad preload $\bar{r}_p = 0$. LBP and LOP configurations. Specific load $W/(LD)=1,239$ kPa, rotor speed $\Omega=500$ rpm to 6,000 rpm.	111
Figure. C. 4 Four-pad TPJB dimensionless stiffnesses (k_{XX} and k_{YY}) vs. Sommerfeld number (S). Pad stiffness $k_{pad} = 4.1, 24.4, \infty$ (rigid) and pivot stiffness $k_{piv} = 8.0$. Pad preload $\bar{r}_p = 0$. LBP and LOP configurations. Specific load $W/(LD)=1,239$ kPa, rotor speed $\Omega=500$ rpm to 6,000 rpm.	113

Figure. C. 5 Four-pad TPJB dimensionless stiffnesses (k_{XX} and k_{YY}) vs. Sommerfeld number (S). Pad stiffness $k_{pad} = 4.1, 24.4, \infty$ (rigid) and pivot stiffness $k_{piv} = 8.0$. Pad preload $\bar{r}_p = 0$. LBP and LOP configurations. Specific load $W/(LD)=1,239$ kPa, rotor speed $\Omega=500$ rpm to 6,000 rpm.....	114
Figure. C. 6 Four-pad TPJB dimensionless damping coefficients (c_{XX} and c_{YY}) vs. Sommerfeld number (S). Pad stiffness $k_{pad} = 4.1, 24.4, \infty$ (rigid) and pivot stiffness $k_{piv} = 8.0$. Pad preload $\bar{r}_p = 0$. LBP and LOP configurations. Specific load $W/(LD)=1,239$ kPa, rotor speed $\Omega=500$ rpm to 6,000 rpm.....	116
Figure. C. 7 Four-pad TPJB dimensionless virtual mass coefficients (m_{XX} and m_{YY}) vs. Sommerfeld number (S). Pad stiffness $k_{pad} = 4.1, 24.4, \infty$ (rigid) and pivot stiffness $k_{piv} = 8.0$. Pad preload $\bar{r}_p = 0$. LBP and LOP configurations. Specific load $W/(LD)=1,239$ kPa, rotor speed $\Omega=500$ rpm to 6,000 rpm.....	117

LIST OF TABLES

		Page
Table 1	Percentage reduction in direct dynamic force coefficients due to both pad and pivot flexibility at two loads, Ref. [13].....	8
Table 2	Geometry, lubrication properties and operating conditions of three TPJBs tested in Ref. [24].....	24
Table 3	Thickness, mass and material properties of pads in Ref. [24].....	24
Table 4	Measured <i>pivot stiffness</i> for each pad configuration as reported by Gaines [24]	25
Table 5	Average pivot stiffness among the pivot deflection range (2 μm ~10 μm)	28
Table 6	Derived pivot stiffness for each pad configuration reported by Gaines [24]. Copied from [31].	29
Table 7	Maximum deformation of pad edge (inner surface) due to uniform contact pressure (0.7 MPa). Predictions using commercial FE software (ANSYS® and Solidworks®).	30
Table 8	Measured and predicted flow rate, measured outlet and peak temperature for the TPJBs with thin and thick pads ($t=8.5$ mm, 11.5 mm) operating at 6 krpm and 12 krpm.	36
Table 9	Correlation coefficients (r^2) of curve fit force coefficients (K, C, M) to predicted complex stiffnesses at two operating conditions for TPJBs in Ref. [24]. Excitation frequency range 0 to 200 Hz.	46
Table 10	Percentage difference between predicted dynamic force coefficients including pad flexibility and those assuming rigid pads at the lowest load ($W/(LD)=172$ kPa) and the highest load ($W/(LD)=1,724$ kPa). Frequency ranges from 0 to 200 Hz	54
Table 11	Geometry, lubrication properties and operating conditions of a four-pad TPJB in Ref. [26].....	57
Table 12	Predicted changes in bearing pad clearance due to pad thermal expansion (ΔC_B) and change in pad clearance due to pad thermal bending (ΔC_P). Data from Ref. [26]. Nominal bearing clearance $C_B=81.5$ μm , pad clearance $C_P=81.5$ μm and pad preload $\bar{r}_p=0$	61

Table A. 1	Pad geometry and material for three pads	82
Table A. 2	Deformation at pad trailing edge due to applied pressure (1 MPa).....	83
Table A. 3	Tip deformation of a pad due to an applied uniform pressure (1 MPa).....	86
Table B. 1	Parameters of a TPJB model in Ref. [24].....	88
Table B. 2	Cases to assess effect of pad flexibility on the performance of a TPJB.....	88
Table C. 1	Parameters of the four-pad TPJB presented in Ref. [26].....	106
Table C. 2	Cases to assess effect of pad flexibility on the performance of a TPJB.....	107

INTRODUCTION*

Stable performance of tilting pad journal bearings (TPJBs) in high performance rotating machinery (e.g. compressors and turbines) enables their wide application. Different from fixed geometry fluid film bearings (e.g., fixed-arc bearings and plain journal bearings), TPJBs have a number of arcuate pads distributed circumferentially around the bearing. Each pad can tilt about its pivot to generate a convergent fluid film on the pad surface. A pad cannot support a tilting moment, except for a pad with a flexure pivot [1]. However, the additional degrees of freedom (DOFs) from the bearing pads' motion, i.e., pad tilt motion, pad and pivot elastic deformations, bring more difficulty in predicting the static and dynamic forced performance of TPJBs [2, 3].

Lund [4] first introduces the pad assembly method to predict dynamic force coefficients of TPJBs by regarding the pads and their pivots as rigid. Predictions show reasonable agreement with the measurements in Ref. [5] for moderate loads. However, under heavy loads ($W/(LD)) > 2.0$ MPa) and at low rotor speeds ($\Omega < 7000$ rpm), predicted TPJB stiffness and damping coefficients show poor correlation with test data in Refs. [6-9].

Refs. [10-21] introduce various physical models and emphasize the importance of including both pad surface flexibility and pivot flexibility to accurately predict the static and dynamic forced performance of heavily loaded TPJBs. An early approach uses a beam equation to estimate pad surface elastic deflections [10-12]. Earles *et al.* [14, 15] develop a two-dimensional (2D) finite element (FE) pad model to estimate pad flexibility, but neglect pad deflections along the pad axial length. Later, Desbordes *et al.* [16] noticed that, when a rotor is operating with large unbalance displacements ($e_b/C_p=4.17$ with e_b is the unbalance eccentricity and C_p is the pad clearance), the axial

* Portion of this thesis is reprinted with permission from "Effect of Pad Flexibility on the Performance of Tilting Pad Journal Bearings - Benchmarking a Predictive Model," by San Andrés, L., and Li, Y., 2015, Proceedings of ASME Turbo Expo 2015, Paper GT2015-42776, June 15-19, Montréal, Canada, Copyright by ASME.

variation of the film thickness due to mechanical deformations is not negligible. Thus, the authors introduce a three-dimensional (3D) FE structural model to fully account for pad elastic deflections [16, 20, 21].

This work extends an existing predictive fluid film flow model, developed by San Andrés and Tao [22, 23], to account for pad flexibility, to obtain better predictions of both the static and dynamic forced performance characteristics of TPJBs.

TASKS

The predictive model is validated by comparing predictions against published test data in Ref. [24-26]. By varying the pad flexibility, a parametric study on a typical TPJB evaluates the influence of pad flexibility on the performance of TPJBs.

- (1) Build a FE structural model for prediction of pad surface elastic deformations. This procedure can be done using a commercial software to obtain the pad stiffness matrix \mathbf{K}^G . The stiffness matrix will be reduced to a reduced form \mathbf{K}_p with only a number of active degrees of freedom (DOFs) that representing nodal displacements on the pad upper surface.
- (2) Solve the Reynolds equation for fluid film lubrication and obtain the hydrodynamic pressure field by using a FE method [27].
- (3) Obtain the pad deflection from the determined fluid film pressure and the reduced stiffness matrix.
- (4) Update the fluid film thickness with the pad deflection to solve again the Reynolds equation.
- (5) Iterate steps (2) to (4) until the convergence on the fluid film pressure field and temperature is obtained.
- (6) Calculate the dynamic force coefficients of the TPJBs by applying a perturbation method of the journal center displacements.
- (7) Validate the predictions calculated in the TPJB code with published data in the literature.
- (8) Develop simplified formulas to quickly estimate pad flexibility.

LITERATURE REVIEW

Tilting pad journal bearings (TPJBs) offer significant advantages over fixed geometry fluid film bearings because they offer stable performance in high rotor speed applications. However, experiments in Refs. [6-9] show that in actuality the damping offered by TPJBs is lower than predicted. Discrepancies between predictions and measurements, in particular at heavy loads and low rotor speeds, are attributed to the predictive model not accounting for pad and pivot flexibility [13, 19, 22]. This literature review focuses on the role of pad flexibility on the performance of TPJBs, especially on the dynamic forced performance of TPJBs.

Lund [4] introduced a landmark model to calculate the stiffness and damping coefficients of TPJBs with rigid pads and rigid pivots. Based on precursor analyses for fixed pad bearings [28-29], using a procedure known as the “Pad Assembly Method,” Lund first derives the stiffness and damping coefficients for a pad; next, the dynamic force coefficients of each pad are assembled to obtain the dynamic force coefficients of the whole bearing. Lund assumes the excitation frequency (ω) coincides with the journal rotational speed (Ω). The dynamic coefficients for a whole bearing are reduced synchronously ($\omega=\Omega$) to render 2×2 matrices of stiffness and damping coefficients. The four stiffness and four damping coefficients are widely used in predictive linear rotor-bearing system analyses.

Lund [4] obtained predictions for a six-pad TPJB and a four-pad TPJB. Both TPJBs have centrally pivoted pads with $L/D=0.75$. The six-pad TPJB has pads with an arc-length of 50° while the four-pad TPJB has pads with an arc-length of 80° . Predictions for the dynamic force coefficients show reasonable correlation with test data in Ref. [5]. Lund [4] presents the dynamic force coefficients of the TPJBs versus Sommerfeld

number $(S = \frac{\mu_0 NDL}{W} \left(\frac{R}{C_p} \right)^2)$. For the four-pad TPJB, predicted direct stiffness coefficients are slightly overestimated at a low Sommerfeld number ($S < 0.3$), but are underestimated at a high Sommerfeld number ($S > 0.4$). The predicted direct damping

coefficients are larger than test data among the whole range of the Sommerfeld number ($0.1 < S < 2.2$).

Taking pivot and pad flexibility into account leads to extra degrees of freedom (DOFs) for the motion of a pad. Accounting for pivot flexibility only, each pad has three DOFs: pad tilt motion (δ) about its pivot, pad lateral displacements along the radial (ξ) and transverse (η) directions, see Figure 1. Considering the journal center displacements along both horizontal (X) and vertical (Y) directions (see Figure 1), a TPJB has a total of $(3N_{pad} + 2)$ DOFs. Thus, the complete stiffness (\mathbf{K}) and damping (\mathbf{C}) matrices of a TPJB contain $(3N_{pad} + 2)^2$ coefficients.

Including pad surface mechanical deformation adds additional DOFs. In the 1980s and early 1990s, a commonly adopted method to predict pad deformation was using one-dimensional (1D) beam equation [10-12]. Later, the FE method became popular to estimate pad mechanical deformation [13-17, 20].

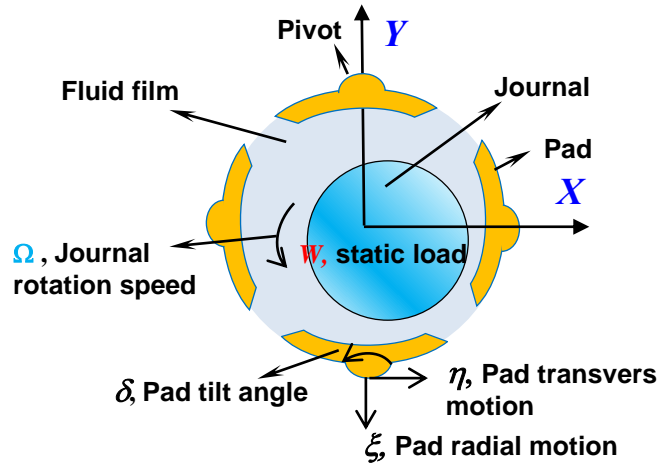


Fig. 1 An ideal four-pad TPJB with pad tilt motion (δ) about its pivot, and pad lateral displacements along the radial (ξ) and transverse (η) directions.

In 1978, Nilsson [10] studied the influence of pad flexibility on the dynamic forced performance of TPJBs. He assumes that the pad is clamped at the pivot and the

mechanical deformation of the pad can be estimated using the theory of a curved beam. Nilsson shows, in dimensionless form, single pad force coefficients for arc lengths equal to 60° , 90° and 120° and as functions of journal eccentricity. The pivot offset is 0.6 with a bearing slender ratio $L/D=1$. For a given static load, pad flexibility causes small changes in journal eccentricity and bearing stiffness coefficients. However, the influence of pad flexibility on the bearing damping coefficients is significant, especially for higher eccentricity. The long pad has a more pronounced effect on damping coefficients. At highest eccentricity ($e/C_B=0.9$), the direct damping coefficient along the load direction decreases by 50% for a 60° arc pad, and by 58% for a 120° arc pad. When reducing the eccentricity to a lower value ($e/C_B=0.5$), the direct damping coefficient along the load direction decreases by 6% for a 60° arc pad and by 21% for a 120° arc pad.

Later, Ettles [11] also predicts a reduction in bearing dynamic force coefficients due to pad flexibility. Ettles [11] accounts for pad deflections due to both the film pressure and thermally induced stresses by using a one-dimensional (1D) beam equation. Rather than using a superposition technique, Ettles considers simultaneously all the pads in a bearing. Operation under turbulent flow regime is included using Constantinescu's model [30]. Synchronous speed ($\omega=\Omega$) reduced force coefficients (including pad mass) are compared to published test data for a four-pad, load-between-pad (LBP) TPJB with $L/D=0.5$. Ettles predicts direct stiffness and damping coefficients larger, but not more than 10%, than those in published experiments. To further show the effect of pad flexibility, Ettles contrasts the dynamic force coefficients of TPJBs with rigid pads against those with flexible pads, including pad deformation due to both shear and thermal bending. The comparison reveals a reduction of damping due to pad flexibility, aggravates as the load increases: about 13% at the lowest load ($W/(LD)=307$ kPa), and about 44% at the largest load ($W/(LD)=5,020$ kPa). However, the effect of pad flexibility on bearing stiffness coefficients is smaller. Pad flexibility causes a 16% drop in stiffness coefficients at the largest load ($W/(LD)=5,020$ kPa) but a 2% increase in stiffness coefficients at the lowest load ($W/(LD)=307$ kPa). In addition, pad flexibility has negligible effect on the journal eccentricity and maximum fluid film temperature.

Lund and Pederson [12] extend the early work in Ref. [4] and present an approximate method to account for pad flexibility and pivot flexibility in the calculation of frequency reduced dynamic force coefficients of a TPJB. The authors treat the pad as an elastic beam and regard its deformation as an increase in pad clearance. The authors model pivot flexibility as a spring in series with the fluid film. The fluid film hydrodynamic pressure is determined from Reynolds equation for an isoviscous lubricant. Lund and Pederson introduce a nonsynchronous speed method, where the excitation frequency is not the same as the journal rotational speed ($\omega \neq \Omega$), to reduce the bearing dynamic coefficients into 4 stiffness and 4 damping coefficients. However, the results presented are only for synchronous speed reduced force coefficients of a single pad. The 60° pad, pivoted with 0.6 offset, has a slenderness ratio $L/D=1$. The authors notice that the reduction in damping caused by pad flexibility is most prominent. Similar to Nilsson [10], Lund and Pederson show predicted damping coefficients for pads with different pad flexibility. The authors also indicate that the more flexible a pad is, the more reduction happens in the damping coefficients. Besides, the authors also note a slight reduction in bearing load carrying capacity and bearing stiffness when pad flexibility is included in a predictive model.

Brugier and Pascal [13] investigate the influence of pad elastic deflections on both the static and dynamic forced characteristics of a large size, three-pad TPJB. Different from earlier analyses [10-12], Brugier and Pascal [13] build a three-dimensional (3D) finite element (FE) pad model to predict the mechanical deformation of the pads due to both the hydrodynamic pressure field and thermally induced stresses. The average deflections along the pad axial length of the most heavily loaded pads, as well as the respective pivot deformation, are taken into account. The authors conduct a study on TPJBs with the same geometry but different load configurations, i.e., load-on-pad (LOP) and load-between-pad (LBP). The pivot offset of the loaded pads is 0.55. The diameter of the large TPJB is 0.75 m with $L/D=0.75$. The journal rotational speed is 1,500 rpm, and the specific load ($W/(LD)$) varies from 1,190 kPa to 4,761 kPa. Though the pad is thick ($t/D=0.21$), the long arc length of the pad (104°) makes it flexible.

Predictions in Ref. [13] show that the mechanical and thermally induced deflections of both a pad and a pivot cause only a small decrease in the maximum temperature and on the minimum film thickness of a loaded pad. However, both the pad and the pivot flexibility reduce significantly the bearing dynamic force coefficients, as detailed in Table 1. For TPJBs, operating under the same load, both pad and pivot flexibility influences more the dynamic performance of a LOP TPJB than that of a LBP TPJB. Generally, the effect of pad and pivot flexibility on the bearing dynamic force coefficients increases as the load increases. However, the reduction in direct damping coefficients along the load direction (C_{YY}) does not change with an increase in load. Similar to Ettles [11], Brugier and Pascal [13] also predict an increase in direct stiffness coefficients at low loads due to both pad and pivot flexibility.

Table 1 Percentage reduction¹ in direct dynamic force coefficients due to both pad and pivot flexibility at two loads, Ref. [13].

Load configuration	Unit load [kPa]	Reduction in direct stiffness coefficients		Reduction in direct damping coefficients	
		ΔK_{XX}	ΔK_{YY}	ΔC_{XX}	ΔC_{YY}
LBP	2,381	3%	0%	21%	12%
	4,524	11%	17%	28%	12%
LOP	1,190	-15%	0%	16%	11%
	4,761	31%	30%	44%	11%

As the relevant literature in Ref. [10-13] reveals, though pad flexibility affects little the bearing static load performance, it significantly drops the damping coefficients, in particular for operation under a large load. As either the load or the pad flexibility

¹ Percentage reduction in dynamic force coefficients is obtained with respect to the predicted coefficients for TPJBs with both rigid pad and pivot.

increases, their effect change more severely the dynamic force coefficients. Thus, accurate predictions of bearing dynamic force coefficients need to take pad flexibility into account.

Neglecting the variation of the pad mechanical deformation along the axial direction, Earles *et al.* [14] use two-dimensional (2D), plane strain FE to evaluate pad flexibility effects in TPJB forced performance. The predictive model assumes a laminar, isoviscous, and incompressible lubricant without thermal effects. The pad upper surface includes N_{node} nodes. Each node has two DOFs: displacements along the radial and transverse directions. The assembled global stiffness matrix of a pad contains all $2N_{node}$ DOFs. By assuming the pad keeps its original curvature, the $2N_{node}$ DOFs are reduced to one single DOF, which is reflected as change in pad radius. Frequency-reduced dynamic force coefficients for a single pad correlate well, within 5% difference, with those obtained by Lund and Pedersen [6].

In Ref. [15], Earles *et al.* utilize the “Pad Assembly Method” to obtain the dynamic force coefficients of a TPJB. The pivot flexibility is modeled using Hertzian contact theory. Consequently, the stiffness and damping matrices contain each $(3N_{pad}+2)^2$ coefficients. The authors then conduct a stability analysis of the complete rotor bearing system with the dynamic force coefficients calculated for the bearing. Using synchronous-speed-reduced bearing dynamic coefficients, pad flexibility decreases by 6% the predicted instability onset speed (IOS) of a particular rotor-bearing system.

Refs [10-15] do not consider elastic deflections along the width of a pad. Desbordes *et al.* [17] evaluate the predictions using two-dimensional (2D) and three-dimensional (3D) FE structural pad models. The authors note that pad deflections along the axial direction are not negligible in a heavily loaded TPJB. The authors also introduce a method to constrain the pad (see Figure 5 later). The pad elastic model deliver a linear algebraic system governed by $\mathbf{K}_P \mathbf{u}_P = \mathbf{F}$, where \mathbf{K}_P is a pad stiffness matrix, \mathbf{u}_P is a vector of nodal radial displacements over the pad inner surface, and \mathbf{F} is the load vector applied on the pad. The three-pad TPJB has a diameter of 0.12 m with $L/D=0.6$, and the pivot offset is 0.56. The specific load ($W/(LD)$) applied on the bearing is 3,492 kPa and

the shaft speed is 3000 rpm (surface speed equals 18.85 m/s). The fluid film thickness and hydrodynamic pressure obtained with a 3D FE pad model and a 2D FE pad model [16] are compared against each other. Both the 2D and 3D FE pad models predict the same minimum film thickness and maximum pressure for operation with an unbalance eccentricity (e_b) smaller than 200 μm . However, when the rotor unbalance (e_b) increases, the discrepancy in results obtained from the two pad, 2D and 3D, FE models becomes evident. When $e_b=500 \mu\text{m}$, the film thickness at the edges of the loaded pad is only half of the magnitude at its midplane.

Wilkes [19] conducts both measurements and predictions for a LOP, 5-pad TPJB with 50% pad pivot offset. The diameter of the TPJB is 101.59 mm with $L/D = 0.55$. Figure 2 shows the pad and its pivot insert. The gap between the pivot and the pad leads to two different bending regions of the pad; i.e. before the pad contacts with the sides of the pivot insert, and after the pad contacts with the pivot insert. Wilkes measures the pad strain versus applied moment curvature and validates a FE pad model against measurements. Wilkes plots the pad bending stiffness versus the applied bending moment curves and obtains the bending stiffness for the pad in the test bearing. Wilkes uses the bending stiffness to predict pad flexibility and regards the pad deformation as the change in pad clearance.

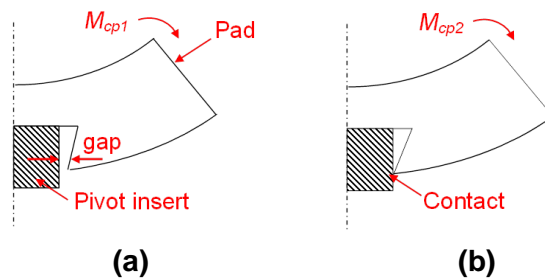


Fig. 2 Schematic view of a typical tilting pad with pivot insert. Bending moment $M_{cp2} > M_{cp1}$. (a) before the pad contacting with the pivot insert, and (b) after the pad contacting with the pivot insert [19].

Wilkes [19] notes the importance of pad flexibility in predicting TPJB dynamic coefficients. Wilkes compares measurements against the predicted results obtained from a model with and without the consideration of both pad and pivot flexibility. The comparisons show that pivot flexibility affects more the predictions of direct stiffness and damping coefficients than pad flexibility, especially at high loads. Pad and pivot flexibility have a large effect on reducing the bearing damping coefficients. At a rotor speed of 10,200 rpm (surface speed $\Omega R/60=54.2$ m/s) with a unit load ($W/(LD)$) of 783 kPa, predictions including pivot flexibility but neglecting pad flexibility overestimate the direct stiffness coefficients by up to 8% and overestimate the direct damping coefficients by up to 42%. At the same rotor speed with a larger unit load ($\Omega=10,200$ rpm, $W/(LD)=3,134$ kPa), predictions including pivot flexibility but neglecting pad flexibility overestimate the direct stiffness coefficients by up to 41% and overestimate the direct damping coefficients by up to 57%. Thus, predictions show that pad flexibility has a more pronounced effect under large loads for this bearing. In addition, Wilkes indicates that since pad flexibility increases with the arc length of a pad, it may play a more important role in TPJBs of large arc size or fewer pads. Notably, Wilkes measures the bearing clearance right after the operation and notes that hot bearing clearance can be up to 30% smaller than the bearing clearance at room temperature.

Hagemann *et al.* [20] conduct both measurements and predictions of the static performance of a large turbine TPJB operating under a LBP load configuration. The 5-pad TPJB has a diameter of 500 mm with $L/D = 0.7$ and the pad pivot offset is 60%. The preload of the TPJB is 0.23 and the unit load ($W/(LD)$) on the TPJB varies from 1,000 kPa to 2,503 kPa. The rotational speed ranges from 500 rpm to 3,000 rpm. The theoretical analysis considers a 3D viscosity and pressure distribution due to the variable temperature in all three (circumferential, axial and radial) directions of the film. The authors use two different methods, by regarding the pad as 1D beam and 3D FE model, to determine the thermo-mechanical deflection of the pad. The deflection of the pad is considered as the change in film thickness. Similar to Desbordes *et al.* [17], Hagemann *et al.* also notice the variation of pad deformations along the bearing width. For a unit

load of 2,503 kPa and a rotor speed of 3000 rpm, the film thickness measured at the bearing mid-plane ($z=L/2$) is about 70 μm (23% of the bearing clearance) larger than that measured at the edges ($z=0$ and $z=L$). Comparisons between measurements and predictions using the two methods (i.e., 3D FE pad and 1D beam equation) demonstrate the necessity to consider the 3D deflections of a pad. Predictions using 3D FE structural model correlate best with the test data.

Kukla *et al.* [21] extend their work and present measured dynamic force coefficients of a five-pad TPJB with the same geometry as described in Ref. [20]. However, their predictions for dynamic force coefficients do not account for pad flexibility.

Recently, Gaines and Childs [24, 25] tested three TPJB sets under a LBP configuration over a range of loads ($172 \text{ kPa} < W/(LD) < 1,724 \text{ kPa}$) and rotational speed conditions ($6 \text{ krpm} < \Omega < 12 \text{ krpm}$). Each bearing has three pads of unequal thickness ($t=8.5 \text{ mm}$, 10 mm , and 11.5 mm) to quantify the effect of pad flexibility on the bearings' force coefficients. As pad flexibility increases, the measured journal eccentricity decreases. However, pad flexibility shows little effect on the measured pad sub-surface temperature ($\sim 5 \text{ mm}$ below) recorded at 75% of the pad arc length. Increasing pad flexibility increases the measured direct stiffnesses by up to 12% at a low load ($W/(LD)=172 \text{ kPa}$), but decreases the measured direct stiffnesses by up to 3% at the largest applied load ($W/(LD)= 1,724 \text{ kPa}$). Pad flexibility shows a more pronounced effect on the bearing damping coefficients, as it reduces their magnitude by up to 20% at 12krpm and by up to 15% at 6krpm.

Based on the body of literature reviewed, pad flexibility affects little the static forced performance of TPJBs. However, for TPJBs operating under a heavy load ($W/(LD)>2.0 \text{ MPa}$), pad (and/or pivot) flexibility can produce a significantly reduction in the dynamic force coefficients, in particular bearing damping coefficients.

THE FLUID FLOW MODEL FOR AN OIL LUBRICATED FLUID FILM BEARING

San Andrés [27] introduces an analysis for static and dynamic load in TPJBs and including pivot flexibility. This section extends the analysis for TPJBs with pad flexibility. Figure 3 shows a schematic view of an idealized TPJB comprised of a rotating journal and a number of arcuate pads tilting about respective pivots. A film of lubricant fills the clearance between the pads and journal. The origin of the (X, Y) inertial coordinate system locates at the bearing center, whereas various local coordinates (ζ, η) system are affixed to (undeformed) each pivot. The figure intends to portray a pad on its assembled configuration and also as loaded during operation.

An external load (W) applies on the journal spinning with rotational speed (Ω). The load forces the journal displacement to eccentricity (e_X, e_Y) away from the bearing center. The applied load is reacted by the generated fluid film hydrodynamic pressure (P) acting on each pad. The pressure field on the pad surface also generates a moment that tilts the pad about its pivot with rotation δ_p and displaces the pad pivot to ξ_{piv} and η_{piv} . The pressure field also deforms elastically the pad; in particular, the deformation field at the pad surface is denoted by u_p .

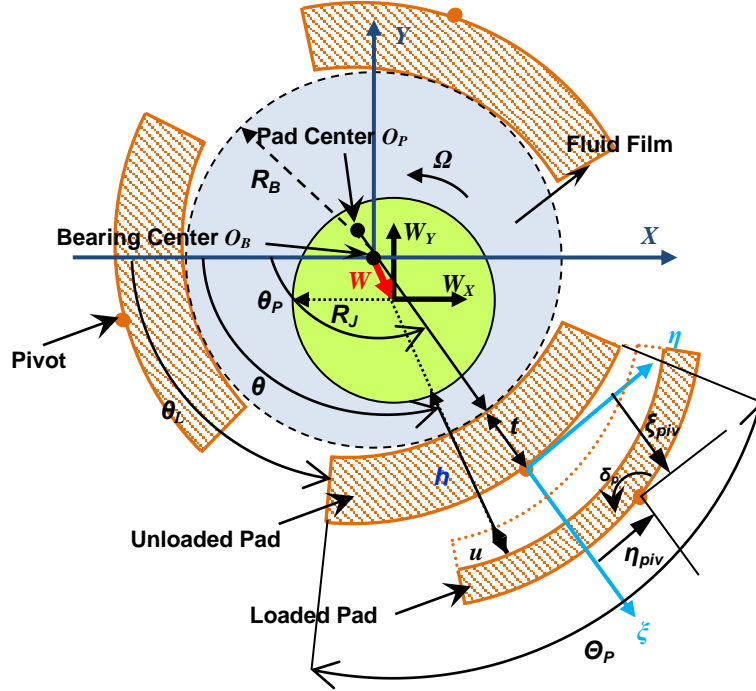


Fig. 3 Schematic view of an idealized TPJB. Film thickness (h), pad deflection (u_p), pad rotation (δ) and pivot deflections (ξ, η) greatly exaggerated. Copied from [31].

San Andrés and Tao [22] state the governing equations and method to solve for the pressure field (P) and temperature field (T) in a laminar-flow TPJB lubricated with a fluid of viscosity (μ) and density (ρ). An extended Reynolds equation with temporal fluid inertia effects governs the generation of hydrodynamic pressure (P^k) in the k^{th} pad with film thickness h^k ,

$$\frac{1}{R_j^2} \frac{\partial}{\partial \theta} \left\{ \frac{(h^k)^3}{12\mu_{(T)}} \frac{\partial P^k}{\partial \theta} \right\} + \frac{\partial}{\partial z} \left\{ \frac{(h^k)^3}{12\mu_{(T)}} \frac{\partial P^k}{\partial z} \right\} = \frac{\partial h^k}{\partial t} + \frac{\Omega}{2} \frac{\partial h^k}{\partial \theta} + \frac{\rho (h^k)^2}{12\mu_{(T)}} \frac{\partial^2 h^k}{\partial t^2}, k = 1, \dots, N_{pad} \quad (1)$$

where (z, θ) are the axial and circumferential coordinates on the plane of the bearing. The film thickness h^k is

$$h^k = u_p^k + C_p + e_x \cos \theta + e_y \sin \theta + (\xi_{piv}^k - r_p) \cos(\theta - \theta_p^k) + (\eta_{piv}^k - R_d \delta_p^k) \sin(\theta - \theta_p^k) \quad (2)$$

where (e_x, e_y) are the journal center displacements, $r_p = C_p - C_B$ is the pad preload, and C_p and C_B are the pad machined radial clearance and bearing assembly clearance, respectively. Above $R_d = R_p + t$ is the sum of the pad machined radius and pad thickness at the pivot position. Note that the pad surface deflection field ($u_p^k > 0$) increases the film thickness.

DETERMINATION OF PAD SURFACE ELASTIC DEFLECTION

A structural FE analysis predicts the displacements of the k^{th} pad upper surface caused by the fluid film pressure field (P). Figure 4 depicts a typical pad assembling a number of brick-like finite elements. The equation for the deflection field (\mathbf{u}^G) relative to the pivot due to an applied load (\mathbf{F}^G) is

$$\mathbf{K}^G \mathbf{u}^G = \mathbf{F}^G + \mathbf{S}^G \quad (3)$$

where \mathbf{K}^G is a global stiffness matrix and \mathbf{S}^G is a vector of surface tractions.

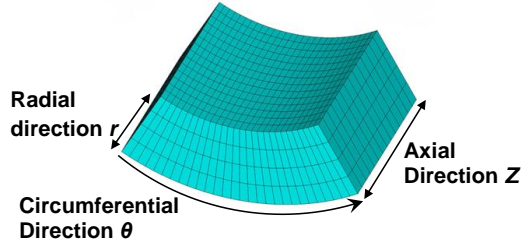


Fig. 4 Typical FE model and mesh for a bearing pad. Copied from [31].

Desbordes *et al.* [17] introduce appropriate boundary conditions for an ideal tilting pad, i.e., one with infinite pivot stiffness. Figure 5 depicts in graphical form the lines where boundary conditions are specified. The solid line denotes the pivot (line contact) and all FE nodes are constrained to a null displacement; $u_r = u_\theta = u_z = 0$, along the radial, circumferential, and axial directions. The two dashed lines parallel to the line contact denote nodes with no radial displacement, $u_r = 0$ only relative to the pivot displacement. On these lines, the nodes can take circumferential (transverse) and axial displacements.

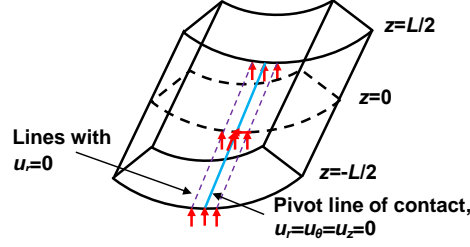


Fig. 5 Boundary conditions on pad as modeled in Ref. [17]. u_r , u_θ , u_z , are the nodal displacements along the radial angular and axial directions, respectively. Copied from [31].

With the boundary conditions assigned, the global system of equations reduces to

$$\bar{\mathbf{K}}^G \bar{\mathbf{u}}^G = \bar{\mathbf{F}}^G \quad (4)$$

where $\bar{\mathbf{K}}^G$ is a reduced (non-singular) stiffness matrix, and $\bar{\mathbf{u}}^G$ and $\bar{\mathbf{F}}^G$ are the vectors of global displacements and forces. The external load generated by the film pressure acts on the (upper) surface of the pad. Thus, further manipulation to reduce Eq. (4) uses a static condensation or *Guyan* reduction procedure. Write the vectors of displacements and generalized force in terms of active and inactive degrees of freedom, i.e.,

$$\bar{\mathbf{u}}^G = \begin{Bmatrix} \mathbf{u}_p \\ \bar{\mathbf{u}} \end{Bmatrix}; \quad \bar{\mathbf{F}}^G = \begin{Bmatrix} \mathbf{f}(P) \\ \mathbf{0} \end{Bmatrix} \quad (5)$$

where \mathbf{u}_p denotes the vector of radial displacements on the pad upper surface which are active DOFs, and $\bar{\mathbf{u}}$ is the vector of displacements of other nodes, $\mathbf{f}(P)=\mathbf{A}\mathbf{P}$ is the vector of nodal forces generated by the pressure field \mathbf{P} with \mathbf{A} as a square matrix containing element surfaces. The reduced global stiffness matrix $\bar{\mathbf{K}}^G$ can be partitioned as

$$\bar{\mathbf{K}}^G = \begin{bmatrix} \bar{\mathbf{K}}_p & \bar{\mathbf{K}}_s \\ \bar{\mathbf{K}}_s & \bar{\mathbf{K}}_{na} \end{bmatrix} \quad (6)$$

With these definitions, Eq. (4) can be written as

$$\begin{cases} \bar{\mathbf{K}}_p \mathbf{u}_p + \bar{\mathbf{K}}_s \bar{\mathbf{u}} = \mathbf{f}(P) \\ \bar{\mathbf{K}}_s \mathbf{u}_p + \bar{\mathbf{K}}_{na} \bar{\mathbf{u}} = \mathbf{0} \end{cases} \quad (7)$$

From Eq. (7), $\bar{\mathbf{u}} = -\bar{\mathbf{K}}_{na}^{-1} \bar{\mathbf{K}}_s \mathbf{u}_p$ and displacements on the pad surface are obtained from

$$\mathbf{K}_p \mathbf{u}_p = \mathbf{f}(P) \quad (8)$$

where $\mathbf{K}_p = \bar{\mathbf{K}}_p - \bar{\mathbf{K}}_s [\bar{\mathbf{K}}_{na}]^{-1} \bar{\mathbf{K}}_s$ is a positive definite symmetric matrix, easily decomposed into its lower and upper triangular forms, $\mathbf{K}_p = \mathbf{L}\mathbf{L}^T$. Hence, Eq. (8) is rewritten as

$$\mathbf{L} \mathbf{L}^T \mathbf{u}_p = \mathbf{f}(P) \quad (9)$$

Let $\mathbf{u}_p^* = \mathbf{L}^T \mathbf{u}_p$; a backward substitution procedure solves first $\mathbf{L} \mathbf{u}_p^* = \mathbf{f}(P)$ to give \mathbf{u}_p^* ; and next, a forward substitution procedure solves $\mathbf{L}^T \mathbf{u}_p = \mathbf{u}_p^*$ to determine \mathbf{u}_p , i.e., the vector of radial displacement at the pad surface. The vector \mathbf{u}_p is used to update the film thickness (h), Eq. (2), for solution of the Reynolds Eq. (1) to find the pressure field (P). Note that the FE structural pad model and its end result, the \mathbf{L} matrix, needs to be performed only once, preferably outside of the main computational program.

A pivot with known load-dependent nonlinear stiffness is easily considered as a series element with the pad structural stiffness.

PERTURBATION ANALYSIS

Accounting for pivot flexibility, San Andrés and Tao [22, 23, 27] presents the analysis for evaluation of dynamic force coefficients in TPJBs. The current work will introduce a modified perturbation analysis accounting for pad flexibility.

At a constant shaft speed (Ω), the static $\mathbf{W}_0 = (W_{X_0}, W_{Y_0})$ load T displaces the journal to its equilibrium position $\mathbf{e}_0 = (e_{X_0}, e_{Y_0})^T$ with the generated fluid film pressure (P_0^k) acting on each pad surface. The k th pad reaches its equilibrium position $(\delta_{p_0}^k, \xi_{piv_0}^k, \eta_{piv_0}^k)^T$ and the deflection of the pad upper surface is $u_{p_0}^k$.

An external dynamic force, $\Delta \mathbf{W} = (\Delta W_X, \Delta W_Y)^T e^{i\omega t}$ with excitation frequency (ω) acts on the journal and causes the journal center to displace to $\Delta \mathbf{e} = (\Delta e_X, \Delta e_Y)^T e^{i\omega t}$ away from \mathbf{e}_0 , i.e., $\mathbf{e}_{(t)} = \mathbf{e}_0 + \Delta \mathbf{e} e^{i\omega t}$ [22, 23, 27]. The journal motion leads to changes in the pad pivot displacements and the pad surface deformation as

$$(\delta_p^k, \xi_{piv}^k, \eta_{piv}^k)^T = (\delta_{p_0}^k, \xi_{piv_0}^k, \eta_{piv_0}^k)^T + (\Delta \delta_p^k, \Delta \xi_{piv}^k, \Delta \eta_{piv}^k)^T e^{i\omega t} \quad (10a)$$

$$u_p^k = u_{p_0}^k + \Delta u_p^k e^{i\omega t}, \quad k = 1, \dots, N_{pad} \quad (10b)$$

On the k^{th} pad, the changes in journal center position and pad displacements cause a change in the film thickness as

$$h^k = h_0^k + \Delta h^k e^{i\omega t}, \quad k = 1, \dots, N_{pad} \quad (11a)$$

where

$$\Delta h^k = \{h_x^k \Delta e_X + h_y^k \Delta e_Y + h_\xi^k \Delta \xi_{piv}^k + h_\eta^k \Delta \eta_{piv}^k + h_\delta^k \Delta \delta_p^k + \Delta u_p^k\} \quad (11b)$$

with $h_x^k = \cos \theta$, $h_y^k = \sin \theta$, $h_\xi^k = \cos(\theta - \theta_p^k)$, $h_\eta^k = \sin(\theta - \theta_p^k)$, $h_\delta^k = -R_d h_\eta^k$ [27]. The fluid film pressure on a pad is

$$P^k = P_0^k + \Delta P^k e^{i\omega t}, \quad k = 1, \dots, N_{pad} \quad (12a)$$

where the change in fluid film pressure caused by the perturbations in displacements is

$$\Delta P^k = \{P_X^k \Delta e_X + P_Y^k \Delta e_Y + P_\xi^k \Delta \xi_{piv}^k + P_\eta^k \Delta \eta_{piv}^k + P_\delta^k \Delta \delta_p^k\} \quad (12b)$$

Let $\mathbf{g}(P^k) = [\mathbf{K}_p^k]^{-1} \mathbf{f}(\mathbf{P}^k)$. Hence, the pad deformations caused by the equilibrium pressure field \mathbf{P}_0^k and the perturbed pressure field ($\Delta \mathbf{P}^k$) are

$$\mathbf{u}_{\mathbf{P}_0^k}^k, \Delta \mathbf{u}_{\mathbf{P}}^k = \mathbf{g}(P_0^k), \mathbf{g}(\Delta P^k) \rightarrow [\mathbf{K}_p^k]^{-1} \mathbf{A} \mathbf{P}_0^k, [\mathbf{K}_p^k]^{-1} \mathbf{A} \Delta \mathbf{P}^k \quad (13)$$

Substituting Eq. (12b) into Eq. (13) yields the change in pad surface deformation as

$$\Delta u_p^k = u_x^k \Delta e_x + u_y^k \Delta e_y + u_\delta^k \Delta \delta_p^k + u_\xi^k \Delta \xi_{piv}^k + u_\eta^k \Delta \eta_{piv}^k \quad (14)$$

Thus,

$$\begin{aligned} \Delta h^k &= (h_x^k + u_x^k) \Delta e_x + (h_y^k + u_y^k) \Delta e_y + (h_\xi^k + u_\xi^k) \Delta \xi_{piv}^k \\ &\quad + (h_\eta^k + u_\eta^k) \Delta \eta_{piv}^k + (h_\delta^k + u_\delta^k) \Delta \delta_p^k \end{aligned} \quad (15)$$

That is, the film thickness changes due to physical displacements of the journal and pad as well as due to the deformation induced by a change or perturbation in pressure.

Define the following linear operators,

$$\ell(*) = \frac{\partial}{R \partial \theta} \left[\frac{h_0^3}{12\mu} \frac{\partial(*)}{R \partial \theta} \right] + \frac{\partial}{\partial z} \left[\frac{h_0^3}{12\mu} \frac{\partial(*)}{\partial z} \right] = \vec{\nabla} \left(\frac{h^3}{12\mu_{(r)}} \vec{\nabla} (*) \right) \quad (16)$$

$$\mathfrak{R}(*) = \left[\frac{\Omega}{2} \frac{\partial(*)}{\partial \theta} + i\omega(*) - \frac{\rho h_0^2}{12\mu_{(r)}} \omega^2(*) \right] - \vec{\nabla} \left(\frac{3h_0^2}{12\mu_{(r)}} (*) \vec{\nabla} P_0 \right) \quad (17)$$

Substitution of h^k and P^k into the extended Reynolds Eq. (1) gives:

$$\ell(P_0) = \frac{\Omega}{2} \frac{\partial h_0}{\partial \theta} \quad (18)$$

and

$$\ell\{P_\sigma^k\} = \mathfrak{R}\{h_\sigma^k + u_\sigma^k\}_{\sigma=X,Y,\delta,\xi,\eta} \quad (19)$$

Note that the first-order or perturbed pressure fields due to a pad rotation and pivot radial and transverse displacements are a linear combination of P_X and P_Y [22, 23, 27], i.e.,

$$\begin{aligned} P_\delta^k &= -R_j P_\eta^k \\ P_\xi^k &= P_X^k \cos \theta_p^k + P_Y^k \sin \theta_p^k, \quad k = 1, \dots, N_{pad} \\ P_\eta^k &= -P_X^k \sin \theta_p^k + P_Y^k \cos \theta_p^k \end{aligned} \quad (20)$$

Since the pad deformations are a linear function of the applied pressure, i.e., $u_\sigma^k = g(P_\sigma^k)$ with $\sigma = X, Y, \delta, \xi, \eta$, then

$$\begin{aligned} u_\delta^k &= -R_J u_\eta^k \\ u_\xi^k &= u_X^k \cos \theta_P^k + u_Y^k \sin \theta_P^k, \quad k = 1, \dots, N_{pad} \\ u_\eta^k &= -u_X^k \sin \theta_P^k + u_Y^k \cos \theta_P^k \end{aligned} \quad (21)$$

The analysis above reveals that the perturbed pressure fields due to pad rotation or pivot transverse displacements can be readily gathered from the fields determined for changes in the journal eccentricity ($\Delta e_X, \Delta e_Y$). Furthermore, the changes in pad deformation also follow immediately after the perturbed displacements (u_X^k, u_Y^k) are found. The process is computationally fast and efficient. The only caveat is that Eq. (19) is solved iteratively, as $u_\sigma^k = g(P_\sigma^k)_{\sigma=X,Y}$.

In the procedure to calculate a perturbed pressure field, Eq. (19) is to be solved iteratively.

- (a) Set $\mathbf{u}_\sigma = 0$. Determine the \mathbf{P}_σ vector from $\ell(P_\sigma^k) = \Re(h_\sigma^k)$.
- (b) Calculate $\mathbf{u}_\sigma^k = \mathbf{g}(P_\sigma^k)$.
- (c) Solve $\ell(P_\sigma^k) = \Re(h_\sigma^k + u_\sigma^k)$.

The procedure (b)-(c) is repeated until obtaining a \mathbf{P}_σ vector that does not change from the prior iteration. Integration of the perturbed pressure fields, renders 25 fluid film dynamic complex stiffness coefficients ($\tilde{Z}_{\alpha\beta}^k$) [22, 23, 27]

$$\tilde{Z}_{\alpha\beta}^k = \int_{-L/2}^{L/2} \int_{\theta_P^k}^{\theta_r^k} P_\beta^k h_\alpha^k R_J d\theta^k dz, \quad \alpha, \beta = X, Y, \delta, \xi, \eta \quad (22)$$

Reduced frequency force coefficients for lateral displacements, $Z_{a\beta}=(K_{a\beta}+i\omega C_{a\beta})$ $a,\beta=X,Y$, are extracted from the complete sets of 25 Z 's by assuming all pads move with the same frequency ω . For details on the reduction process, see Refs. [22, 23, 27].

COMPARISON OF PREDICTIONS WITH PUBLISHED RESULTS FOR TEST TPJBS

There are two relevant publications of importance to the current work, Refs.[24,26]. The current predictive model delivers predictions for comparison against the data in these references. Gaines [24] reports test data for three TPJB sets, each having three pads of unequal thickness, to quantify the effect of pad flexibility on the bearings' force coefficients over a range of applied load (LBP) and rotational speed conditions. Branagan [26] reports predictions for several bearings, one being a four-pad TPJB with a LBP configuration. The predictions account for both pad thermal bending and pad mechanical bending over a range of loads with operation at a constant shaft rotational speed.

Predicted TPJBs forced performance characteristics of interest include the static journal eccentricity, fluid film temperature, fluid film pressure, pad surface deformation and dynamic force coefficients, e.g. stiffness, damping, and virtual mass coefficients. Assessing the correlation between current predictions and the data in Refs. [24,26] aids to validate the predictive model. Predictions with and without pad flexibility will evidence quantitatively the effect of pad flexibility.

Example 1-Predicted Forced Performance for a Three-Pad LBP TPJB [24]

Gaines [24] presents test data for three TPJBs, each configuration having three pads and operating under the same conditions. The pad thickness varies in each bearing configuration. This section presents comparison of the predicted and measured [24] static and dynamic forced performance characteristics of Gaines' test bearings, and investigates the effect of pad flexibility on bearing behavior. Table 2 lists the geometry of the TPJBs, lubricant properties and operation conditions, and Figure 6 depicts the load configuration of a test TPJB.

Table 2 Geometry, lubrication properties and operating conditions of three TPJBs tested in Ref. [24].

Number of pads, N_{pad}	3		
Configuration	LBP		
Rotor diameter, D	101.6 mm		
Pad axial length, L	61 mm		
Pad arc angle, θ_P	90°		
Pivot offset	50%		
Nominal preload, \bar{r}_p	0.25		
Pad thickness, t	8.5mm	10 mm	11.5mm
Cold bearing clearance, C_B	69 μm	70 μm	70 μm
Cold pad clearance, C_P	92 μm	93 μm	93 μm
Lubricant type	ISO VG 46		
Supply lubricant temperature	49 °C		
Supply lubricant pressure	2.2 bar		
Lubricant density	854 kg/m ³		
Viscosity at 49 °C ¹ , μ_0	0.0269 Pa·s		
Viscosity temperature coefficient, α	0.0319 1/°C		
Specific heat capacity at 70 °C	1830 J/(kg·K)		
Specific load, $W/(LD)$	172 kPa -1724 kPa		
Journal speed, Ω	6,000-12,000 rpm		
Surface speed, ΩR	32-64 m/s		

¹ The lubricant used in test cell is ISO VG46. The oil viscosity is measured using a viscometer.

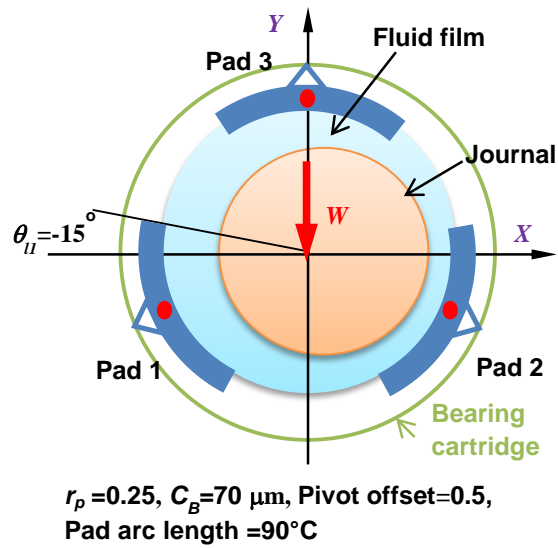


Fig. 6 Load configuration and angular disposition of each pad as per test TPJBs in Ref. [24].

As shown in Figure 7, the pad thickness varies from 8.5 mm to 11.5 mm, thus modifying the pad flexibility. Table 3 lists the thickness, mass and material properties of the three pads. The arc length and inner radius of the three pads are identical. Note that each pad includes a 1.5 mm thick Babbitt layer.

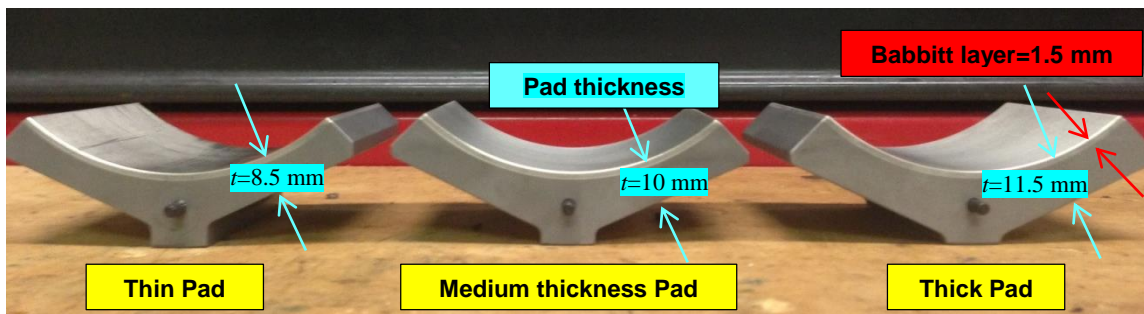


Fig. 7 Photograph of three pads with 1.5 mm thick Babbitt layer and metal thickness noted. As per Ref.[24].

Table 3 Thickness², mass and material properties of pads in Ref. [24]

	Pad thickness [mm]	Pad mass ³ [kg]	Pad moment of inertia [kg·cm ²]	Elastic modulus ⁴ [GPa]		Poisson's ratio [-]	
				Metal	Babbitt	Metal	Babbitt
Thin pad	8.5	0.42	3.57	200	50	0.29	0.33
Medium thickness pad	10	0.48	4.20				
Thick pad	11.5	0.54	4.86				

Gaines [24] measures the force performance of three tilting pad journal bearings (TPJBs), all having similar geometry and configuration but differing in pad thickness. To measure the pivot stiffness of a single pad, a bearing is assembled in the LOP orientation (see Figure 8). A hydraulic cylinder and spring pull on the bearing casing and displace it against a rigid rotor (journal). The applied load on the shaft is through contact pressure over the whole pad arc extent.

Eddy current sensors (rotor-stator probes), at both the drive end and the non-drive end of the bearing, record the relative displacements between the stator-bearing assembly and the journal or shaft [24]. The recorded displacements represent the pad and pivot elastic deflection. The data below represents the average of the displacements measured at both ends (drive and non-drive).

² Pad thickness includes 1.5 mm Babbitt layer.

³ Pad mass of each pad is measured value, and the pad moment of inertia is estimated from Solidworks©.

⁴ Metal and Babbitt material properties are from Ref. [33].

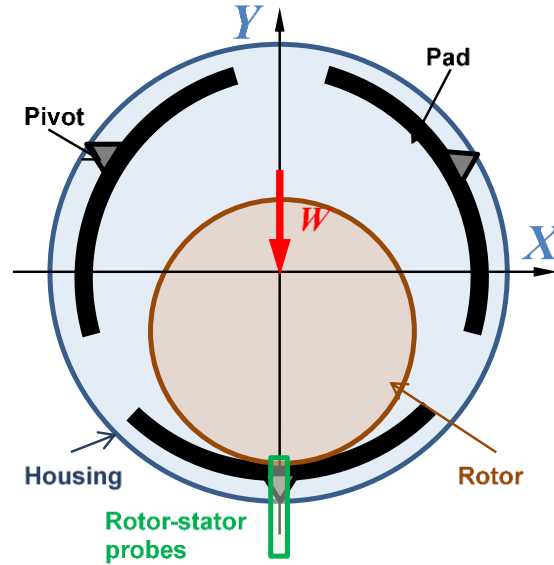


Fig. 8 Illustration of three pad TPJB and set up for measurement of pivot stiffness. Copied from [31].

Table 4 lists the *pivot stiffness* reported by Gaines [24] for the three pads differing in thickness. The pads have the same pivot type; and hence, their pivot stiffness must be (nearly) the same. However, note the *pivot stiffnesses* are markedly different.

Table 4 Measured *pivot stiffness* for each pad configuration as reported by Gaines [24]

	<i>Pivot stiffness</i> [MN/m]
Thin pad ($t=8.5$ mm)	505
Medium thickness pad ($t=10$ mm)	664
Thick ($t=11.5$ mm)	751

Figure 9 shows the applied load versus measured deflection curves obtained from the data delivered by Gaines [24]. Note there is a nonlinear relationship between load and

pivot deflection; first a soft region with very low stiffness⁵, followed by an elastic region with a hardening stiffness for loads from 2 kN to 4 kN. In addition, the test data shows mechanical hysteresis.

For the medium thickness pad ($t=10$ mm) and the thickest pad ($t=11.5$ mm), the slopes of the load vs. (average) deflection curves are 664 MN/m and 751 MN/m, respectively, in the load range 2 kN to 4 kN. These magnitudes are similar as those reported by Gaines [24]. For the thin pad ($t=8.5$ mm), the slope of the load vs. deflection curve is about 1,000 MN/m, almost twice as large as that selected by Gaines [24].

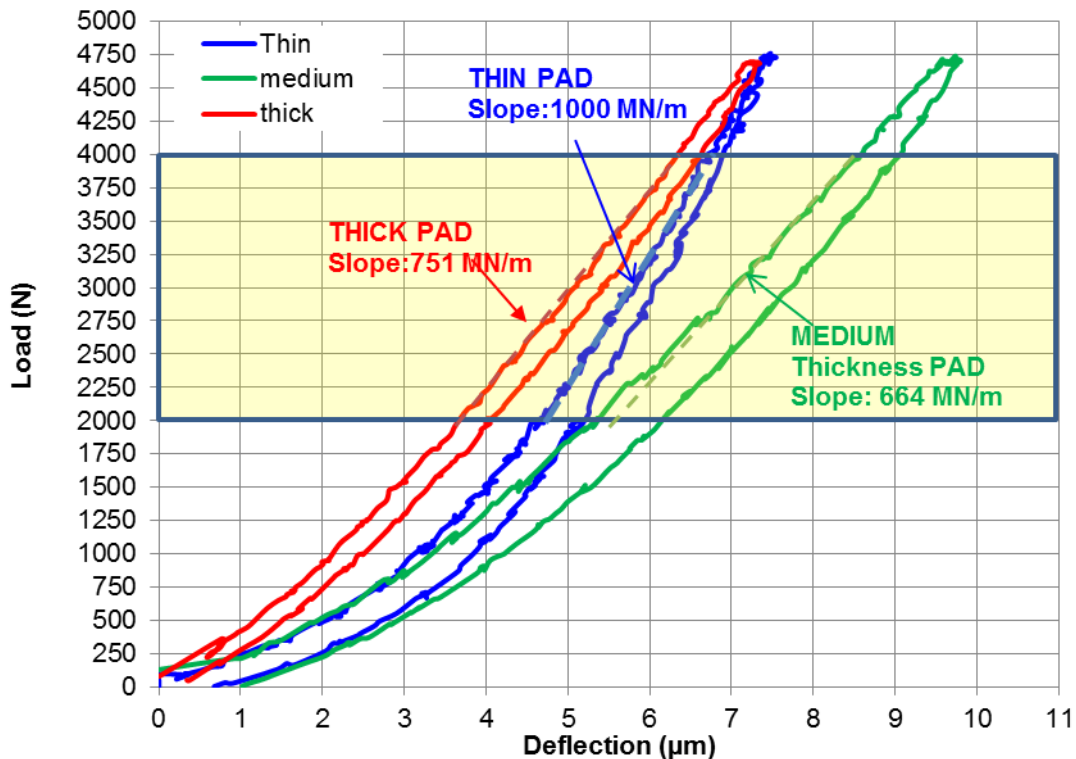


Fig. 9 Pivot load versus measured deflection for pads with thickness: thin ($t=8.5$ mm), medium ($t=10$ mm), and thick ($t=11.5$ mm). Data from Gaines [24].

⁵ Not due to Babbitt deformation as FE structural model predictions show.

Figure 10 shows the applied load versus (measured) average⁶ displacement curves and trend lines with a power curve fit. Selecting the average displacements from the load and unload processes removes the hysteresis effect.

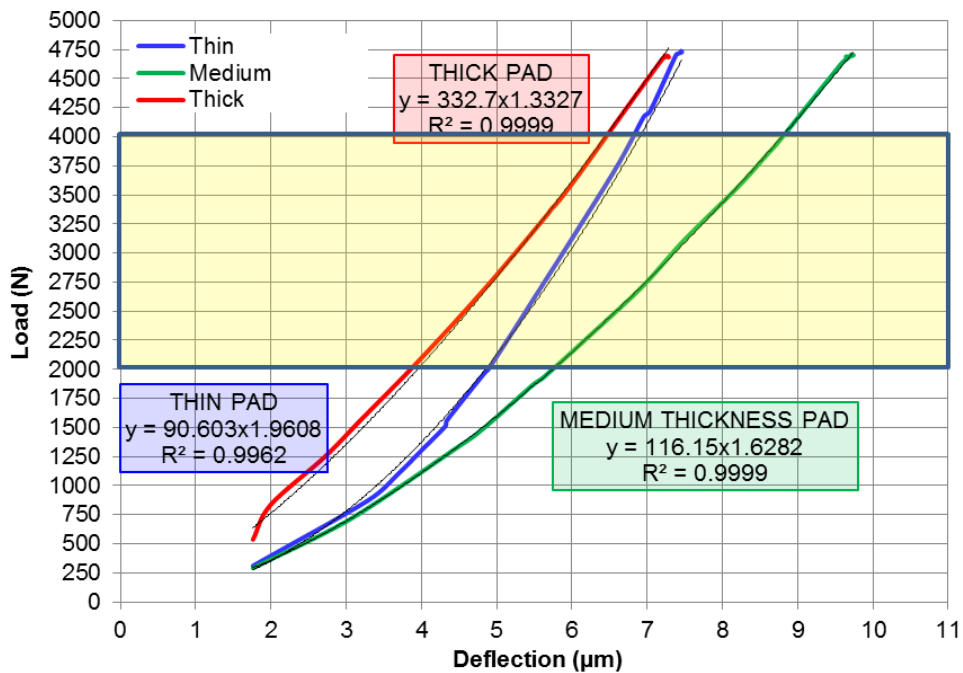


Fig. 10 Pivot load versus *average* deflection for pads with thickness: thin ($t=8.5\text{mm}$), medium ($t=10\text{mm}$), and thick ($t=11.5\text{mm}$).

Figure 11 depicts the slope of the curves in Figure 10, i.e. the *pivot stiffness* as a function of the deflection. Note the derived pivot stiffness increases with the *pivot* displacement. Interestingly, the *pivot stiffness* for the thin pad ($t=8.5\text{ mm}$) is larger than those for the thick pad ($t=11.5\text{ mm}$) and medium thickness pad ($t=10\text{ mm}$).

⁶ Average from the load and unload cases.

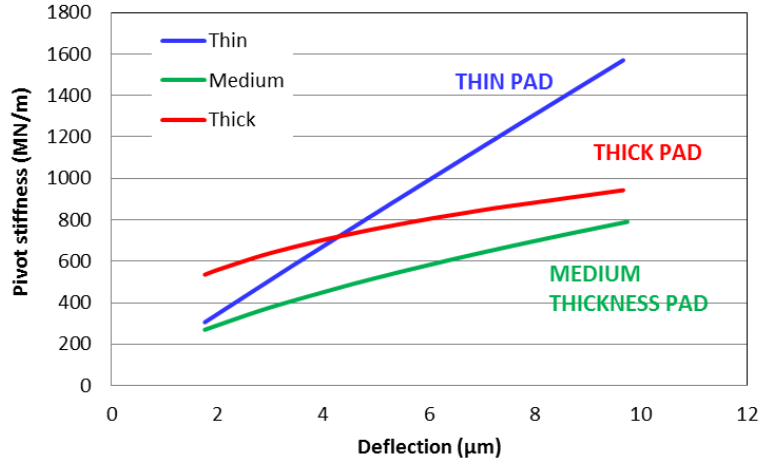


Fig. 11 Derived pivot stiffness versus average deflection for pads with thickness: thin ($t=8.5\text{mm}$), medium ($t=10\text{mm}$), and thick ($t=11.5\text{mm}$).

Table 5 lists an average *pivot stiffness* derived from the data in Figure 11. The data for displacements from $2\ \mu\text{m}$ to $10\ \mu\text{m}$ are used to obtain the average stiffness. The thin pad ($t=8.5\text{mm}$) has the largest average pivot stiffness. This is unusual, though congruent with the test data displayed in Fig. 10 [24].

Table 5 Average pivot stiffness among the pivot deflection range ($2\ \mu\text{m} \sim 10\ \mu\text{m}$)

	Pivot stiffness [MN/m]	Average pivot stiffness [MN/m]
	Gaines reported [24]	From curve fits –Fig. 11
Thin pad ($t=8.5\ \text{mm}$)	505	934
Medium thickness pad ($t=10\ \text{mm}$)	664	675
Thick ($t=11.5\ \text{mm}$)	751	775

Presently, a *pivot stiffness* for the thin pad ($t=8.5\ \text{mm}$) is estimated as follows. The ratio of pad thicknesses equals

$$\frac{t_{\text{medium}}}{t_{\text{thin}}} = \frac{10}{8.5} = 1.176, \quad \frac{t_{\text{thick}}}{t_{\text{medium}}} = \frac{11.5}{10} = 1.15 \quad (23)$$

For the thick pad, take $K_{piv(thick)} = 775$ MN/m; and assuming a pivot stiffness that is proportional to the pad thickness; then,

$$K_{piv(medium)} = \frac{K_{piv(thick)}}{1.150} = 674 \text{ MN/m}, \quad K_{piv(thin)} = \frac{K_{piv(medium)}}{1.176} = 573 \text{ MN/m} \quad (24)$$

Table 6 lists the derived pivot stiffness for each pad used in the following predictions.

Table 6 Derived pivot stiffness for each pad configuration reported by Gaines [24]. Copied from [31].

	Pivot stiffness [MN/m]
Thin pad ($t=8.5$ mm)	573
Medium thickness pad ($t=10$ mm)	675
Thick ($t=11.5$ mm)	775

Table 7 lists the maximum deformation occurring at a pad edge obtained by ANSYS® and Solidworks®. The load applied on the pad model is a uniform pressure of 689.4 kPa (100 psi). The deformations predicted by ANSYS® and Solidworks® correlate well with each other. As listed in Table 3, the elastic modulus of Babbitt is ¼ that of steel. For two pad models having the same pad thickness, the one composed of both Babbitt and steel is softer than the one solely made of steel. Hence, the FE structural model used to estimate pad elastic deformations includes the Babbitt layer.

Table 7 Maximum deformation of pad edge (inner surface) due to uniform contact pressure (0.7 MPa). Predictions using commercial FE software (ANSYS® and Solidworks®).

Thin pad: 8.5 mm	
Metal + Babbitt (ANSYS®), $t=7$	13.4 μm
All metal (ANSYS®), $t=8.5$ mm	9.6 μm
All metal (Solidworks®), $t=8.5$ mm	10.3 μm
Medium thickness pad: 10 mm	
Metal + Babbitt(ANSYS®), $t=8.5$	8.4 μm
All metal (ANSYS®), $t=10$ mm	6.3 μm
All metal (Solidworks®), $t=10$ mm	7.1 μm
Thick pad: 11.5 mm	
Metal + Babbitt (ANSYS®), $t=10$	6.1 μm
All metal (ANSYS®), $t=11.5$ mm	4.8 μm
All metal (Solidworks®), $t=11.5$ mm	4.4 μm

This section shows predictions for the three sets TPJBs, each set with a different pad thickness ($t=8.5$ mm, 10 mm and 11.5 mm). As in the tests, the predictions are obtained for rotor speeds equal to 6 krpm and 12 krpm, and for unit loads ($W/(LD)$) from 172 kPa to 1,724 kPa. Predictions follow with and without the consideration of pad flexibility. Note that all the predictions include the pivot stiffnesses listed in Table 6.

The current predictive model includes both the shaft and pad thermal expansion due to a rise in film temperature. The shaft and pads, both made of steel, have a thermal expansion coefficient of 1.2×10^{-5} 1/ °C [34]. The predictive model assumes that the lubricant carries away all the heat generated in the bearing, i.e., an adiabatic heat flow condition. According to Tao [23], the inlet thermal mixing coefficient (λ) varies for differing rotor speed; a larger λ should be used for a high rotor speed ($\Omega > 10$ krpm). Thus, at $\Omega=6$ krpm, $\lambda=0.8$; while at $\Omega=12$ krpm, $\lambda=0.98$.

Figure 12(a) shows a comparison between the predicted and measured journal eccentricity ratio (e_y/C_p) along the load direction (Y) for operation at 6 krpm and 12

krpm. The predictions include curves accounting for pad flexibility and without it. At both operational speeds ($\Omega=6$ krpm, 12 krpm), the predictions with pad flexibility correlate better with the test data as the applied load increases. Predictions solely considering pivot flexibility deliver a larger static eccentricity (e_Y). Pad flexibility tends to reduce the predicted journal eccentricity, in particular for operation at the high rotor speed ($\Omega=12$ krpm). Figure 12(b) depicts the predicted maximum pad deformation (u_{max}/C_p) increasing linearly with the unit load ($W/(LD)$). u_{max}/C_p is slightly larger at a larger journal speed ($\Omega=12$ krpm). At $\Omega=12$ krpm and $W/(LD)=1,724$ kPa, the maximum deformation for the thin pad is 25% of the pad clearance. Note that at $W/(LD)=0$ kPa, $u_{max}>0$ since the bearing pads, each having a preload $\bar{r}_p=0.25$, generate a significant pressure field that deforms the pad surface.

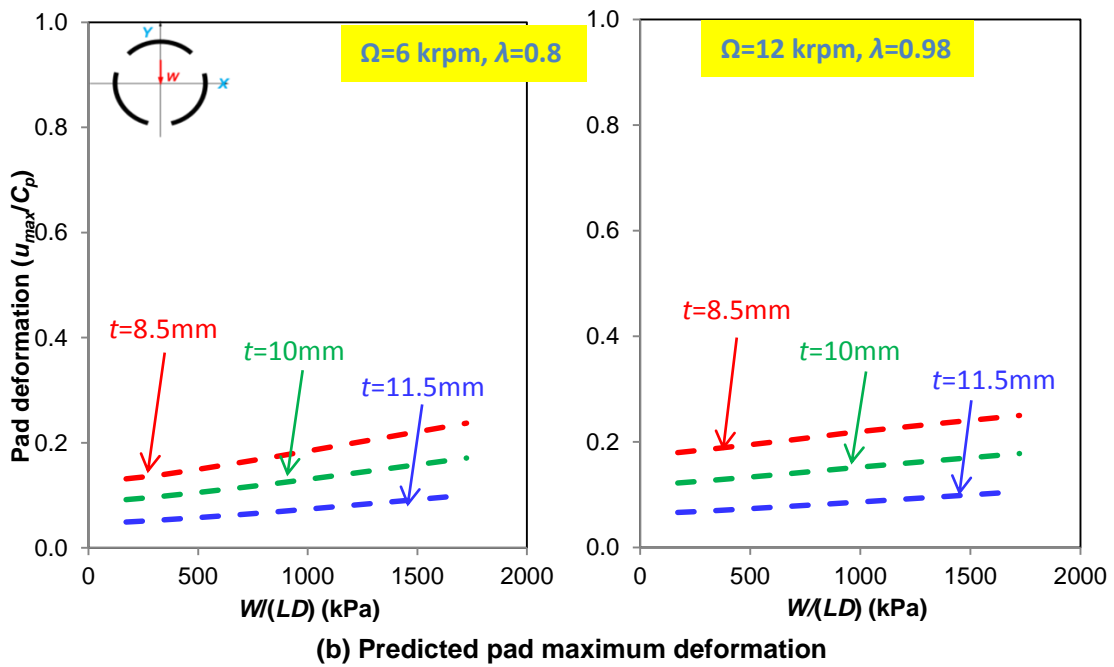
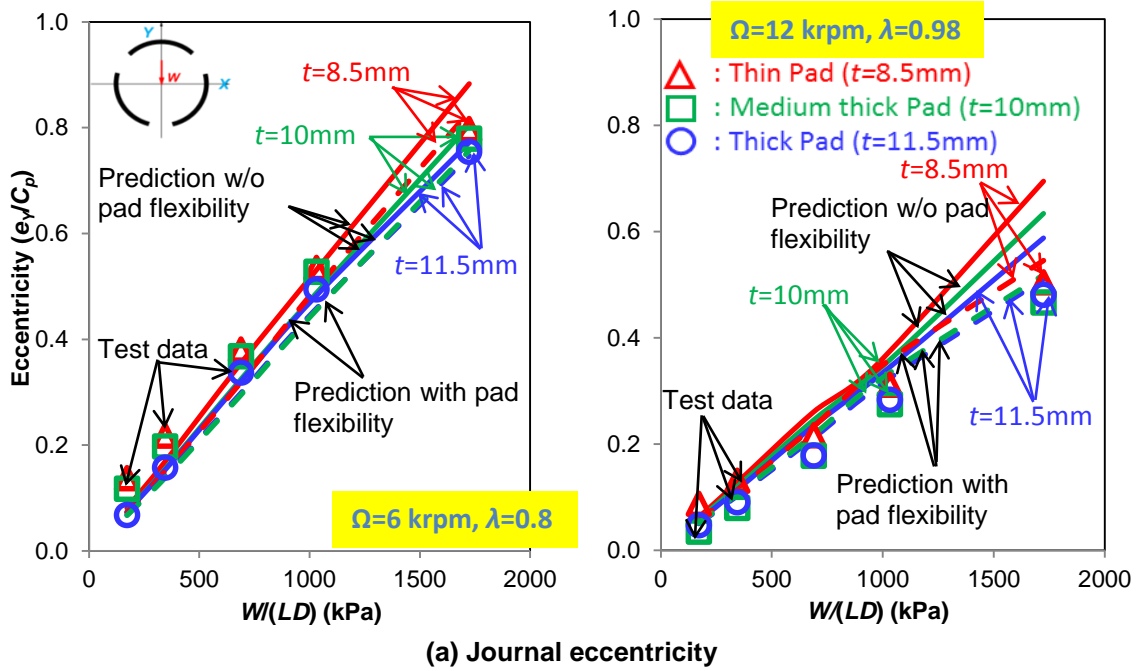
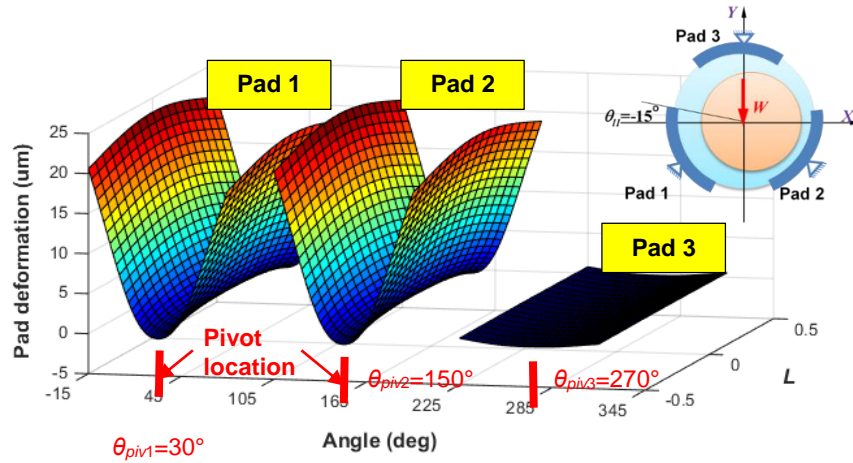


Fig. 12 (a) Journal eccentricity (e_y/C_p) along the load direction and (b) predicted pad maximum deformation (u_{max}/C_p) versus unit load $W(LD)$. Journal speed $\Omega=6$ krpm and 12 krpm. Predictions (with and without pad flexibility) and test data from Gaines [24]. Results shown for thin, medium and thick pads.

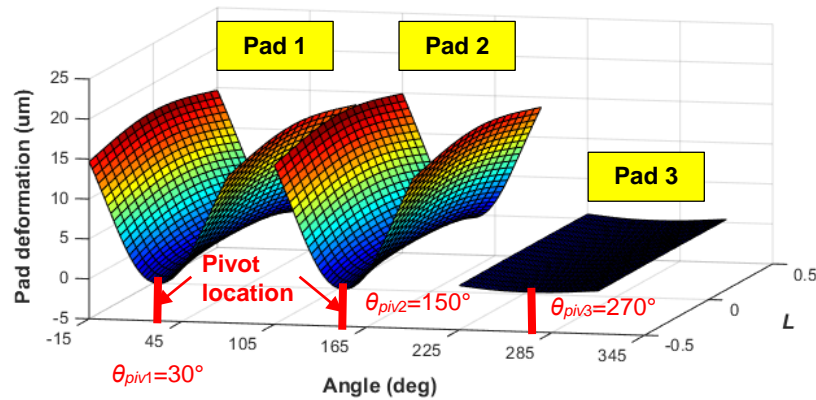
Figure 13 shows the predicted pad surface deformation due to the action of the hydrodynamic fluid film pressure. The maximum pad surface deformation⁷ locates at both the trailing edge and the leading edge of a pad. Note that at $W/(LD)=1,724$ kPa and with shaft speed $\Omega=12$ krpm, the upper pad (#3) has no deformation as it is unloaded. The deformation along the axial direction is not uniform. For example, along the pad leading edge, the deformation at the pad mid-plane ($Z=0$) is up to 12% larger than that at the pad side edges ($Z=\pm 1/2 L$).

Figure 14 depicts the predicted and measured maximum temperature rise ($\Delta T_{\max}/T_{in}$) versus unit load for operation at two journal speeds. In the tests [24], a pad sub-surface (~5 mm below) temperature is recorded at 75% of the pad arc length. Predictions account for the heat transfer conducted through a pad and the heat convection in the back of a pad. The predictions show the bulk fluid film temperature in pad 2. Generally, the maximum temperatures are underestimated, in particular at the high speed and largest load; $\Omega=12$ krpm, $W/(LD)=1,724$ kPa.

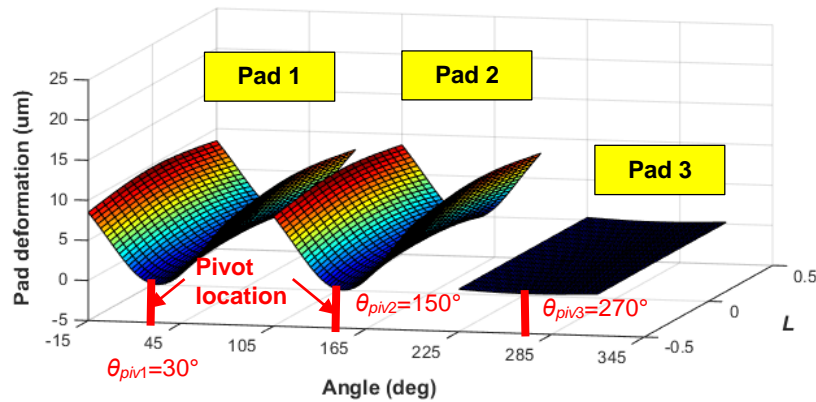
⁷ Relative to the pivot radial displacement.



(a) Thin pad, $t=8.5$ mm



(b) Medium thick pad, $t=10$ mm



(c) Thick pad, $t=11.5$ mm

Fig. 13 Pad surface deformation. $W(LD)=1,724$ kPa, $\Omega= 12$ krpm. Hot pad clearance for the TPJB with thin pad sets, medium thick pad sets, and thick pad sets: $C_p= 83.5 \mu\text{m}$, $82.9 \mu\text{m}$ and $81.4 \mu\text{m}$. Results shown for thin, medium and thick pads.

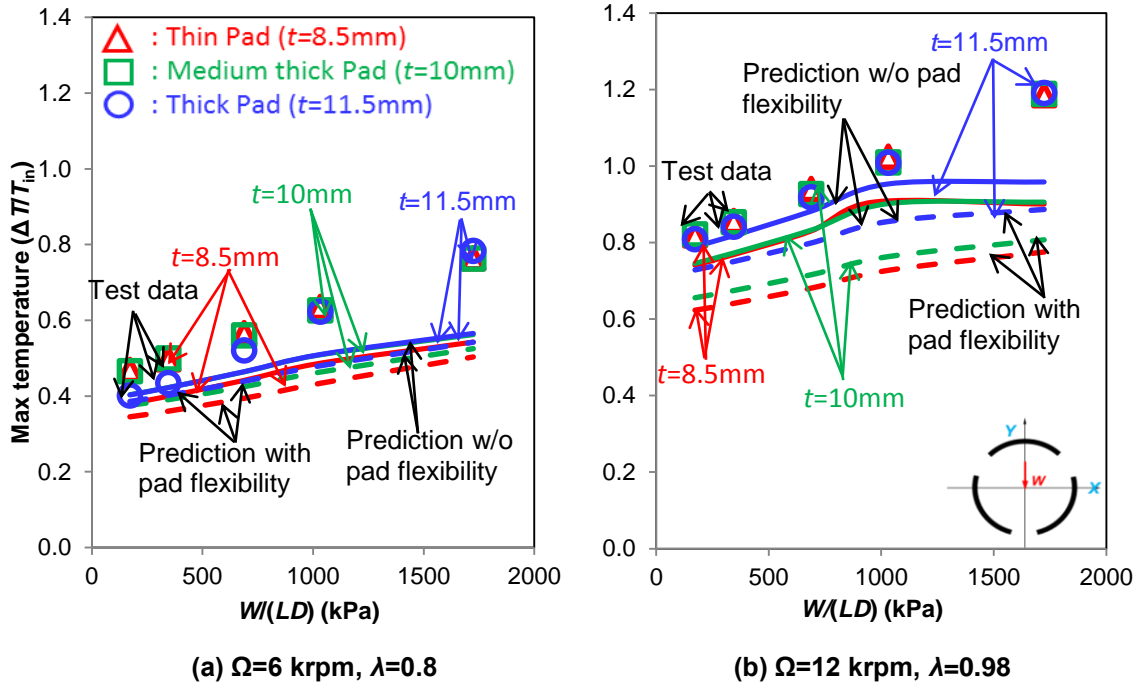


Fig. 14 Predicted and measured maximum temperature versus unit load. $\Omega=6$ krpm and 12 krpm; $W(LD)=172$ kPa to 1,724 kPa. Predictions from current model. Test data from Gaines [24]. Copied from [31].

Note that the maximum temperatures are underestimated, in particular at the high speed and large load ($\Omega=12$ krpm, $W(LD) = 1,724$ kPa). Table 8 lists the measured and predicted flow rate and the oil temperature change, i.e. $(T_{out}-T_{in})^8$ and $(T_{max} - T_{in})^9$. The significant differences in temperatures are due to the test bearing being supplied with a fixed flow rate, irrespective of the load and journal speed condition. The current model cannot account for this circumstance. For tests with a shaft speed of 6 krpm, the actual supplied flow rate (31 LPM) is greater than the one predicted (17 LPM) while the recorded peak pad surface temperatures are much higher.

⁸ T_{out} is the outlet oil temperature and $T_{in}=49^\circ\text{C}$ is the supply oil temperature. $(T_{out}-T_{in}) \sim P_w/(\rho \cdot C_v \cdot Q)$, where P_w is the power loss, Q is the flow rate, C_v is the specific heat, and ρ is the lubricant density.

⁹ T_{max} is the maximum pad subsurface temperature measured at 75% of the pad arc length.

Table 8 Measured and predicted flow rate, measured outlet and peak temperature for the TPJBs with thin and thick pads ($t=8.5$ mm, 11.5 mm) operating at 6 krpm and 12 krpm.

Pad type	Speed (rpm)	Unit Load (kPa)	Flow rate (LPM)		$T_{out}-T_{in}$ (°C)		Measured $T_{max}-T_{in}$ (°C)
			Predicted	Measured	Predicted	Measured	
Thin pad ($t=8.5$ mm)	6,000	172	17.7	31.2	20.0	3.6	22.9
		345	17.7	31.3	20.1	3.6	24.2
		689	17.7	31.2	20.6	3.8	27.6
		1034	17.8	31.2	21.7	4.1	31.0
		1724	17.6	31.1	26.3	4.2	37.3
	12,000	172	35.6	31.5	26.9	12.2	40.0
		345	35.6	31.6	27.0	12.2	41.8
		689	35.6	31.3	27.5	12.6	45.9
		1034	35.4	31.2	28.4	12.6	50.0
		1724	33.6	31.2	31.4	12.9	57.9
Thick pad ($t=11.5$ mm)	6,000	172	15.8	31.7	25.4	3.5	19.5
		345	15.8	31.6	25.5	3.4	21.2
		689	15.8	31.4	26.4	3.5	25.4
		1034	15.8	31.5	28.2	3.9	30.4
		1724	15.7	31.2	33.8	3.8	38.2
	12,000	172	30.0	31.4	34.8	11.6	39.5
		345	30.0	31.3	35.0	11.5	41.1
		689	30.0	31.4	35.7	11.9	44.8
		1034	29.8	31.3	37.5	11.7	49.3
		1724	29.1	31.4	40.1	11.2	58.1

To support the assertion, note that the recorded lubricant outlet temperature is much lower than the measured peak temperatures, a few degrees above the supply oil temperature [24] (Table 8), and also lower than the predicted lubricant temperature at the bearing exit plane. Hence, excessive churning of the lubricant on the bearing sides contributes to the distinctive differences. At the high shaft speed condition ($\Omega=12$ krpm),

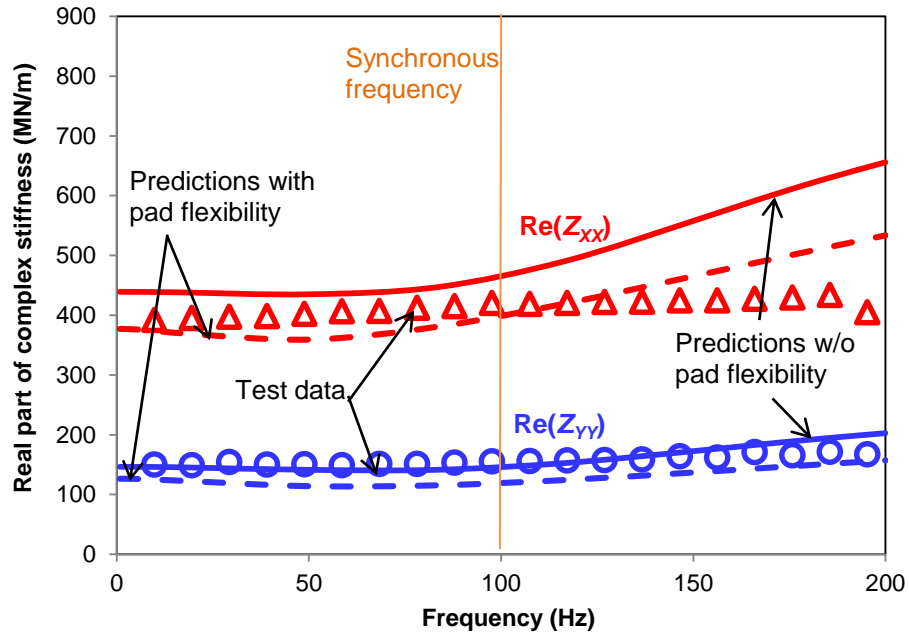
most of the cold supply flow rate likely does not enter the bearing pads, thus causing the lubricant (and pads) to heat excessively.

In Ref. [24], Gaines uses a frequency independent (K - C - M) model to extract the bearing static stiffness (K), damping (C) and virtual mass (M) coefficients from curve fits to the experimentally derived complex stiffnesses (Z),

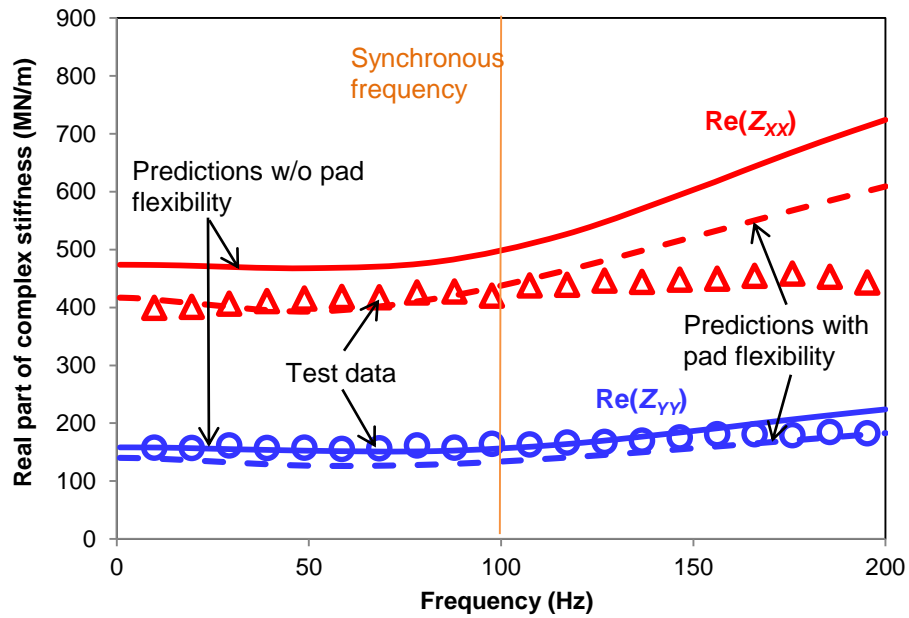
$$\text{Re}(Z) \rightarrow K - \omega^2 M, \text{Im}(Z) \rightarrow \omega C \quad (25)$$

In Ref. [24], the frequency range to obtain the bearing K - C - M coefficients is 0~200 Hz. The predictions are based on the same frequency range. The following figures compare test data against predictions with/without the consideration of pad flexibility. To evaluate the effect of pad flexibility, Figures 15-18 depict predictions accounting for both pad and pivot flexibility and predictions considering pivot flexibility only.

For the largest applied static load, Figures 15 and 16 show the real part of the bearing direct complex stiffnesses, $\text{Re}(Z)$, obtained at two shaft speeds ($\Omega=6$ krpm and 12 krpm) versus excitation frequency ($0 < \omega < 200$ Hz). Note $\text{Re}(Z_{YY})$, along the load direction, is less than $\text{Re}(Z_{XX})$. This peculiar behavior is distinctive for the three-pad bearing, each pad having a large (90°) arc extent. In general, the predicted $\text{Re}(Z_{YY})$ correlates best with the test data, whereas $\text{Re}(Z_{XX})$ is overestimated at high frequencies ($\omega > 100$ Hz). Note the experimental $\text{Re}(Z)$ show little frequency dependency, yet the predictions forward a stiffening $\text{Re}(Z_{YY})$ as frequency increases, and in particular for operation at the low shaft speed (6 krpm). Including pad flexibility reduces the dynamic stiffness, $\text{Re}(Z)$; the effect being more pronounced on the thin pad.

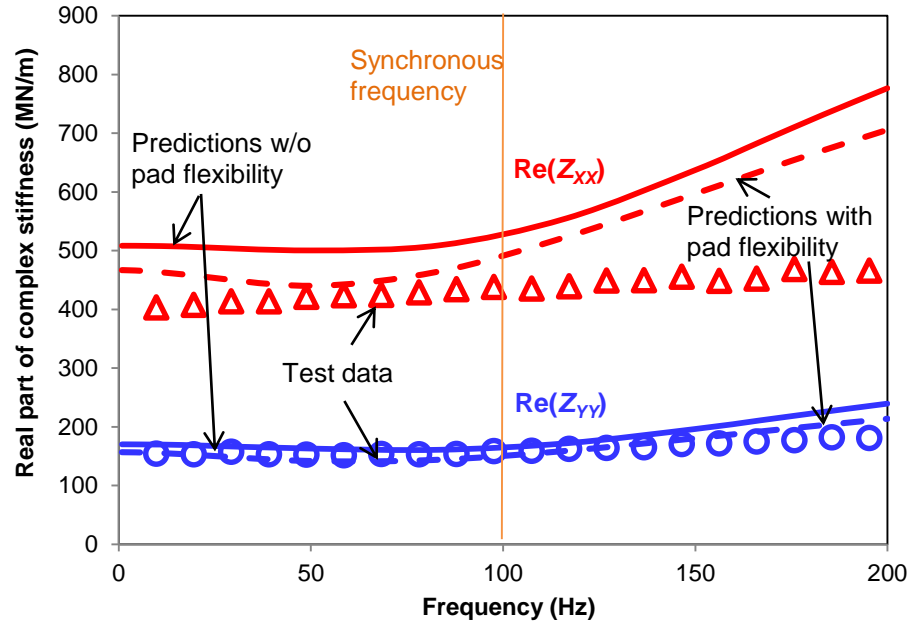


(a) Thin pad, $t=8.5$ mm



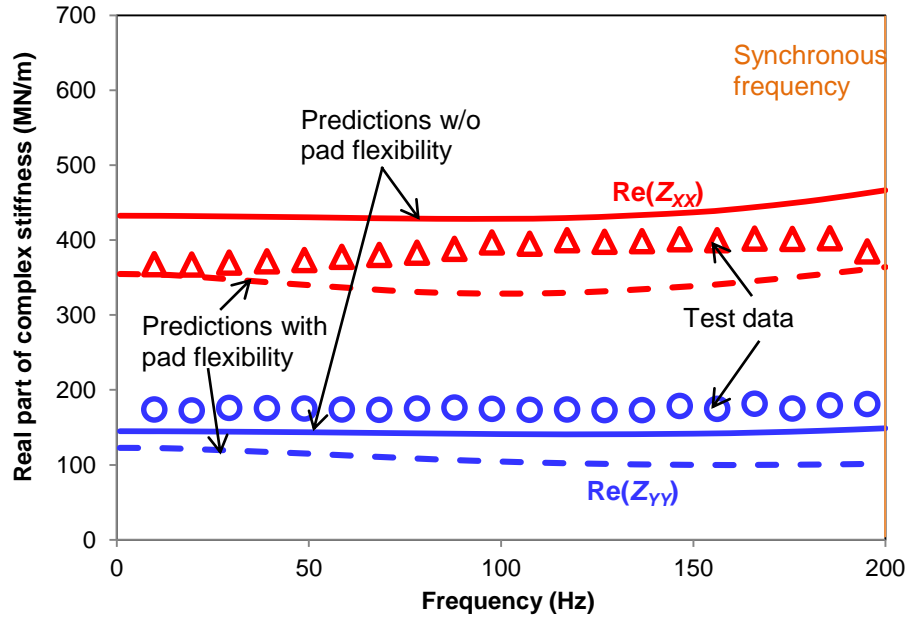
(b) Medium thickness pad, $t=10$ mm

Fig. 15 Real part of bearing complex stiffnesses, $Re(Z)$, for TPJBs with pads of thickness (a) $t=8.5$ mm (b) $t=10$ mm (c) $t=11.5$ mm. Shaft speed $\Omega=6$ krpm and unit load $W/(LD)=1,724$ kPa. Test data from Gaines [24] and predictions (with and without pad flexibility). Copied from [31].

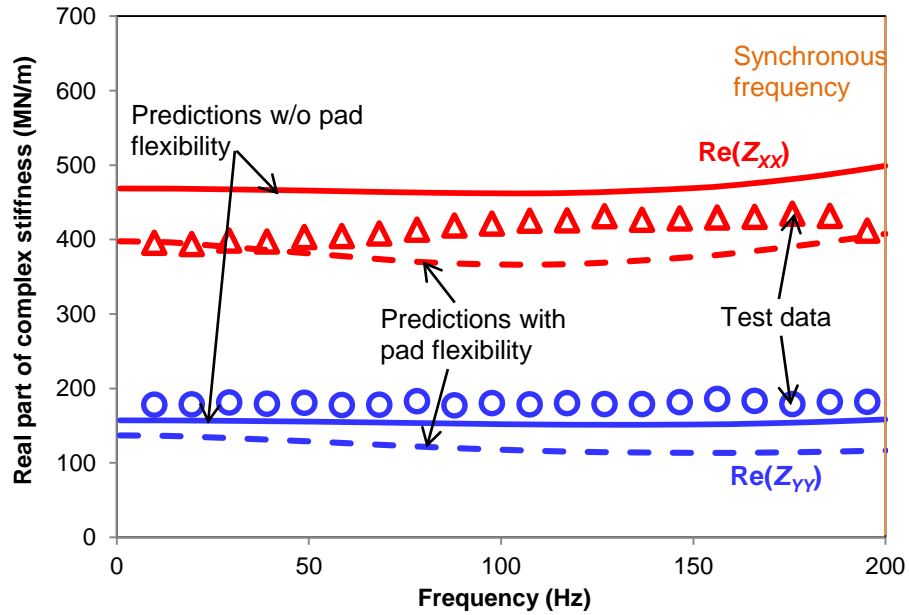


(c) Thick pad, $t=11.5$ mm

Fig. 15 Continued.

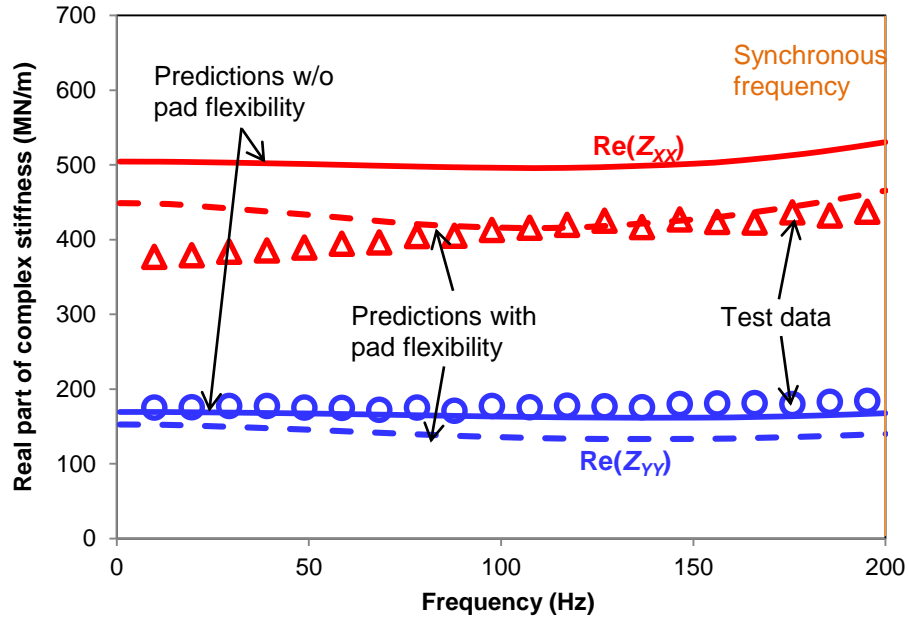


(a) Thin pad, $t=8.5$ mm



(b) Medium thickness pad, $t=10$ mm

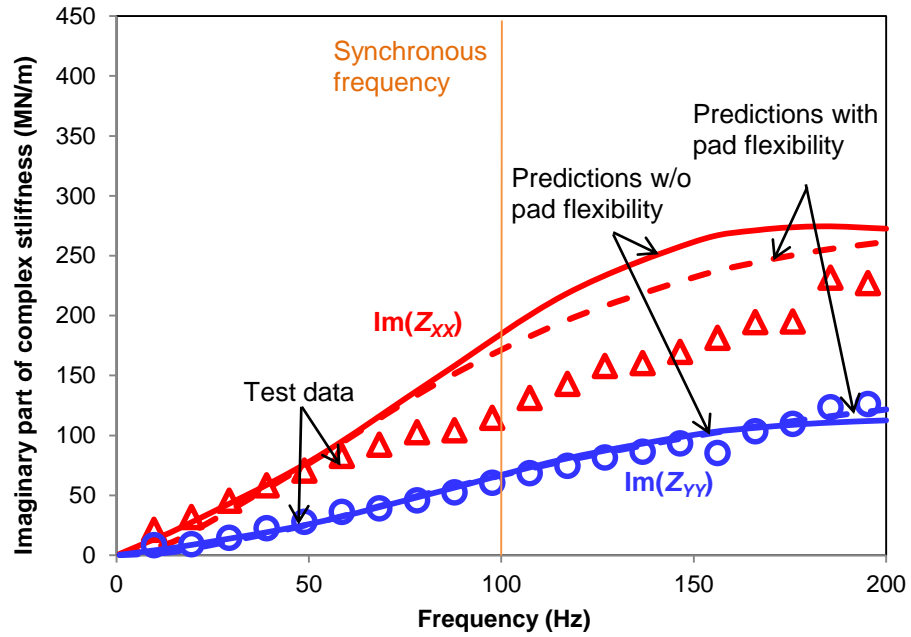
Fig. 16 Real part of bearing complex stiffnesses, $Re(Z)$, for TPJBs with pads of thickness (a) $t=8.5$ mm (b) $t=10$ mm (c) $t=11.5$ mm. Shaft speed $\Omega=12$ krpm and unit load $W(LD)=1,724$ kPa. Test data from Gaines [24] and predictions (with and without pad flexibility). Copied from [31].



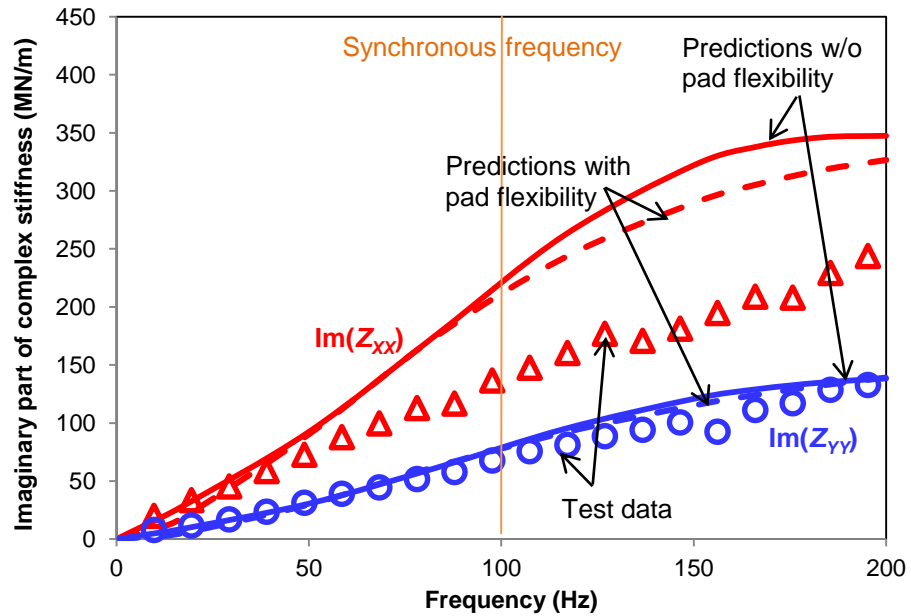
(c) Thick pad, $t=11.5$ mm

Fig. 16 Continued.

For the same static load condition and two journal speeds, Figures 17 and 18 depict the experimental and predicted imaginary part of the bearing complex stiffnesses, $\text{Im}(Z)$. In general, the bearing damping coefficient (C) is the slope of $\text{Im}(Z) \sim \omega C$. Both $\text{Im}(Z_{XX})$ and $\text{Im}(Z_{YY})$ from the experiments show a linear growth with frequency, i.e., a frequency independent C . Note $\text{Im}(Z_{XX}) > \text{Im}(Z_{YY})$. The predictions are in very good agreement with the experimental results for operation with the high shaft speed (12 krpm). On the other hand, for operation at 6 krpm, the predicted $\text{Im}(Z_{XX})$ is larger than the test results and evidences a reduction in growth on the high side of the excitation frequency range ($\omega > 1.5\Omega$).

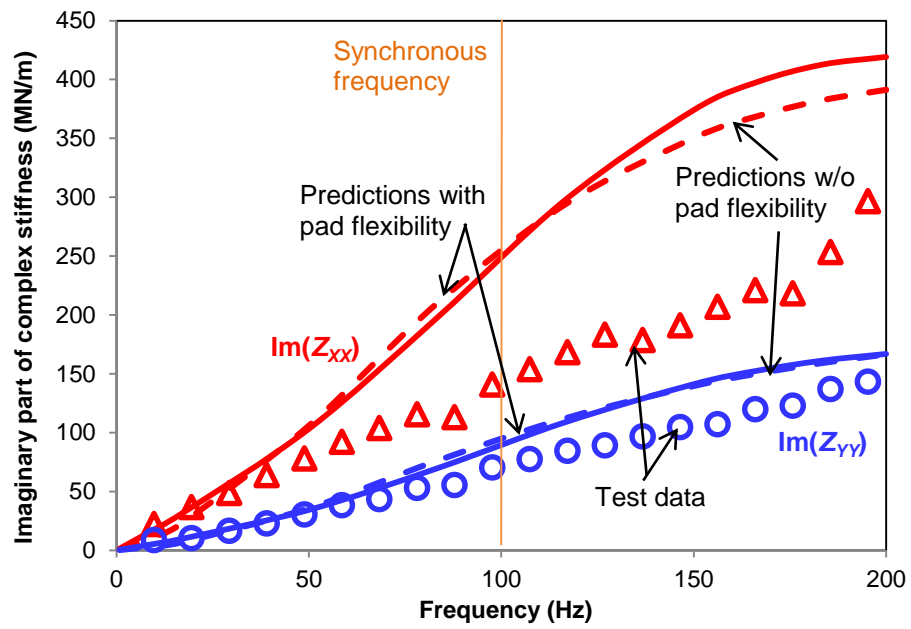


(a) Thin pad, $t=8.5$ mm



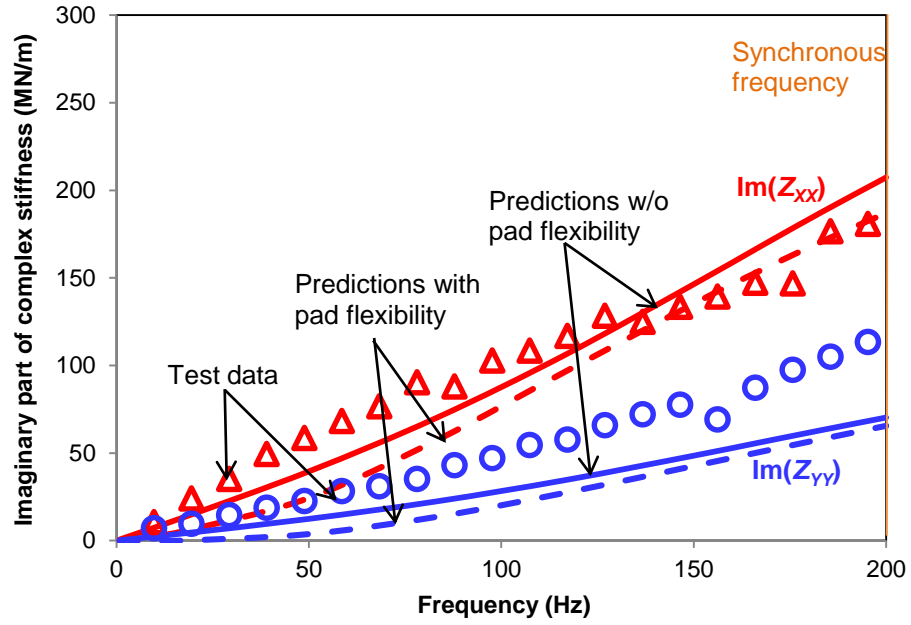
(b) Medium thickness pad, $t=10$ mm

Fig. 17 Imaginary part of bearing complex stiffnesses, $\text{Im}(Z)$, for TPJBs with pads of thickness (a) $t=8.5$ mm (b) $t=10$ mm (c) $t=11.5$ mm. Shaft speed $\Omega=6$ krpm and unit load $W(LD)=1,724$ kPa. Test data from Gaines [24] and predictions (with and without pad flexibility). Copied from [31].

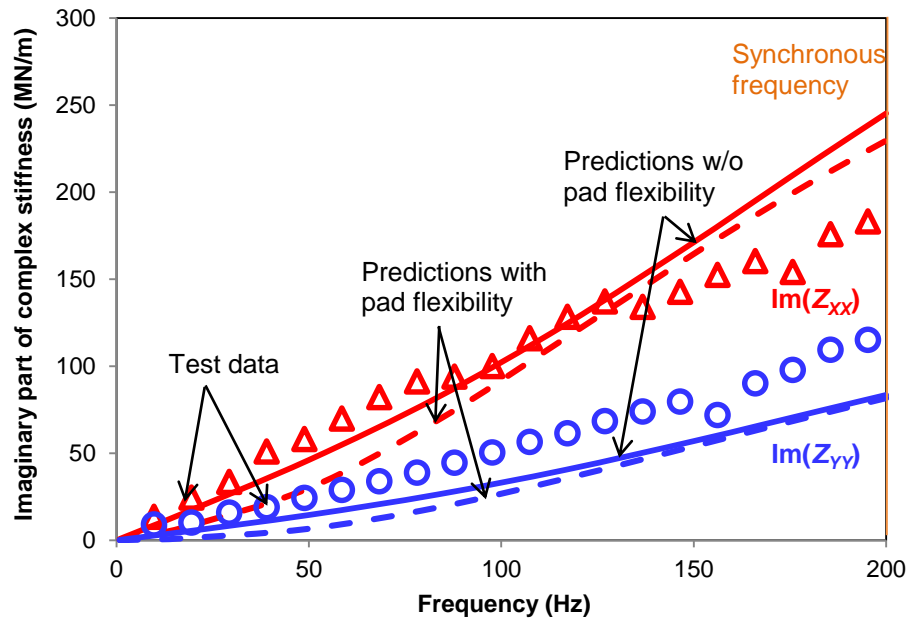


(c) Thick pad, $t=11.5$ mm

Fig. 17 Continued.

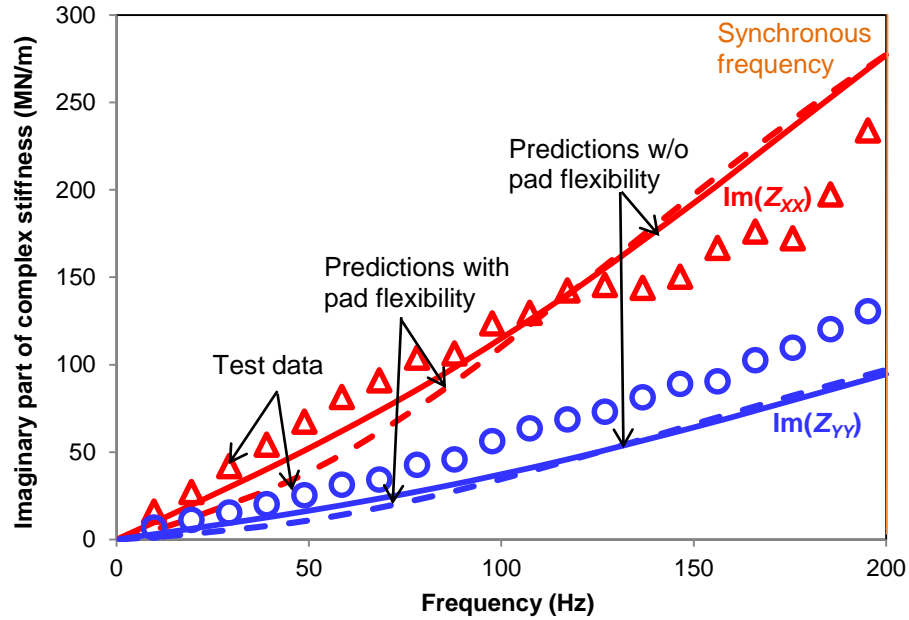


(a) Thin pad, $t=8.5$ mm



(b) Medium thickness pad, $t=10$ mm

Fig. 18 Imaginary part of bearing complex stiffnesses, $\text{Im}(Z)$, for TPJBs with pads of thickness (a) $t=8.5$ mm (b) $t=10$ mm (c) $t=11.5$ mm. Shaft speed $\Omega=12$ krpm and unit load $W/(LD)=1,724$ kPa. Test data from Gaines [24] and predictions (with and without pad flexibility). Copied from [31].



(c) Thick pad, $t=11.5$ mm

Fig. 18 Continued.

The correlation coefficient (r^2) represents the goodness of the $[K-C-M]$ curve fit to predicted complex stiffnesses. Table 9 lists r^2 for the results of predictions conducted with three TPJB configurations. A correlation coefficient (r^2) $\rightarrow 1$ indicates that the $[K-C-M]$ model delivers perfect force coefficients. All the correlation coefficients for the curve fits to the predicted imaginary part of the bearing complex stiffnesses are close to 1, thus revealing that the predicted damping coefficients are nearly frequency independent.

At a rotor speed of 12 krpm, the correlation coefficients of the curve fit (K, M) parameters to the predicted real part of the bearing complex stiffnesses are low, varying from 0.13 to 0.87. Recall that at a rotor speed of 12 krpm, $\text{Re}(Z)$ is almost invariant over the frequency range (0~200Hz). At $\Omega=6$ krpm, $\text{Re}(Z)$ is frequency independent at a sub synchronous frequency ($\omega < \Omega$). Thus, $\text{Re}(Z)$ is not a quadratic function of ω and the curve ($K-M\omega^2$) cannot adequately represent $\text{Re}(Z)$. A constant K is a better match.

Table 9 Correlation coefficients (r^2) of curve fit force coefficients (K, C, M) to predicted complex stiffnesses at two operating conditions for TPJBs in Ref. [24]. Excitation frequency range 0 to 200 Hz.

	Rotor speed		Specific load (kPa)				
			172	345	689	1,032	1,724
Thin pad $t=8.5$ mm	6 krpm	$K_{XX}-\omega^2 M_{XX} \rightarrow \text{Re}(Z_{XX})$	0.86	0.80	0.94	0.96	0.99
		$K_{YY}-\omega^2 M_{YY} \rightarrow \text{Re}(Z_{YY})$	0.80	0.77	0.76	0.79	0.90
		$\omega C_{XX} \rightarrow \text{Im}(Z_{XX})$	1.00	1.00	1.00	1.00	0.99
		$\omega C_{YY} \rightarrow \text{Im}(Z_{YY})$	1.00	1.00	1.00	1.00	0.99
	12 krpm	$K_{XX}-\omega^2 M_{XX} \rightarrow \text{Re}(Z_{XX})$	0.71	0.66	0.51	0.29	0.19
		$K_{YY}-\omega^2 M_{YY} \rightarrow \text{Re}(Z_{YY})$	0.78	0.79	0.82	0.84	0.87
		$\omega C_{XX} \rightarrow \text{Im}(Z_{XX})$	0.99	0.99	0.99	0.99	0.99
		$\omega C_{YY} \rightarrow \text{Im}(Z_{YY})$	0.99	0.99	0.98	0.98	0.98
Medium thick pad $t=10$ mm	6 krpm	$K_{XX}-\omega^2 M_{XX} \rightarrow \text{Re}(Z_{XX})$	0.86	0.89	0.93	0.96	0.99
		$K_{YY}-\omega^2 M_{YY} \rightarrow \text{Re}(Z_{YY})$	0.80	0.78	0.75	0.76	0.93
		$\omega C_{XX} \rightarrow \text{Im}(Z_{XX})$	1.00	1.00	1.00	1.00	0.99
		$\omega C_{YY} \rightarrow \text{Im}(Z_{YY})$	1.00	1.00	1.00	1.00	1.00
	12 krpm	$K_{XX}-\omega^2 M_{XX} \rightarrow \text{Re}(Z_{XX})$	0.76	0.71	0.58	0.37	0.13
		$K_{YY}-\omega^2 M_{YY} \rightarrow \text{Re}(Z_{YY})$	0.80	0.82	0.83	0.84	0.84
		$\omega C_{XX} \rightarrow \text{Im}(Z_{XX})$	0.99	0.99	0.99	0.99	0.99
		$\omega C_{YY} \rightarrow \text{Im}(Z_{YY})$	0.99	0.99	0.99	0.98	0.98
Thick pad $t=11.5$ mm	6 krpm	$K_{XX}-\omega^2 M_{XX} \rightarrow \text{Re}(Z_{XX})$	0.84	0.88	0.93	0.96	0.99
		$K_{YY}-\omega^2 M_{YY} \rightarrow \text{Re}(Z_{YY})$	0.78	0.74	0.74	0.80	0.94
		$\omega C_{XX} \rightarrow \text{Im}(Z_{XX})$	1.00	1.00	1.00	1.00	0.99
		$\omega C_{YY} \rightarrow \text{Im}(Z_{YY})$	1.00	1.00	1.00	1.00	1.00
	12 krpm	$K_{XX}-\omega^2 M_{XX} \rightarrow \text{Re}(Z_{XX})$	0.78	0.74	0.61	0.38	0.22
		$K_{YY}-\omega^2 M_{YY} \rightarrow \text{Re}(Z_{YY})$	0.81	0.83	0.86	0.83	0.73
		$\omega C_{XX} \rightarrow \text{Im}(Z_{XX})$	0.99	0.99	0.99	0.99	0.99
		$\omega C_{YY} \rightarrow \text{Im}(Z_{YY})$	0.99	0.99	0.98	0.98	0.99

Define dimensionless dynamic force coefficients as¹⁰

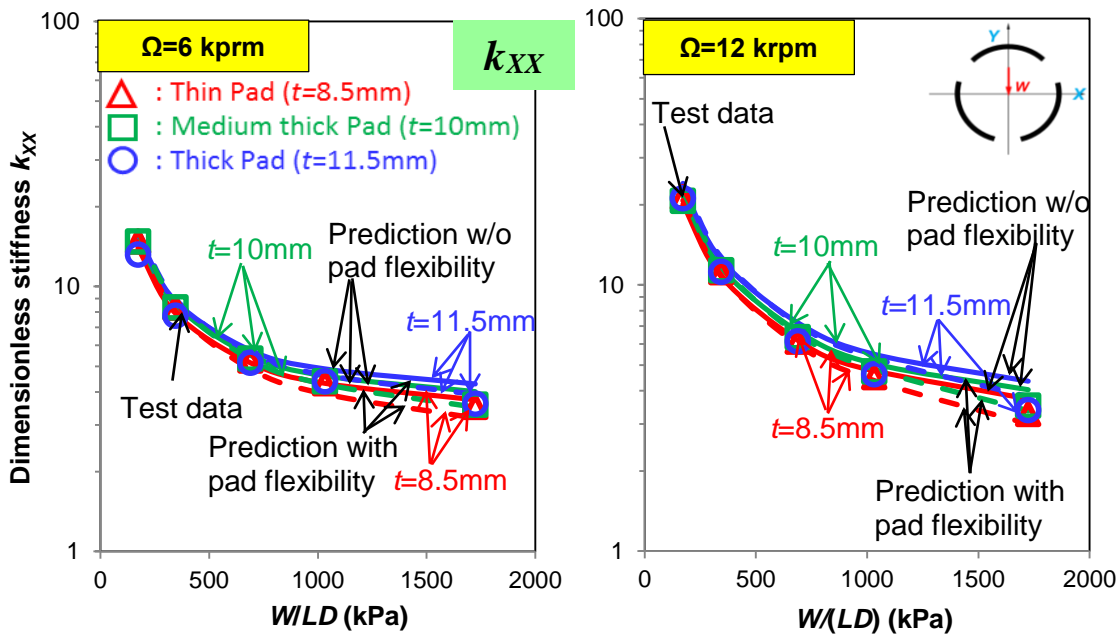
$$k_{ij} = \frac{K_{ij} C_p}{W}, c_{ij} = \frac{C_{ij} \Omega C_p}{W}, m_{ij} = \frac{M_{ij} \Omega^2 C_p}{W} \quad i, j = X, Y \quad (26)$$

where K , C and M are the bearing stiffness, damping and virtual mass coefficients derived from the complex stiffnesses using a $[K-C-M]$ model. C_p is the cold pad radial clearance, Ω is the rotor speed in rad/s, and W is the static load applied on the bearing.

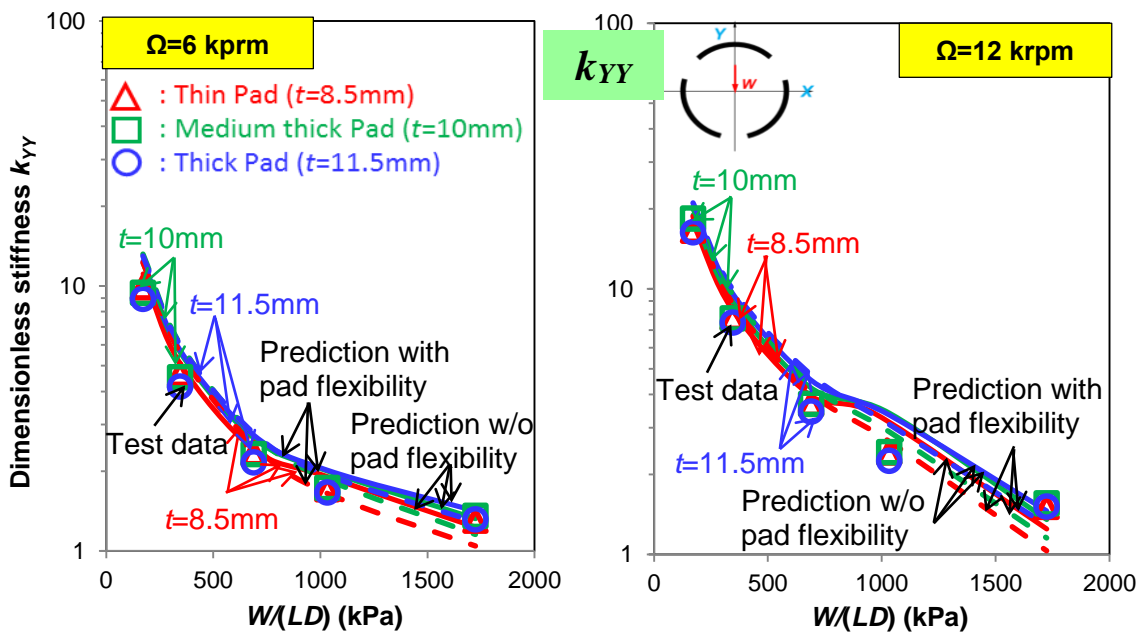
Figure 19 depicts the TPJB stiffness coefficients ($k_{XX} > k_{YY}$) versus unit load as identified (curve fits) from the measured and predicted bearing complex stiffnesses (Z). The predicted stiffnesses correlate well with the test data at low loads, $W/(LD) < 1,032$ kPa, but are underestimated at the highest load, $W/(LD) = 1,724$ kPa. Note that pad flexibility increases the predicted k_{XX} and k_{YY} at low loads, $W/(LD) < 689$ kPa, whereas it reduces the predicted k_{XX} and k_{YY} for high loads, $W/(LD) > 689$ kPa. Predicted direct stiffnesses accounting for pad flexibility are up to 20% smaller than those assuming a rigid pad. As the pad thickness decreases from 11.5 mm to 8.5 mm, the predicted k_{XX} decreases by 21%.

Interestingly, the direct stiffness (k_{YY}) along the static load direction ($-Y$) is significantly lower than the stiffness k_{XX} , in particular as the unit load increases. Fig. 20 depicts the film thickness and hydrodynamic pressure at the bearing mid-plane ($z = 1/2 L$). Both the minimum film thickness and the maximum pressure are quite close to the X axis ($\theta = 180^\circ$), thus causing a large stiffness along the unloaded direction (X). That is, the stiffening effect is a result of the long arc extent of the bearing pads, 90° .

¹⁰ At $W/(LD) = 172, 345, 689, 1,032$ and $1,724$ kPa, $W/C_p = [11, 23, 46, 69, 115]$ MN/m; at the journal speed of 6 krpm, $W/(\Omega C_p) = [18265, 36637, 73168, 109805, 183079]$ N·s/m, and $W/(\Omega^2 C_p) = [29, 58, 116, 175, 291]$ kg; at the journal speed of 12 krpm, $W/(\Omega C_p) = [9133, 18318, 36584, 54902, 91539]$ N·s/m, and $W/(\Omega^2 C_p) = [7, 15, 29, 44, 73]$ kg.



(a) k_{xx}



(b) k_{yy}

Fig. 19 Direct stiffnesses (k_{xx} and k_{yy}) versus unit load and two shaft speeds. Predictions (without and with pad flexibility) and test data from Gaines [24]. Results shown for thin, medium and thick pads. Copied from [31].

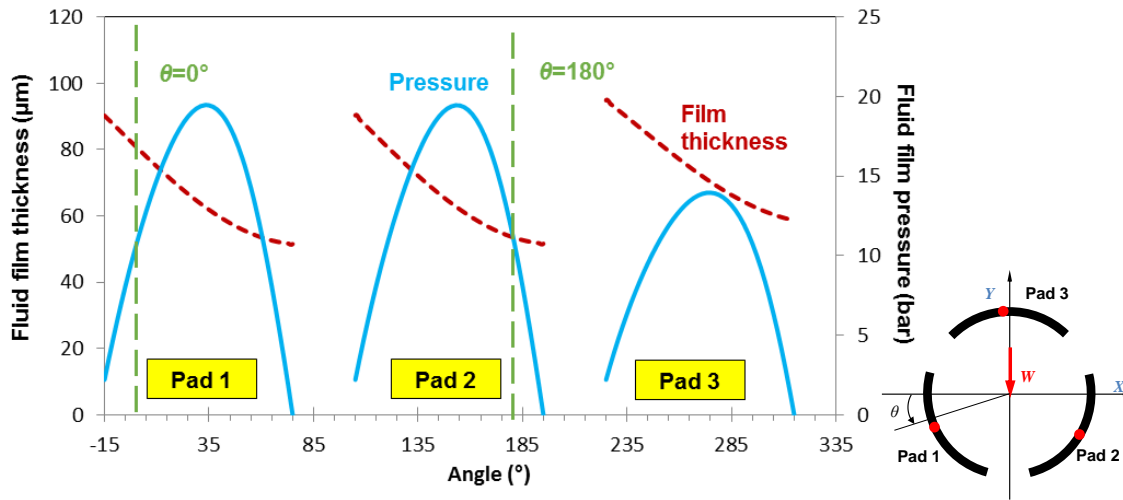
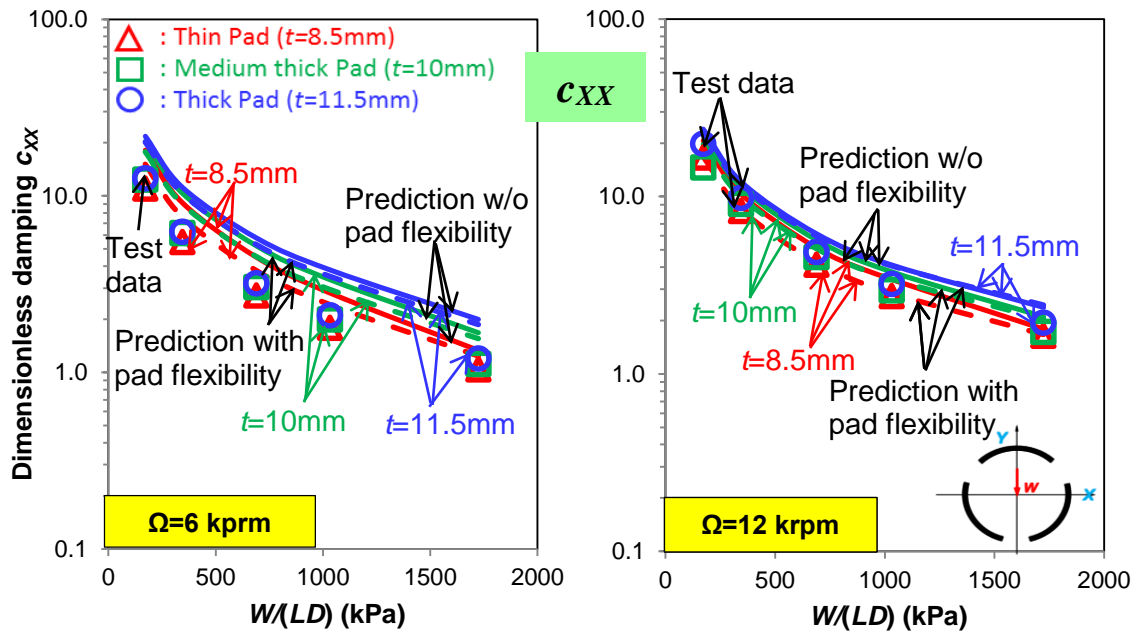
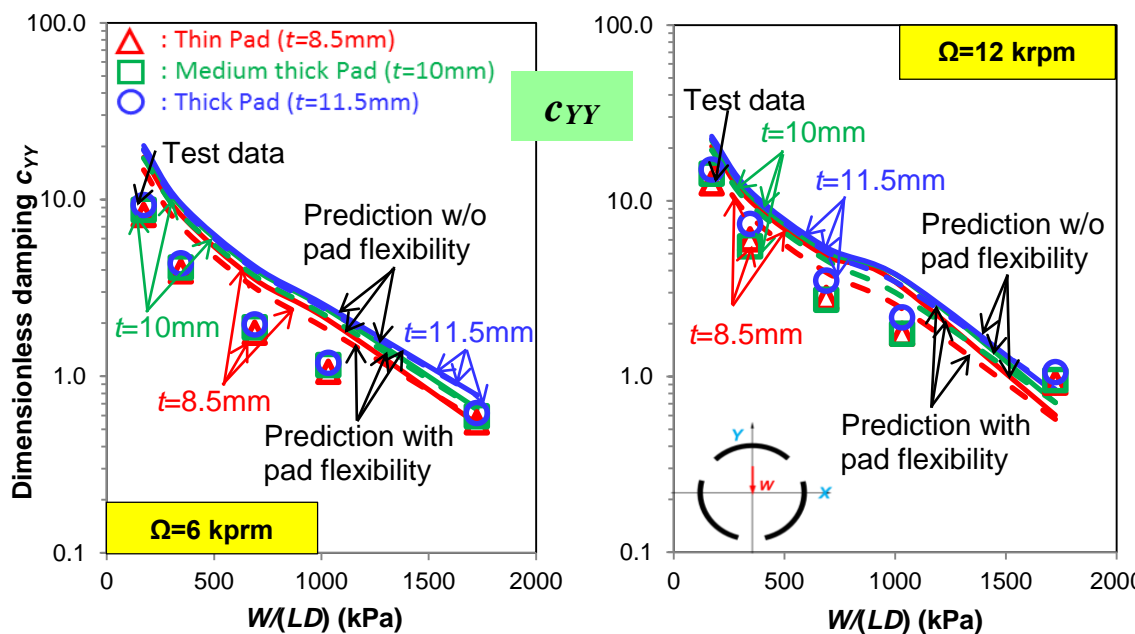


Fig. 20 Predicted film pressure and film thickness at bearing mid plane. Operation with unit load $W/(LD)=172$ kPa and shaft speed $\Omega=6$ krpm. Location of the maximum film pressure for each pad: $\theta_1=33^\circ$ (pad 1), $\theta_2=153^\circ$ (pad 2) and $\theta_3=273^\circ$ (pad 3). Location of the minimum film thickness for each pad: $\theta_1=53^\circ$ (pad 1), $\theta_2=173^\circ$ (pad 2) and $\theta_3=301^\circ$ (pad 3). Copied from [31].

Figure 21 depicts the damping coefficients ($c_{xx} > c_{yy}$) versus unit load for two shaft speeds. Pad flexibility reduces the predicted damping over the entire load range, $172 \text{ kPa} < W/(LD) < 1,724 \text{ kPa}$. The experimental results show less differences for the three pad thicknesses than the model otherwise predicts. Predictions including pad flexibility deliver damping coefficients that are up to 20% lower than similar coefficients obtained with a rigid pads model. Reducing the pad thickness from 11.5 mm to 8.5 mm produces also a reduction of 34% (at most) in predicted direct damping. Note that the test results appear to agree with the predictions including pad flexibility for c_{xx} . At the rotor speed of 6 krpm, including pad flexibility still overestimates c_{yy} .



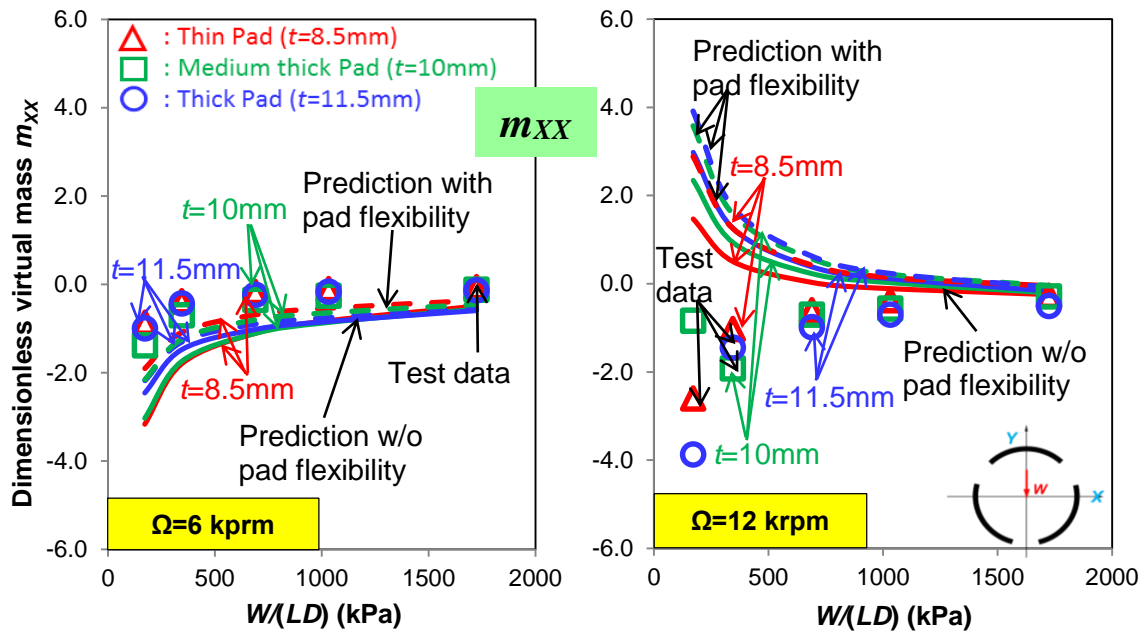
(a) c_{XX}



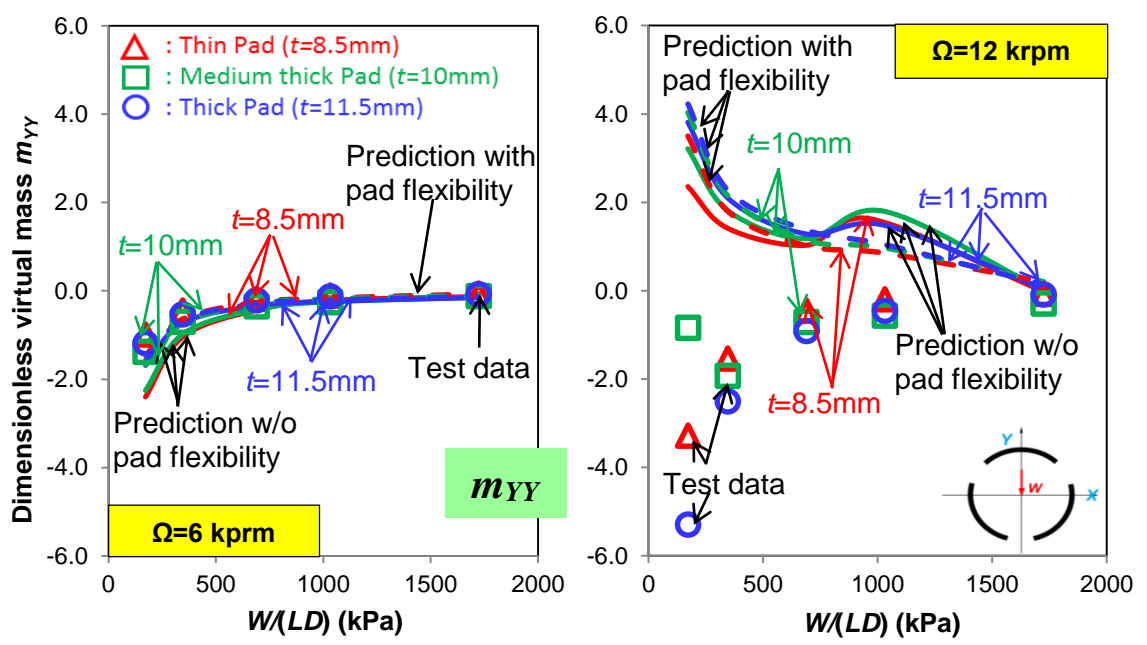
(b) c_{YY}

Fig. 21 Direct damping coefficients (c_{XX} and c_{YY}) versus unit load and two shaft speeds. Predictions (without and with pad flexibility) and test data from Gaines [24]. Results shown for thin, medium and thick pads. Copied from [31].

Figure 22 displays the virtual mass coefficients (m_{XX} , m_{YY}) versus unit load and operation at the low shaft speed of 6 krpm. The test results evidence smaller magnitudes for the added masses than the predictions otherwise show. The negative values denote the bearing dynamic stiffness hardens slightly as frequency increases, see Fig. 15. Most importantly, as the unit load increases, note (m_{XX} , m_{YY}) approach null values, thus indicating the real part of the complex stiffnesses (Z) does not show a frequency dependency. Similar results follow for operation at 12 krpm. Note that in the sub-synchronous frequency range ($\omega < \Omega$), the virtual mass coefficients have a negligible impact on the dynamic stiffnesses ($\text{Re}(Z)$).



(a) m_{xx}



(b) m_{yy}

Fig. 22 Direct virtual mass coefficients (m_{xx} and m_{yy}) versus unit load and shaft speed= 6krpm. Predictions (without and with pad flexibility) and test data from Gaines [24]. Results shown for thin, medium and thick pads.

Gaines [24] reports the percent reduction in the experimentally estimated dynamic force coefficients for the TPJB with thin pad sets ($t=8.5$ mm), with respect to those coefficients for the TPJB with thick pad sets ($t=11.5$ mm). Similarly, define $\Delta\bar{k}_{XX}$, $\Delta\bar{k}_{YY}$, $\Delta\bar{c}_{XX}$ and $\Delta\bar{c}_{YY}$ as the percent reduction in predicted direct dynamic force coefficients for the TPJB including pad flexibility with respect to those coefficients for the TPJB assuming rigid pads as

$$\Delta\bar{k}_{XX} = \left(1 - \frac{k_{XX,flex}}{k_{XX,rigid}}\right), \Delta\bar{k}_{YY} = \left(1 - \frac{k_{YY,flex}}{k_{YY,rigid}}\right) \quad (27.a)$$

$$\Delta\bar{c}_{XX} = \left(1 - \frac{c_{XX,flex}}{c_{XX,rigid}}\right), \Delta\bar{c}_{YY} = \left(1 - \frac{c_{YY,flex}}{c_{YY,rigid}}\right) \quad (27.b)$$

where $k_{XX,flex}$, $k_{YY,flex}$, $c_{XX,flex}$, $c_{YY,flex}$ are the predicted stiffness and damping coefficients assuming both flexible pads and flexible pivots; and $k_{XX,rigid}$, $k_{YY,rigid}$, $c_{XX,rigid}$, $c_{YY,rigid}$ are the predicted stiffness and damping coefficients assuming a rigid pad with a flexible pivot.

Table 10 lists the percentage reduction in bearing direct stiffness and damping coefficients at $W/(LD)=172$ kPa and 1,724 kPa and $\Omega=6$ krpm and 12 krpm. A positive value means including pad flexibility reduces a predicted force coefficient while a negative value means pad flexibility increases a predicted force coefficient.

Table 10 Percentage difference¹¹ between predicted dynamic force coefficients including pad flexibility and those assuming rigid pads at the lowest load ($W(LD)=172$ kPa) and the highest load ($W(LD)=1,724$ kPa). Frequency ranges from 0 to 200 Hz

Speed [rpm]	Unit load [kPa]	$\Delta \bar{k}_{xx}$	$\Delta \bar{k}_{yy}$	$\Delta \bar{c}_{xx}$	$\Delta \bar{c}_{yy}$
Thin pad sets, $t=8.5$ mm					
6,000	172	-5.7	-10.5	16.7	15.2
	1724	14.7	15.2	6.8	5.1
12,000	172	-3.3	-6.4	18.9	18.9
	1724	19.5	17.3	6.7	5.2
Medium thick pad sets, $t=10$ mm					
6,000	172	-5.6	-8.0	12.7	11.1
	1724	12.6	12.8	7.3	0.9
12,000	172	-4.2	-5.9	12.5	11.8
	1724	16.7	14.8	3.3	0.3
Thick pad sets, $t=11.5$ mm					
6,000	172	-3.7	-4.5	7.2	5.7
	1724	8.7	8.9	6.3	0.2
12,000	172	-3.8	-3.6	4.9	3.5
	1724	12.6	11.5	2.9	0.1
		Stiffness		Damping	

Pad flexibility influences significantly the dynamic force performance of the TPJB with thin pad sets ($t=8.5$ mm), since these pads are more flexible. Gaines [24] reports that the reduction in measured damping coefficients due to the increase in pad flexibility is more significant at a high rotor speed ($\Omega=12$ krpm). For the TPJBs with medium thick and the thickest pad sets, the reduction in predicted direct damping coefficients ($\Delta \bar{c}_{xx}$ and $\Delta \bar{c}_{yy}$) due to pad flexibility increases with an increase in rotor speed; while for the TPJB with the thin pad sets, $\Delta \bar{c}_{xx}$ and $\Delta \bar{c}_{yy}$ due to pad flexibility decreases with an increase in rotor speed. In general, $\Delta \bar{c}_{xx}$ and $\Delta \bar{c}_{yy}$ decrease as the load increases. The effect of pad flexibility on the direct stiffnesses is larger at a high rotor speed and with a large unit

¹¹ With respect to the predicted dynamic force coefficients assuming flexible pivot but rigid pad.

load. In addition, pad flexibility tends to increase slightly the direct stiffness coefficients at low loads, though it decreases the direct stiffnesses at high loads.

Closure Test data in Ref. [24] shows that pad flexibility reduces the journal eccentricity and the dynamic force coefficients. However, pad flexibility shows little effect on the film temperature. In the predictions, pad flexibility shows a more significant effect on the predicted static performance of the TPJB operating at a high rotor speed ($\Omega=12$ krpm). At the highest shaft speed and with the largest load ($\Omega=12$ krpm, $W/(LD)=1,724$ kPa), pad flexibility reduces the predicted journal eccentricity of the TPJB with thin pad sets ($t=8.5$ mm) by up to 32%. At a rotor speed of 12 krpm, including pad flexibility reduces the predicted maximum temperature by 11%.

The maximum pad deformations locate at both the pad leading and trailing edges and increases linearly with the applied load. At $\Omega=12$ krpm and $W/(LD)=1,724$ kPa, the maximum deformation for the thin pad is 25% of the cold pad clearance ($C_p=93$ μm). Along the pad leading and trailing edges, the deformation at the pad mid-plane ($Z = 0$) is up to 12% larger than that at the pad side edges ($Z = \pm 1/2 L$).

At the largest load ($W/(LD)=1,724$ kPa), stiffnesses of the TPJB with thin pad sets ($t=8.5$ mm) including pad flexibility are up to 20% smaller than those assuming a rigid pad. For the TPJB with thin pad sets ($t=8.5$ mm), including pad flexibility reduces the direct damping coefficients by up to 20%. The effect of pad flexibility on the predicted damping coefficients is more significant at the low unit load ($W/(LD)=172$ kPa).

In general, the predicted journal eccentricity and dynamic force coefficients including pad flexibility correlate well with test data in Ref. [24]. The bearing damping coefficients are overestimated at low unit load ($W/(LD)<1,032$ kPa) and the low rotor speed ($\Omega=12$ krpm). However, the maximum temperature is overestimated.

Example 2-Predicted Forced Performance for a Four-Pad LBP TPJB [26]

Branagan [26] reports predictions of performance for several fixed geometry journal bearings and TPJBs. The author considers two forms of pad deformation: thermal bending and mechanical bending. He regards the thermally and mechanically induced stresses as due to an applied moment acting on the pad. The pad deformation is accounted for as a change in pad clearance. One of the bearings analyzed in Ref. [26] is a four-pad TPJB with a LBP configuration.

Predictions using the current model are compared against the published predictions in Ref. [26] for both the static and the dynamic force performance characteristics of the four-pad TPJB. Table 11 lists the geometry of the TPJB, the lubricant type, and operating conditions. Figure 23 shows the schematic view of the four-pad TPJB with load-between-pad (LBP) configuration.

Table 11 Geometry, lubrication properties and operating conditions of a four-pad TPJB in Ref. [26]

Number of pads, N_{pad}	4	
Configuration	LBP	
Rotor diameter, D	120 mm	
Pad axial length, L	60 mm	
Pad thickness, t_p	22.6 mm	
Pad arc angle, Θ_P	75°	
Pivot offset	60%	
Dimensionless preload, \bar{r}_p	0	
Cold bearing clearance, $C_{B,cold}$	81.5 μm	
Cold pad clearance, $C_{P,cold}$	81.5 μm	
Hot bearing clearance, $C_{B,cold}$	79.4-81.1 μm	
Pad mass ¹ , m_P	0.98 kg	
Pad moment of inertia, I_P	0.16 kg·m ²	
Pad material	Elastic modulus ² , E	207 GPa
	Poisson's ratio, ν	0.289
Pivot type	Spherical pivot	
Supply oil pressure ³	1 bar	
Inlet oil temperature	33.5 °C	
Lubricant density	854 kg/m ³	
Lubricant viscosity at 33.5 °C, μ_0	52.1 mPa·s	
Viscosity temperature coefficient, α	0.0342 1/°C	
Lubricant specific heat capacity at 70 °C	1970 J/(kg·K)	
Specific load, W/LD	688 kPa- 3,441 kPa	
Journal speed, Ω	4000 rpm	

¹ Ref. [26] does not offer the pad mass and the pad moment of inertia. Magnitudes shown in Table 11 are estimated using Solidworks©.

² Pad material elastic modulus is taken from Ref. [26].

³ Ref. [26] does not report the supply oil pressure. The current predictions are obtained assuming the inlet oil pressure is 0.1 bar.

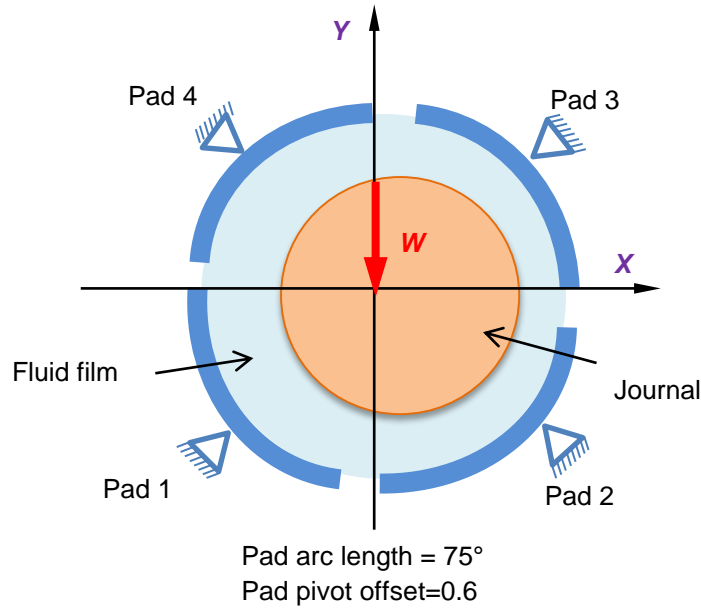


Fig. 23 Schematic view of a four-pad TPJB in Ref. [26]. Load between pads.

Pivot flexibility In Ref. [26], Branagan selects $K_{piv}=870$ MN/m (5×10^6 lbf/in) as the stiffness of the spherical pivot. The current model adopts the same pivot stiffness.

Pad flexibility Branagan [26] considers the pad thermal expansion and the pad thermal bending as a change in bearing clearance (ΔC_B) and pad clearance (ΔC_P), respectively. The bearing clearance decreases by an average heating of the pad [26],

$$\Delta C_B = -\frac{\alpha}{\ln r_0} \frac{T_1 - T_2}{R_p} [r_0 - \ln r_0 - 1] \quad (28)$$

where $\alpha = 1.17 \times 10^{-5}$ 1/C° is the pad thermal expansion coefficient from Ref. [26] and $r_0 = (R_p + t)/R_p$ with R_p as the pad radius and t as the pad thickness. T_1 and T_2 are the average circumferential temperatures for the Babbitt ($T_{Babbitt}$) and the back of a pad (T_{back}), respectively. Branagan [26] solves for $T_{Babbitt}$ by matching the heat conduction from the film to the finite difference solution for the heat flow in the pad. He indicates that a convection boundary condition on the back of the pads cannot be adequately defined. In general, the pads are surrounded by oil, named as “sump oil”, churned by pad

motion. Branagan [26] set $T_{back} = T_{sump}$ since the “sump oil” cools the back of the pads by forced convection. The temperature of the “sump oil” is determined by a global heat balance,

$$T_{sump} = T_{in} + \frac{\varepsilon P_w}{\rho c_v Q_s} \quad (29)$$

where T_{in} is the supply oil temperature, P_w is the drag power loss in the film, $\varepsilon=100\%$ is the fraction of shear loss carried by the oil, ρ is the oil density, c_v is the oil specific heat and Q_s is total supply oil flow rate.

Branagan [26] determines the change in pad clearance (ΔC_p) using a curved beam model with a bending moment M_b (thermal and mechanical) acting at its ends, i.e.,

$$\Delta C_p = -\frac{M_b}{AE} (r_0 - 1) \frac{4 \left[1 - r_0^2 - 1 - 2 \ln r_0 \right]}{r_0^2 - 1 - 2 r_0 \ln r_0} \quad (30)$$

where $A=L \times t$ is the area of a pad cross section and E is the elastic modulus of the pad. A thermally induced bending moment and a mechanical bending moment due to fluid film pressure are determined from

$$M_{thermal} = -\frac{\alpha \cdot E \cdot A \cdot R_p \cdot (T_1 - T_2)}{4 \cdot (r_0 - 1) \cdot \ln(r_0)} \left[r_0^2 - 1 - 2 \cdot r_0 \cdot \ln(r_0) \right] \quad (31)$$

$$M_{pressure} = -R_p^2 L \frac{2}{3} \int_{\theta_l}^{\theta_p} P(\theta) \sin(\theta - \theta_p) d\theta \quad (32)$$

where L is the pad width, θ_p is the location of the pad pivot, θ_l is the location of the pad leading edge and $P(\theta)$ is the fluid film pressure at the bearing mid-plane.

In the current model, the element size along the circumferential direction is 2° (default setting). Presently, the grid density for the pressure field on one pad surface is $N_{cir} \times N_{axial} = 29 \times 19$. Figure 24 shows a simple pad structural model built in ANSYS© with the same mesh. Since predictions in Ref. [26] neglect the Babbitt layer, the FE pad model does not consider it either. Similar boundary conditions as those in Desbordes *et al.* [17] are applied on the FE pad model.

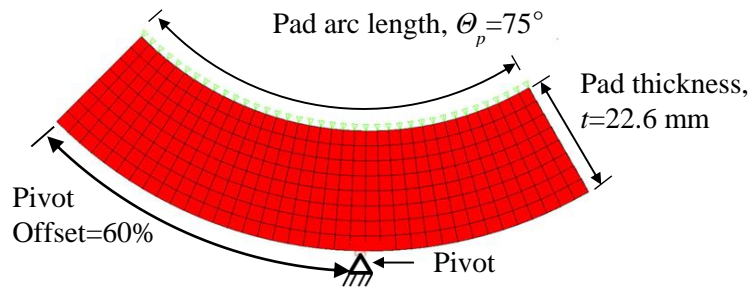


Fig. 24 FE pad model of tilting pad in Ref. [26]

The current pad FE structural model (in Figure 24) considers the pad deflection due to fluid film pressure. However, Branagan [26] takes both the thermal and mechanical deflection of each pad into account. Table 12 lists the change in pad clearance (ΔC_B) due to the pad thermal expansion and the change in bearing clearance (ΔC_P) due to the pad thermal bending in Ref. [26]. To approximate Branagan's results, the current model uses the same ΔC_B and ΔC_P listed in Table 12 to account for the pad deflection due to temperature change.

Table 12 Predicted changes in bearing pad clearance due to pad thermal expansion (ΔC_B) and change in pad clearance due to pad thermal bending (ΔC_P). Data from Ref. [26]. Nominal bearing clearance $C_B=81.5 \mu\text{m}$, pad clearance $C_P=81.5 \mu\text{m}$ and pad preload $\bar{r}_p=0$.

Unit load (kPa)	Pad number	ΔC_B (μm)	ΔC_P (μm)	Operating Preload ⁴ (-)
688	1	-1.25	3.91	0.06
	2	-1.43	4.48	0.07
	3	-0.85	2.65	0.04
	4	-0.74	2.32	0.04
1,377	1	-1.43	4.49	0.07
	2	-1.79	5.58	0.08
	3	-0.73	2.28	0.03
	4	-0.56	1.76	0.03
2,065	1	-1.50	4.67	0.07
	2	-1.67	5.20	0.08
	3	-0.33	1.04	0.02
	4	-0.28	0.89	0.01
2,753	1	-1.67	5.20	0.08
	2	-1.79	5.59	0.09
	3	-0.27	0.85	0.01
	4	-0.22	0.68	0.01
3,441	1	-1.80	5.62	0.08
	2	-1.89	5.93	0.09
	3	-0.23	0.71	0.01
	4	-0.17	0.54	0.01

⁴ Resultant pad preload due to pad thermally induced deflection, $\bar{r}_p = 1 - C_B + \Delta C_B / C_P + \Delta C_P$. Note the nominal pad reload $\bar{r}_p = 0$.

In accordance with Ref. [26], the current predictions account for the heat convection between the fluid film and the journal surface⁵. The lubricant inlet thermal mixing coefficient (λ) is 0.8, since the rotational speed is low ($\Omega=4,000$ rpm). This section shows the current predictions with and without accounting for pad flexibility. Recall that the current model accounts for pivot flexibility ($K_{piv}=870$ MN/m).

Journal eccentricity Figure 25 shows the journal eccentricity ratio (e/C_p) predicted by the current model and that in Ref. [26] agree for most loads. Note that $C_p = 81.5$ μm is the cold pad clearance. Pad flexibility produces a negligible effect on the journal eccentricity. The ratio between the pad maximum deformation (u_{max}) and the pad clearance (C_p) increases as the static load increases. The pad maximum deformation (u_{max}/C_p) is only 10% even at the largest load $W/(LD)=3,441$ kPa, thus indicating the pad is not very flexible.

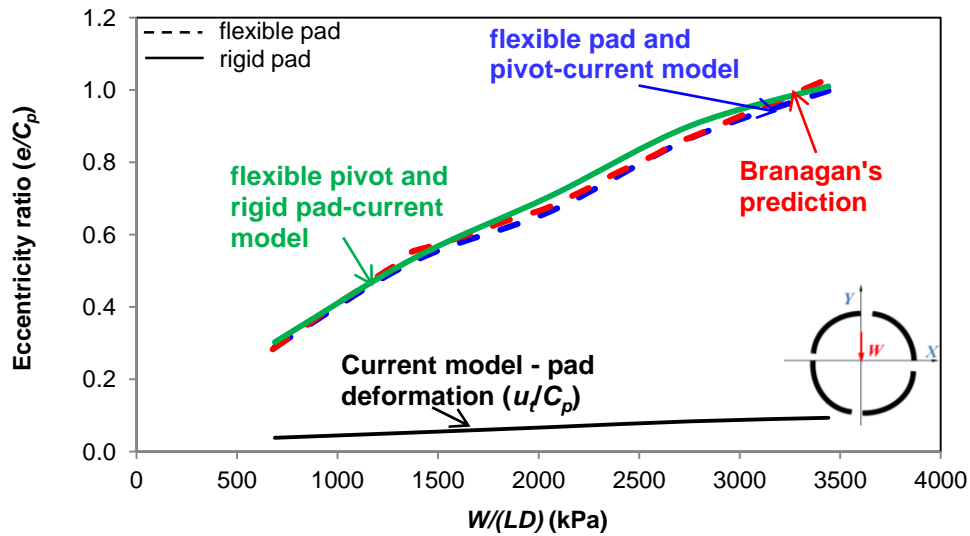
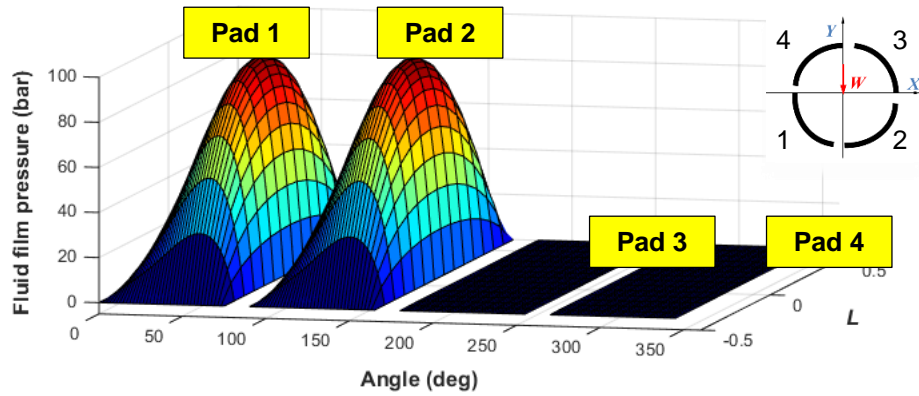


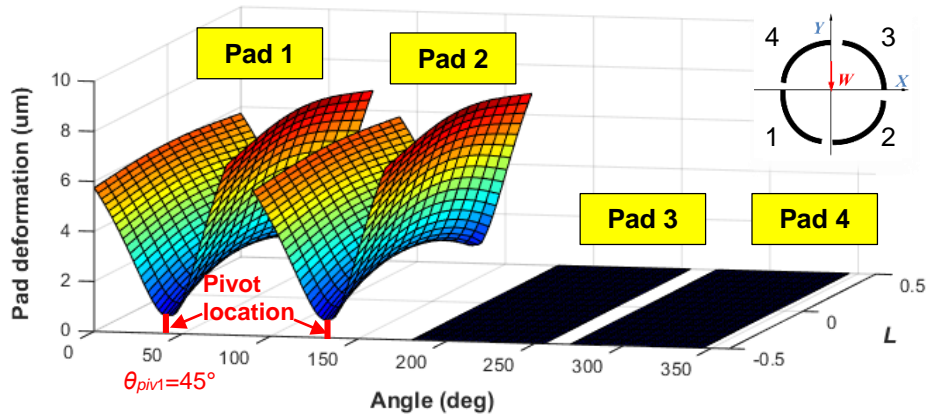
Fig. 25 Journal eccentricity ratio (e/C_p) for example TPJB [26]. Current model predictions vs. predictions in Ref. [26]; ($\Omega=4$ krpm; $W/(LD)=688$ kPa to 3,441 kPa)

⁵ Predictions and Ref. [26] use the average fluid film temperature as the journal temperature.

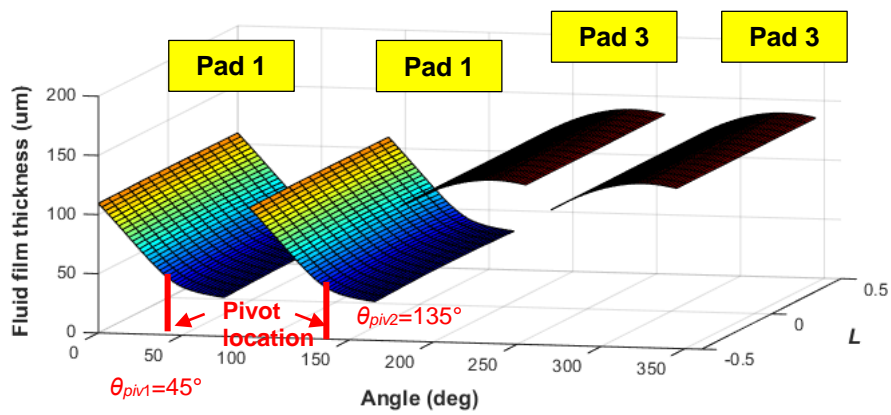
Figure 26 depicts the pressure, fluid film thickness and pad surface deformation field for operation at 4 krpm and at the largest load ($W/(LD)=3,441$ kPa). As the upper two pads are unloaded ($P=0$), they have no deformation. The maximum pad deformation locates at the pad trailing edge mid-plane ($Z=0$) (pivot offset: 60%). Note that the pad deformation along the pad width (Z) is not uniform. The minimum film thickness occurs at the pad trailing edge.



(a) Fluid film pressure



(b) Pad deformation



(c) Fluid film thickness

Fig. 26 (a) Fluid film pressure, (b) pad surface deformation, and (c) fluid film thickness. Shaft speed $\Omega=4$ krpm and static load $W/(LD)=3,441$ kPa.

Figure 27 depicts the fluid film pressure at the bearing mid-plane for loads $W/(LD)=1,377$ kPa, 2,065 kPa and 3,441 kPa and operation at 4 krpm. Though the nominal pad preload is nil ($\bar{r}_p = 0$), at $W/(LD)=1,377$ kPa, the upper two pads (#3 and #4) are loaded. For modeling purposes, the upper two pads tilt to generate a minute fluid film pressure ($P>0$). However, at 3,441 kPa, the fluid film pressure on the upper pads (#3 and 4) is zero. Interestingly, at $W/(LD)= 2,065$ kPa, there is fluid film pressure generated on pad #4, albeit the pressure on pad #3 is zero.

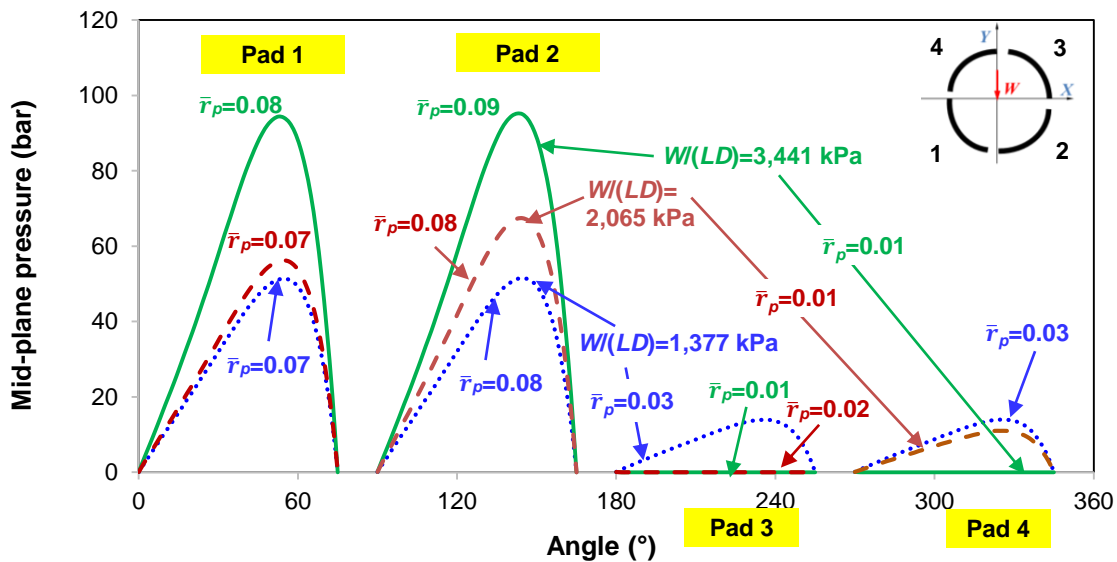


Fig. 27 Fluid film pressure at bearing mid-plane. Current predictions. Operating preload on each pad noted. Rotor speed $\Omega=4$ krpm and unit loads $W/(LD)=1,377$ kPa, 2,065 kPa and 3,441 kPa.

Maximum film pressure Figure 28 depicts a comparison between the predicted maximum fluid film pressure and predictions in Ref. [26]. At $W/(LD)=3,403$ kPa, the current maximum fluid film pressure becomes 16% smaller than predictions in Ref. [26]. For the current predictions, pad flexibility shows no effect on the peak pressure. The reason for the discrepancy with data in Ref. [26] is that the FE pad model predicts a surface deformation field over the whole pad whereas Branagan [26] only accounts for

the pad deformation as a change in pad clearance due to a bending moment created by the pressure field⁶.

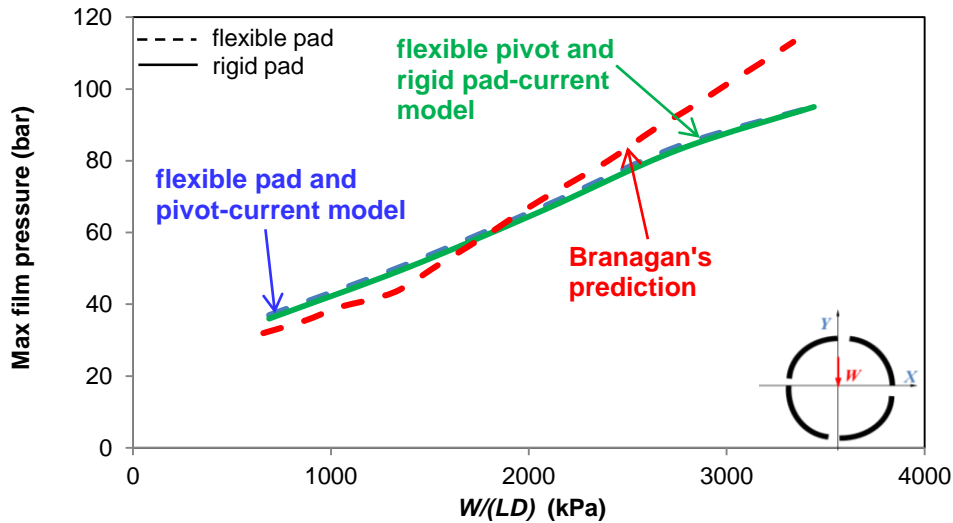


Fig. 28 Maximum fluid film pressure for example TPJB [26]. Current model predictions vs. predictions in Ref. [26]; ($\Omega=4$ krpm; $W/(LD)=688$ kPa to 3,441 kPa)

Maximum film temperature Figure 29 shows the predicted maximum fluid film temperature and that in Ref. [26] versus applied load. Note that Branagan [26] reports the maximum Babbitt surface temperature. Current predictions including pad flexibility are slightly lower (within 2°C) than those in Ref. [26]. Though the effect of pad flexibility is not significant, it tends to reduce the maximum temperature as the load increases.

⁶ See Eqs. (30, 32).

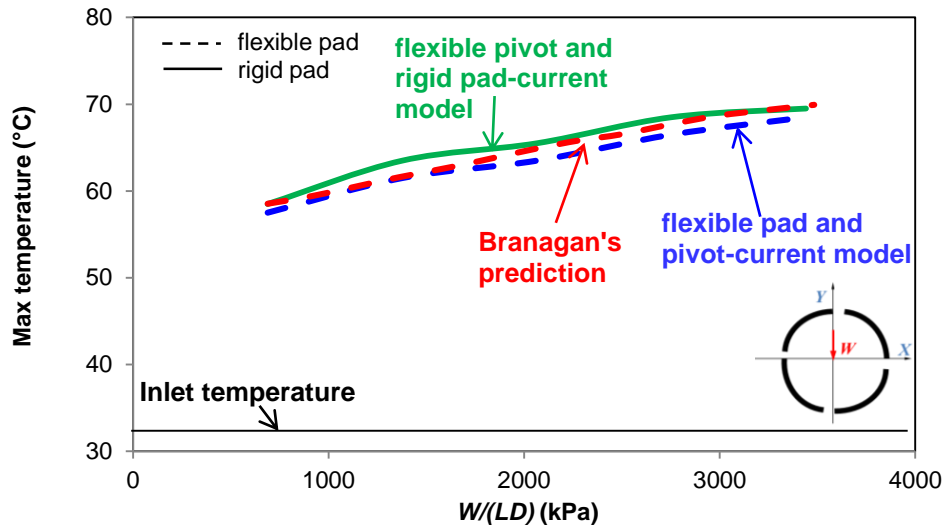
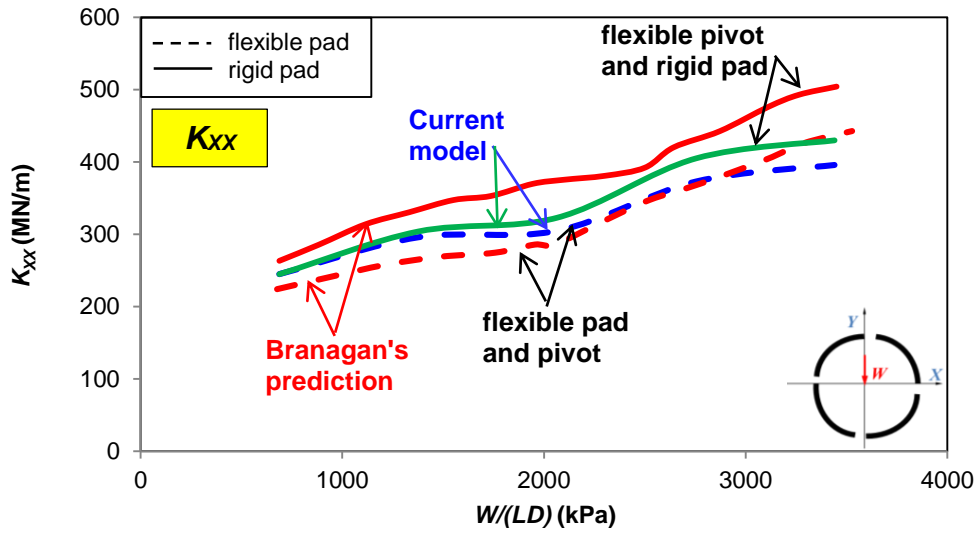


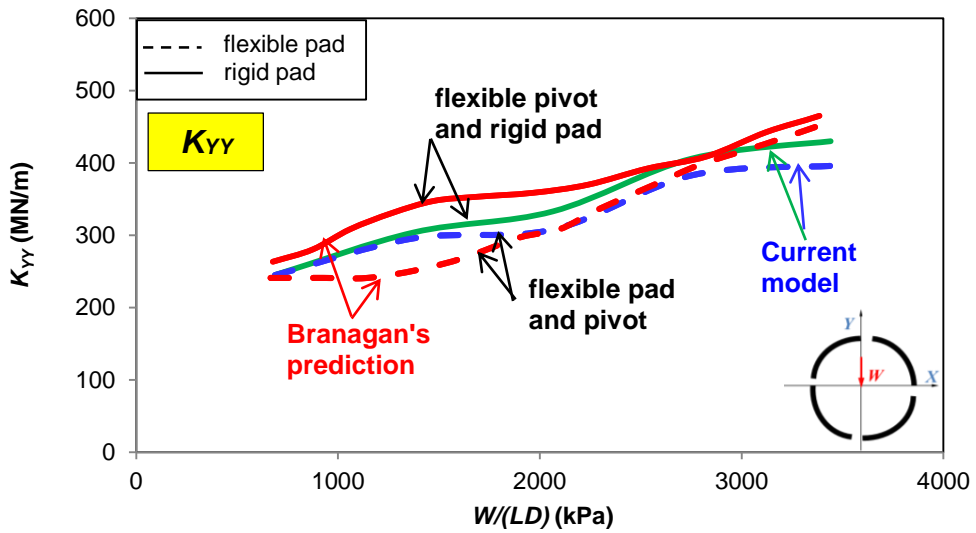
Fig. 29 Maximum fluid film temperature for example TPJB [26]. Current model predictions vs. predictions in Ref. [26]; ($\Omega=4$ krpm; $W/(LD)=688$ kPa to 3,441 kPa)

TPJB stiffness and damping force coefficients In Ref. [26], Branagan uses a K-C model and reduces the dynamic force coefficients at a whirl frequency of $\omega=1$ krpm, whereas the rotor speed (Ω) is at 4 krpm (nonsynchronous speed analysis with $\omega/\Omega=1/4$). Figures 30 and 31 show the asynchronous shaft speed direct-dynamic-force coefficients predicted using the current model. Both the current model and Branagan's predictions show a difference between the direct force coefficients, i.e., $K_{XY} \neq K_{YY}$ and $C_{XX} \neq C_{YY}$. The difference is more significant in Branagan's predictions. Recall that Branagan presents the dynamic force coefficients with and without the consideration of pad flexibility.

In Figure 30, the current predictions for K_{XX} and K_{YY} correlate well with the predictions in Ref. [26]. The stiffnesses increase with an increase in load. Though the effect of pad flexibility tends to reduce the stiffness coefficients and increases as the load increases, the reduction in direct stiffnesses is not significant. At the largest load ($W/(LD)=4,021$ kPa), including pad flexibility reduces the direct stiffnesses by 7%.



(a) K_{xx}

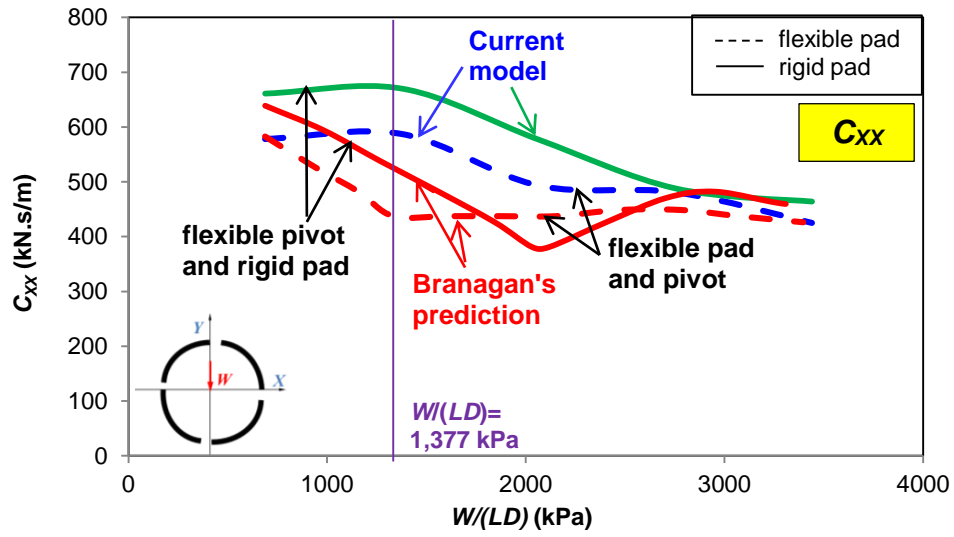


(b) K_{yy}

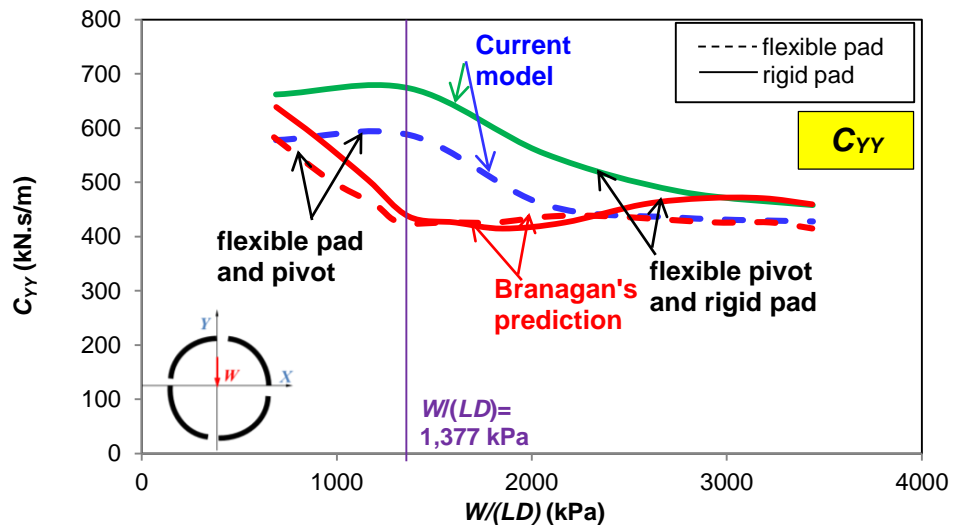
Fig. 30 Asynchronous direct stiffness coefficients (K_{xx} and K_{yy}) for example TPJB [26]. Current model predictions vs. predictions in Ref. [26]; ($\omega=1$ krpm; $\Omega=4$ krpm; $W/(LD)=688$ kPa to 3,441 kPa)

Figure 31 depicts the asynchronous speed ($\omega/\Omega=1/4$) damping coefficients versus specific load. At $W/(LD)<1,377$ kPa, C_{XX} and C_{YY} increase slightly with applied load; whereas, since the upper two pads become unloaded for $W/(LD)>1,377$ kPa, C_{XX} and C_{YY} decrease with applied load. At a large load, $W/(LD)>2,500$ kPa, the current model predictions start to approach the predictions in Ref. [26]. However, at $W/(LD)=1,377$ kPa, the current predictions including pad flexibility are up to 34% larger than the Branagan's predictions including pad flexibility [26].

The current model predictions show that including pad flexibility reduces the damping coefficients by up to 21% at the lowest unit load ($W/(LD)=688$ kPa) and by 6% at the largest unit load ($W/(LD)=3,441$ kPa). In Ref. [26], including pad flexibility reduces the damping coefficients by up to 8% at the smallest unit load ($W/(LD)=619$ kPa) and by 7.3% at the largest load ($W/(LD)=3,403$ kPa). Similar to bearing stiffnesses, at $W/(LD)>1,856$ kPa, the bearing damping coefficients decrease since the upper two pads become unloaded (see Figure 27).



(a) C_{xx}



(b) C_{yy}

Fig. 31 Asynchronous direct damping coefficients (C_{yy} and C_{yx}) for an example TPJB [26]. Current model predictions vs. predictions in Ref. [26]; ($\omega=1$ krpm; $\Omega=4$ krpm; $W/(LD)=688$ kPa to 3,441 kPa)

Closure For the example analyzed, a TPJB with both flexible pads and pivots, pad flexibility shows little influence on the predicted static load results (i.e., journal eccentricity, maximum pressure and maximum temperature). At the largest load $W/(LD)=3,441$ kPa, the maximum pad deformation is 10% of the cold pad clearance thus indicating the pad is quite rigid. However, including pad flexibility reduces the bearing dynamic force coefficients, in particular the damping coefficients. For the current model, pad flexibility reduces the direct stiffnesses as the applied load increases. However, for the direct damping coefficients, the influence of pad flexibility is more significant at low loads, $W/(LD)<2,000$ kPa.

Note that Branagan's bearing [26] has stiffer pads, with shorter arc length and larger pad thickness, than those in the bearings tested by Gaines [24]. Under a uniform pressure (1 MPa), the trailing edge deformation of Gaines' thickest pad ($t=11.5$ mm) is 40% larger than that of the pad in Ref.[26]. At the largest load ($W/(LD)=1,724$ kPa) in Ref. [24], u_{max}/C_p for Gaines' thickest pad bearing is 10% while that for Malcher's bearing in Ref.[26] is 7%. Thus, the effect of pad flexibility on the force performance of this bearing is not as pronounced as that in those bearing tested by Gaines [24].

CONCLUSIONS

Accurate characterization of mechanical components presently requires physical models to have ever increasing complexity that include all relevant geometrical aspects, material properties and fluid flow conditions, as per installation and operation, even envisioning operation well beyond their intended original design [31]. This thesis extends a computational thin film fluid flow model for TPJBs to include both pad and pivot flexibility on the prediction of the static and dynamic forced performance of typical bearings.

Presently, a FE structural commercial model builds the stiffness matrix for pad displacements. This stiffness matrix is condensed to show only the pad surface deformations due to an applied pressure field. The deformation field is integrated into the evaluation of film thickness for solution of the Reynolds equation delivering the hydrodynamic pressure field. A small amplitude perturbation analysis produces equations for the zeroth and first-order pressure fields from which the load capacity and a multitude of complex stiffness for each pad are determined. A pad assembly method with frequency reduction delivers the 4x4 stiffnesses and damping coefficients for lateral displacements of the shaft center. In a *K-C-M* model, curve fits of the force/displacement versus excitation frequency also deliver the bearing stiffness, damping, and virtual mass coefficients.

In comparisons to experimental data and predictions in Refs. [24,26], current predictions including both pad and pivot flexibility correlate better than the predictions solely including pivot flexibility. For a three-pad TPJB with thin pad sets in Ref. [24], pad flexibility reduces significantly the journal eccentricity by up to 32% and the maximum temperature by up to 11%, in particular for operation at a high rotor speed ($\Omega=12$ krpm). The four-pad LBP TPJB in Ref. [26] has stiffer pads. The maximum pad deformation is 10% of the cold pad clearance at the largest load. Including pad flexibility has little effect on the journal eccentricity and the peak fluid film temperature.

In general, the dynamic force coefficients are reduced due to pad flexibility. For the three pad TPJBs in Ref. [24], pad flexibility causes up to a 20% reduction in predicted bearing stiffness. However, both test data in Ref. [24] and current predictions show an increase in bearing direct stiffnesses for the TPJB at a low load ($W/(LD) < 689$ kPa). Pad flexibility shows a more significant effect on the predicted dynamic force coefficients than the experimental results evidence, in particular at a higher rotor speed ($\Omega = 12$ krpm), thus indicating the pad structural FE model delivers a smaller stiffness than that of the actual test pad. Measurements for the structural stiffness of the pads are needed to further improve the FE model. Predictions including pad flexibility deliver damping coefficients up to 20% lower than those obtained with a rigid pads model. Reducing the pad thickness from 11.5 mm to 8.5 mm causes also a reduction of up to 34% in the predicted direct damping coefficients.

For a four-pad TPJB with a LBP configuration [26], current predictions include both the pad thermal expansion and the pad thermal bending using the resultant bearing and pad clearance listed in Ref.[26]. Including pad flexibility reduces the direct stiffnesses by up to 7% at the largest load and the damping coefficients by up to 21% at the smallest load.

The thesis also introduces a parametric study to quantify the influence of pad flexibility on the rotordynamic force coefficients of sample TPJBs. Generally, pad flexibility shows a more pronounced effect at a large Sommerfeld number ($S > 0.8$). For the sample TPJB with three pads of increasing preload = 0, 0.25 (baseline) and 0.5 under LBP or LOP configurations, the bearing pads vary from being rigid to flexible ($k_{pad} = \infty, 3.15$ and 7.33). The operating journal eccentricity and dynamic force coefficients are reduced due to pad flexibility in particular for operation at a large Sommerfeld number ($S > 0.8$). However, for the LOP and LBP bearings with a 0.25 pad preload, pad flexibility increases the stiffness coefficients at large Sommerfeld number ($S > 0.8$). Pad flexibility shows a more pronounced effect for the TPJB with null pad preload at a large Sommerfeld number.

The thesis further considers a sample TPJB with four pads with null preload (LBP or LOP configurations). The pads have stiffnesses $k_{pad} = \infty, 24.4$ and 4.1 (rigid to soft). Pad flexibility shows a more pronounced effect, generally decreasing the bearing dynamic force coefficients along the loaded direction for the TPJB with LOP configuration. The bearing stiffnesses for the bearing with the softest pads ($k_{pad}=4.1$) are 14% smaller than those for the bearing with rigid pads. The bearing damping coefficients with rigid pads are up to 19% larger than that with the softest pads ($k_{pad}=4.1$).

Future work should focus on the accurate prediction of pad thermal expansion and pad thermal bending to render the actual bearing and pad clearances. Besides the current flooded lubricated condition, the model should also include a directed lubricated condition and also fluid starvation to accurately predict the force performance for more realistic types of bearings.

REFERENCES

- [1] Al-Ghasem, A.M., Childs, D.W., 2006, "Rotordynamic Coefficients Measurements Versus Predictions for a High-Speed Flexure-Pivot Tilting-Pad Bearing (Load-Between-Pad Configuration)," *ASME J. Eng. Gas Turbines Power*, **128**, pp. 896-906.
- [2] Dimond, T., Younan, A., and Allaire, P., 2011, "A Review of Tilting Pad Bearing Theory," *International Journal of Rotating Machinery*, 2011, pp. 1-23.
- [3] Dimond, T., Younan, A., and Allaire, P., 2010, "Comparison of Tilting Pad Journal Bearing Dynamic Full Coefficient and Reduced Order Models Using Modal Analysis," *ASME J. Vib. Acoust.*, **132**, pp. 051009 1-10.
- [4] Lund, J.W., 1964, "Spring and Damping Coefficients for the Tilting-Pad Journal Bearing," *ASLE Trans.*, **7**, pp. 342-352.
- [5] Hagg, A.C., and Sankey, G.O., 1956, "Some Dynamic Properties of Oil-Film Journal Bearings with Reference to the Unbalance Vibration of Rotors," *J. Appl. Mech.*, **23**, pp. 302-306.
- [6] Nicholas, J.C., Gunter, F.J., and Allaire, P.E., 1979, "Stiffness and Damping Coefficients for the Five-Pad Tilting-Pad Bearing," *ASLE Trans.*, **22**, pp.113-124.
- [7] Rodriguez, L.E. and Childs, D.W., 2006, "Frequency Dependency of Measured and Predicted Rotordynamic Coefficients for a Load-on-Pad Flexible-Pivot Tilting-Pad Bearing," *ASME J. Trib.*, **128**, pp. 388-395.
- [8] Delgado, A., Vannini, G., Ertas, B., Drexel, M. and Naldi, L., 2011, "Identification and Prediction of Force Coefficients in a Five-Pad and Four-Pad Tilting Pad Bearing for Load-on-Pad and Load-Between-Pad Configurations," *ASME J. Eng. Gas Turbines Power*, **133**, pp. 092503 1-9.
- [9] Carter, C., and Childs, D.W., 2009, "Measurements versus Predictions for the Rotordynamic Characteristics of a Five-Pad Rocker-Pivot Tilting-Pad Bearing in Load- Between-Pad Configuration," *ASME, J. Eng. Gas Turbines Power*,

- 131**, pp. 012507 1-9.
- [10] Nilsson, L., 1978, "The Influence of Bearing Flexibility on the Dynamic Performance of Radial Oil Film Bearings," Proc. 5th Leeds-Lyon Symposium on Tribology, **5**, pp.311-319.
- [11] Ettles, C.M., 1980, "The Analysis and Performance of Pivoted Pad Journal Bearings Considering Thermal and Elastic Effects," ASME J. Lubr. Technol., **102**, pp. 182-192.
- [12] Lund, J.W. and Pedersen, L.B. 1987, "The Influence of Pad Flexibility on the Dynamic Coefficients of a Tilting Pad Journal Bearing," ASME J. Tribol., **109**, pp. 65-70.
- [13] Brugier, D. and Pascal, M.T., 1989, "Influence of Elastic Deformations of Turbo-Generator Tilting Pad Bearings on the Static Behavior and on the Dynamic Coefficients in Different Designs," ASME J. Tribol., **111**, pp. 364-371.
- [14] Earles, L.L., Palazzolo, A.B. and Armentrout, R.W., 1990 "A Finite Element Approach to Pad Flexibility in Tilt Pad Journal Bearings: Part I – Single Pad Analysis," ASME J. Tribol., **112**, pp. 169-177.
- [15] Earles, L.L., Palazzolo, A.B. and Armentrout, R.W., 1990 "A Finite Element Approach to Pad Flexibility in Tilt Pad Journal Bearings: Part II – Assembled Bearing and System Analysis," ASME J. Tribol., **112**, pp. 178-182.
- [16] Desbordes. H., Fillon, M., Frene, J. and Chan Hew Wai, C., 1994, "Dynamic Analysis of Tilting Pad Journal Bearing – Influence of Pad Deformation," ASME J. Tribol., **116**, pp. 379-384.
- [17] Desbordes. H., Fillon, M., Frene, J. and Chan Hew Wai, C., 1995, "The Effects of Three Dimensional Pad Deformations on Tilting-Pad Journal Bearings under Dynamic Loading," ASME J. Tribol., **117**, pp. 379-384.
- [18] Sudheer Kumar Reddy, D., Swarnamani, S., and Prabhu, B.S., 2000, "Thermoelastohydrodynamic Analysis of Tilting Pad Journal Bearing – Theory and Experiments" Tribology Transactions, **43**, pp.82-90.

- [19] Wilkes, J. C., 2011, "Measured and Predicted Rotor-Pad Transfer Functions for a Rocker-Pivot Tilting-Pad Bearing," PhD. Thesis, Mechanical Engineering, Texas A&M University, College Station, TX.
- [20] Hagemann, T., Kukla, S., and Schwarze, H., 2013, "Measurements and Prediction of the Static Operating Conditions of a Large Turbine Tilting-Pad Bearing under High Circumferential Speeds and Heavy Loads," Proceedings of ASME Turbo Expo 2013, Paper GT2013-95004, June 3-7, San Antonio, USA.
- [21] Kukla, S., Hagemann, T., and Schwarze, H., 2013, "Measurements and Prediction of the Dynamic Characteristics of a Large Turbine Tilting-Pad Bearing under High Circumferential Speeds," Proceedings of ASME Turbo Expo 2013, Paper GT2013-95074, June 3-7, San Antonio, USA.
- [22] San Andrés, L., and Tao, Y., 2013, "The Role of Pivot Stiffness on the Dynamic Force Coefficients of Tilting Pad Journal Bearings," ASME J. Eng. Gas Turbines Power, **11**, pp. 112515.
- [23] Tao, Y., 2012, "A Novel Computational Model for Tilting Pad Journal Bearings with Soft Pivot Stiffnesses," MS. Thesis, Mechanical Engineering, Texas A&M University, College Station, TX.
- [24] Gaines, J., 2014, "Examining the Impact of Pad Flexibility on the Rotordynamic Coefficients of Rocker-Pivot-Pad Tiling-Pad Journal Bearings," MS. Thesis, Mechanical Engineering, Texas A&M University, College Station, TX.
- [25] Gaines, J., and Childs, D., 2015, "The Impact of Pad Flexibility on the Rotordynamic Coefficients of Tilting-Pad Journal bearings," Proceedings of ASME Turbo Expo 2015, Paper GT2015-42289, June 15-19, Montréal, Canada.
- [26] Branagan, L.A., 1988, "Thermal Analysis of Fixed and Tilting Pad Journal Bearing Including Cross-Film Viscosity Variations and Deformation," Ph.D. Dissertation, University of Virginia, Charlottesville, Virginia.
- [27] San Andrés, L., 2010, "Note 16. Analysis of Tilting Pad Bearings," Modern

- Lubrication Theory, Texas A&M University Digital Libraries, <http://repository.tamu.edu/handle/1969.1/93256>.
- [28] Lund, J.W., and Sternlicht, B., 1962, “Rotor-Bearing Dynamics with Emphasis on Attenuation,” *J. Basic Eng.*, **84**, pp. 491-502.
- [29] Warner, P.C., 1963, “Static and Dynamic Properties of Partial Journal Bearings,” *J. Basic Eng.*, **85**, pp. 247-257.
- [30] Constantinescu, V.N., 1967, “The Pressure Equation for Turbulent Lubrication,” *Proc. Of the Conference on Lubrication and Wear, London*, pp. 132.
- [31] San Andrés, L., and Li, Y., 2015, “Effect of Pad Flexibility on the Performance of Tilting Pad Journal Bearings - Benchmarking a Predictive Model,” *Proceedings of ASME Turbo Expo 2015, Paper GT2015-42776, June 15-19, Montréal, Canada*.
- [32] Boedo, S., and Booker, J. F., 1997, “Mode Stiffness Variation in Elastohydrodynamic Bearing Design,” *Elastohydrodynamics '96*, D. Dowson et al., eds., Elsevier, pp. 685–697.
- [33] American Society for Metals, 1985, *Metals Handbook*, 9th ed., 3, pp. 802-822.
- [34] Cverna, F., 2002, *ASM Ready Reference: Thermal Properties of Metals*, ASM International, Chapt.2.
- [35] Timoshenko, S., and Goodier, J.N., 1951, *Theory of Elasticity*, New York, McGraw-Hill, Chap.6.
- [36] Armenakas, A.E., 2005, *Advanced Mechanics of Materials and Applied Elasticity*, Taylor & Francis, Boca Raton, Chap.13.
- [37] Reddy, J. N., 2002, *Energy Principles and Variational Methods in Applied Mechanics*, John Wiley & Sons, New York, Chap.5.
- [38] Kassimali, A., 1999, *Structural Analysis*, PWS Pub. Pacific Grove. Chap. 7.
- [39] Gere, J.M., 2013, *Mechanics of Materials*, Cengage Learning, Stamford, Chap.6.
- [40] Paul E. L., 2007, *Curved Beams*, UW Courses Web Server,

<http://courses.washington.edu/me354a/Curved%20Beams.pdf>

- [41] San Andrés, L., Tao, Y., and Li, Y., 2014, “Tilting Pad Journal Bearing: On Bridging the Hot Gap Between Experimental Results and Model Predictions,” *ASME J. Eng. Gas Turbines Power*, **137**, pp. 022505.
- [42] Someya, T., 1989, *Journal-Bearing Databook*, Springer-Verlag, Berlin, Heidelberg, Chap. 1.

APPENDIX A- PAD DEFLECTION AND PAD STIFFNESS COEFFICIENT [35]

Analyses on pad flexibility available in the archival literature commonly adopt a beam bending or flexural model to estimate pad deformations. Often enough, the analyses ignore some important parameters affecting pad flexibility, like the pad thickness and arc length, and the Babbitt layer. This appendix presents a novel model, accounting for the effect of the pad geometry and material properties, to estimate the pad surface deformation.

The simple model adopts a unit-load method [35-37]. Regard half of the pad as a cantilevered curved beam (see Figure A.1) and with a uniform pressure (\bar{p}) acting on it. The curved beam has radius R , thickness t , width L and arc length θ_t . The elastic modulus of the pad material is E .

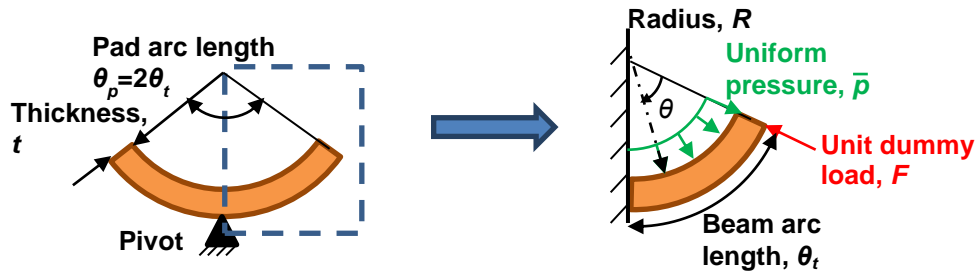


Fig. A. 1 simplified cantilevered beam model for a pivoted pad

The bending moment (M_p) at $\theta=0$ caused by a uniform pressure (\bar{p}) is

$$M_p = \int_0^{\theta} \bar{p} L R d\theta \cdot R \sin \theta = \bar{p} L R^2 \cdot (1 - \cos \theta) \quad (\text{A.1})$$

Apply a virtual radial load (F) at the end of the curved beam. The bending moment (M_F) caused by this force is

$$M_F = -F \cdot R \sin(\theta) \quad (\text{A.2})$$

The total bending moment (M_b) at θ is

$$M_b(\theta) = M_p + M_F \quad (\text{A.3})$$

$$\bar{p} L R^2 \cdot (1 - \cos \theta) - F \cdot R \sin(\theta)$$

The total work (W) performed by the external loads (\bar{p} and F) is

$$W = \int_0^{\theta_i} \frac{M_b^2 R d\theta}{2EI} = \int_0^{\theta_i} \frac{[\bar{p} L R^2 \cdot (1 - \cos \theta) - F \cdot R \sin(\theta)]^2}{2EI} R d\theta \quad (\text{A.4})$$

where $I=(Lt^3)/12$ is the area moment of inertia of the beam cross-section. According to Castigliano's theorem [38], the beam displacement along the same direction as the applied force (F) is

$$u = \frac{\partial W}{\partial F} = \int_0^{\theta_i} \frac{M_b(\theta)}{EI} \frac{\partial M_b(\theta)}{\partial F} R d\theta = \int_0^{\theta_i} \frac{[\bar{p} L R^2 \cdot (1 - \cos \theta) - F \cdot R \sin(\theta)]}{EI} \cdot R \sin(\theta) R d\theta \quad (\text{A.5})$$

Since F is arbitrary, set $F=0$ to obtain the radial displacement [37] at the end of the curved beam due to the uniform pressure (\bar{p}) only

$$u_{(\theta_i)} = \frac{\bar{p} L R^4}{E I} \int_0^{\theta_i} (1 - \cos \theta) \sin \theta d\theta \quad (\text{A.6})$$

$$= \frac{\bar{p} L R^4}{2 E I} [(\cos \theta_i - 2) \cos \theta_i + 1]$$

Eq.(A.6) is adequate for a thin beam, i.e. one with a small thickness. For a beam with a large thickness and a rectangular cross-section, replace R in Eq.(A.6) with the neutral

axis of the beam $R_n = \frac{t}{\ln(R_o/R_i)}$,

$$u_{(\theta_i)} = \frac{\bar{p} L R_n^4}{2 E I} [(\cos \theta_i - 2) \cos \theta_i + 1] \quad (\text{A.7})$$

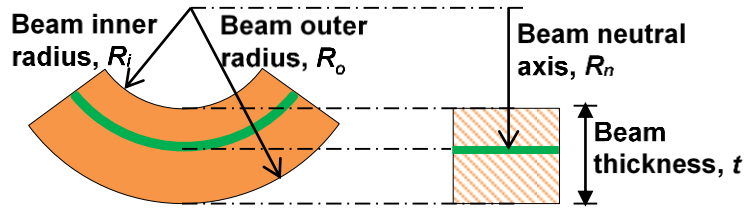


Fig. A. 2 Neutral axis of a curved beam

Recall that a pivoted pad is simplified into a curved beam, see Figure A.1. Thus, the radial deformation at the leading or trailing edge of the pad can be estimated using Eq.(A.7).

Table A.1 lists the geometry and material properties for three pads of differing pad thicknesses. Note that the pad model has no Babbitt layer.

Table A. 1 Pad geometry and material for three pads

Pad thickness	11.3 mm, 18.1 mm, 22.6 mm
Pad radius	59.9 mm
Pivot offset	0.5 and 0.6
Pad width	60 mm
Elastic modulus	207 GPa
Poisson ratio	0.289
Pad full arc length, θ_p	75° ($\theta_i=0.5 \cdot \theta_p=37.5^\circ$) and ($\theta_i=0.4 \cdot \theta_p=30^\circ$)

The deformation at the pad trailing edge can be determined by applying a uniform pressure (1 MPa) on the pad. Table A.2 shows the deformation at the pad trailing edge for the three pads determined using Eq.(A.7) and a finite element (FE) structural computational commercial program. Comparisons in Table A.2(a) indicate that Eq.(A.7) can predict well the deformation at the pad trailing edge for the pad with 0.5 pivot offset.

Note that Eq.(A.7) slightly overestimates the pad deformation for the thin pad by 5%. However, for the pad with 0.6 pivot offset, Eq.(A.7) delivers more accurate results for the thinnest pad but underestimates the pad deformation for a thicker pad.

Table A. 2 Deformation at pad trailing edge due to applied pressure (1 MPa).

(a) Pad offset=0.5				
Pad model number, i	Pad thickness, t_i	Pad trailing edge deformation, u_i		Percentage difference $(u_{i(\text{FE})} - u_{i(\text{Eq.A.7})}) / u_{i(\text{FE})}$
		FE software	Eq.(A.7)	
1	11.3 mm	14.91 μm	15.68 μm	-5.1 %
2	18.1 mm	4.64 μm	4.61 μm	6.5 %
3	22.6 mm	2.87 μm	2.66 μm	7.3 %

(b) Pad offset=0.6				
Pad model number, i	Pad thickness, t_i	Pad trailing edge deformation, u_i		Percentage difference $(u_{i(\text{FE})} - u_{i(\text{Eq.A.7})}) / u_{i(\text{FE})}$
		FE software	Eq.(A.7)	
1	11.3 mm	6.98 μm	6.59 μm	5.4 %
2	18.1 mm	2.34 μm	1.94 μm	17.1 %
3	22.6 mm	1.31 μm	1.12 μm	14.5 %

To include the Babbitt layer deposited on a pad surface, an equivalent elastic modulus of the composite pad with both metal and Babbitt is employed. Gere [39] details the procedure to derive the equivalent elastic modulus of a bimetallic straight beam. Figure A.3 shows a curved beam and two end moments (M_b).

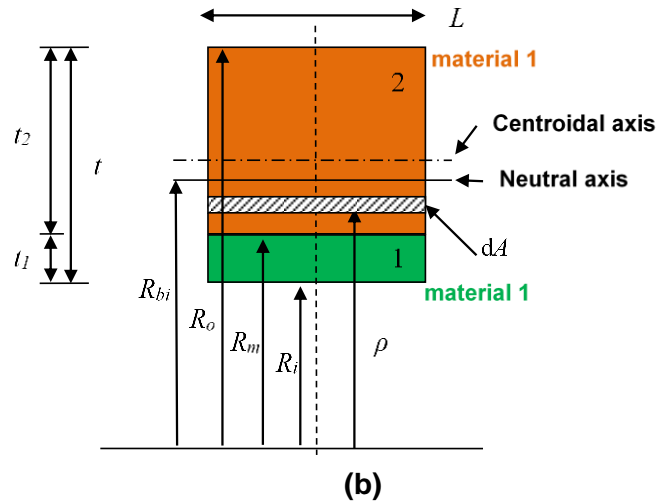
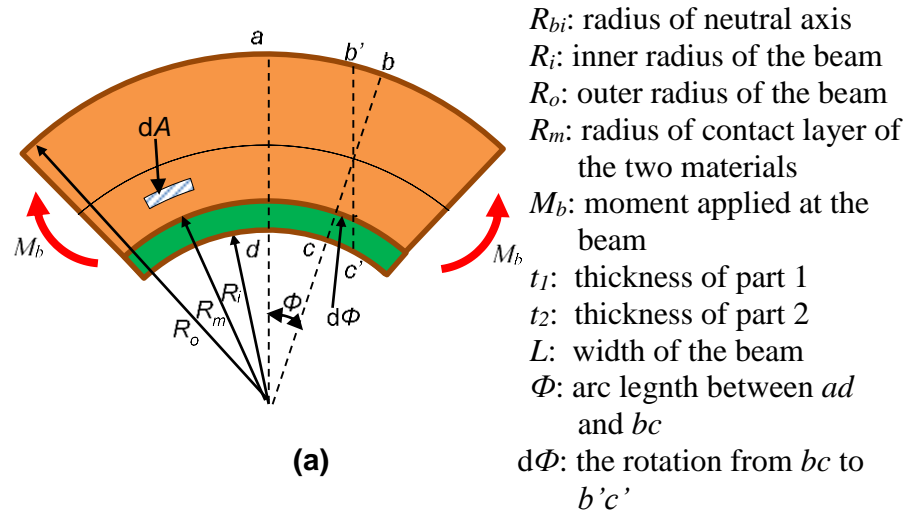


Fig. A. 3 A curved beam made of two materials applied with bending moments (M_b): (a) shape of the curved beam (b) cross-section of the curved beam

Follow the procedure in Ref. [39] and derive the location of the neutral axis (R_{bi}) of a bimetallic curved beam with rectangular cross-section [40],

$$R_{bi} = \frac{E_1 t_1 + E_2 t_2}{E_1 \ln R_m/R_i + E_2 \ln R_o/R_m} \quad (\text{A.9})$$

where E_1 and E_2 are the elastic moduli of material 1 and 2; t_1 and t_2 are the thickness of material 1 and material 2. R_i and R_o denote the inner and outer radius of the beam, and R_m is the radius of the contact layer of the two materials.

Now express the applied moment (M_b) on a bimetallic curved beam as

$$M_b = \frac{d\phi}{\phi} \left[E_1 \left(\frac{R_m - R_i}{2} - R_{bi} \right) A_1 + E_2 \left(\frac{R_o - R_m}{2} - R_{bi} \right) A_2 \right] \quad (\text{A.10})$$

where ϕ is arc length between ad and bc (see Figure A.3(a)) and $d\phi$ is the rotation from bc to $b'c'$. Regarding the bimetallic curved beam as an equivalent curved beam made of single material, Eq.(A.10) becomes

$$M_b = \frac{d\phi}{\phi} \left[E_{eq} \left(\frac{R_o - R_i}{2} - R_{eq} \right) A_1 + A_2 \right] \quad (\text{A.11})$$

where R_{eq} and E_{eq} are the radius of the neutral axis and the elastic modulus of the equivalent beam made of single material; $R_{eq} = \frac{t}{\ln(R_o/R_i)}$.

Comparing Eq. (A.10) and Eq. (A.11) yields an equivalent elastic modulus as

$$E_{eq} = \frac{E_1 \left(\frac{1}{2} t_1 - R_{bi} \right) t_1 + E_2 \left(\frac{1}{2} t_2 - R_{bi} \right) t_2}{\left(\frac{1}{2} t - R_{eq} \right) t} \quad (\text{A.16})$$

The elastic deformation (u) at the trailing edge of a bimetallic beam is

$$u_{(\theta_i)} = \frac{1}{2} \cdot \frac{\bar{p}LR_{eq}^4}{E_{eq}I} \left[(\cos \theta_i - 2) \cos \theta_i + 1 \right] \quad (\text{A.17})$$

Consider the pads having the similar geometry and materials listed in Table A.1 but with a 1.5 mm Babbitt layer on the top surface of the pads.

As a reference, Branagan [26] introduces several equations to calculate the pad elastic deformation due to a bending moment. The one used for predictions in Ref.[26] is

$$u = -\frac{M_b}{AE} (m-1) \frac{4 \left[1 - (m)^2 (1 - 2 \ln(m)) \right]}{\left[(m)^2 - 1 \right]^2 - (2(m) \ln(m))^2} \text{ with } m = \frac{R_o}{R_i} \quad (\text{A.18})$$

where R_o is the pad outer radius and R_i is the pad inner radius. Note that this equation does not account for the Babbitt layer or the pad arc length.

Use the equivalent elastic modulus from Eq. (A.16) and calculate the pad deformation at the trailing edge. Table A.3 shows the deformation at a pad trailing edge predicted using Eq.(A.17), Eq. (A.18), and from a FE commercial software.

Table A. 3 Tip deformation of a pad due to an applied uniform pressure (1 MPa)

Pad model number, i	Pad thickness, t_i (with 1.5 mm Babbitt layer)	Pad trailing edge deformation, u_i		
		FE software	Eq.(A.17)	Eq. (A.18)
1	11.3 mm	19.20 μm	17.18 μm	11.72 μm
2	18.1 mm	4.54 μm	4.86 μm	4.54 μm
3	22.6 mm	2.82 μm	2.76 μm	2.92 μm

The pad trailing edge deformations calculated using Eq.(A.17) and the FE structural model correlate well with each other. Eq. (A.18) from Ref. [26] underestimates the pad trailing edge deformation for the thin pad (Pad #1) by 39%, but predicts well the deformation for the medium thickness pad (Pad #2) and thick pad (Pad #3).

Eq. (A.17) is adequate for general pad cases (any pad thickness t), while Branagan's equation (Eq.(A.18)) is accurate for a pad with large thickness ($t/R > 0.3$).

APPENDIX B-EFFECT OF PAD FLEXIBILITY ON THE FORCE PERFORMANCE
OF THREE-PAD TPJBS (LOP AND LBP CONFIGURATIONS) AND WITH
PRELOAD VARYING FROM 0, 0.25 TO 0.5 [24]

This section presents a parametric study on the effect of pad flexibility on the force performance of a three-pad TPJB. Table B.1 lists the geometry and lubricant properties of the model bearing taken from Ref. [24], i.e., the bearing has a pad clearance of 92.9 μm with thickest pad sets ($t=11.5\text{ mm}$)⁷. Table B. 2 presents the operating conditions and geometrical parameters varied for the model TPJB.

⁷ The bearing with the medium thick pad sets and that with the thick pad sets have the same bearing clearance and pad clearance: $C_B=70\text{ }\mu\text{m}$ and $C_P=93\text{ }\mu\text{m}$. For the bearing with the thin pad sets, $C_B=69\text{ }\mu\text{m}$ and $C_P=92\text{ }\mu\text{m}$.

Table B. 1 Parameters of a TPJB model in Ref. [24].

Number of pads, N_{pad}	3
Configuration	LBP
Rotor diameter, D	101.6 mm
Pad axial length, L	61 mm
Pad arc angle, Θ_P	90°
Pivot offset	50%
Nominal preload, \bar{r}_p	0.25
Cold pad clearance ⁸ , C_P	92.9 μm
Pad mass, m_p	0.54 kg
Pad moment of inertia, I_p	4.86 $\text{kg}\cdot\text{cm}^2$
Pivot stiffness, K_{piv}	751 MN/m
Lubricant type	ISO VG46
Supply lubricant temperature	49 °C
Supply lubricant pressure	2.2 bar
Lubricant density	854 kg/m^3
Lubricant viscosity at 49 °C, μ_0	0.0269 Pa·s
Viscosity temperature coefficient, α	0.0319 1/°C
Lubricant specific heat capacity at 70 °C	1830 J/(kg·K)

Table B. 2 Cases to assess effect of pad flexibility on the performance of a TPJB.

Static specific load, W/LD	689 kPa
Journal speed, Ω	1000 rpm – 12,000 rpm
Pad preload, \bar{r}_p	0, 0.25, 0.5
Load configuration	LBP, LOP
Pad thickness ⁹ , t	Rigid pad, 8.5 mm, 11.5 mm
Pivot stiffness, K_{piv}	750 MN/m

⁸ The bearing clearance varies for the bearing with differing preload, i.e., $\bar{r}_p = 0, 0.25$ and 0.5 .

⁹ The model pad has a 1.5 mm thick Babbitt layer.

The predictive model assumes that the lubricant carries away all the heat generated in the bearing, i.e., adiabatic journal and pad surface. Following the parametric study conducted by San Andrés *et al.* [41], the change in clearance due to an increase in film temperature is not considered, so as to limit the number of factors affecting bearing performance other than pad flexibility.

Define a dimensionless pivot stiffness as ($K_{piv}=750$ MN/m)

$$k_{piv} = \frac{K_{piv} C_p}{W_{\max}} = 16 \quad (\text{B.1})$$

Note that the bearing has a moderately rigid pivot. According to Appendix A and Ref. [41], define a dimensionless pad stiffness as

$$k_{pad} = \frac{C_p}{W / (LD)} K_{pad} = \frac{C_p}{u_t} \cdot \frac{\bar{p}LD}{W} = \frac{E_{eq} I}{R_{eq}^3} \cdot \frac{D}{R_{eq}} \frac{2}{[(\cos \theta_t - 2) \cos \theta_t + 1]} \left(\frac{C_p}{W} \right) \quad (\text{B.2})^{10}$$

with θ_t is the arc length from the pivot to the pad trailing edge. Thus, the dimensionless pad stiffness $k_{pad} = 3.15$ for a pad with a thickness of 8.5 mm, and $k_{pad} = 7.33$ for another pad with a thickness of 11.5 mm, respectively. $k_{pad} = \infty$ denotes a rigid pad.

The dimensionless dynamic force coefficients are defined as¹¹ [42]

$$k_{ij} = \frac{K_{ij} C_p}{W}, c_{ij} = \frac{C_{ij} \Omega C_p}{W}, m_{ij} = \frac{M_{ij} \Omega^2 C_p}{W} \quad i, j = X, Y \quad (\text{B.3})$$

where K , C and M are the bearing stiffness, damping and virtual mass coefficients derived from the complex stiffnesses using a $[K-C-M]$ model. C_p is the cold pad radial clearance, Ω is the rotor speed, and W is the static load applied to the bearing. The Sommerfeld number (S), increasing with shaft speed (Ω) and decreasing with applied load (W), is

¹⁰ In Eq. (C.2), $R_{eq}=54.9$ mm for $k_{pad} = 3.15$ and $R_{eq}=56.4$ mm for $k_{pad} = 7.33$.

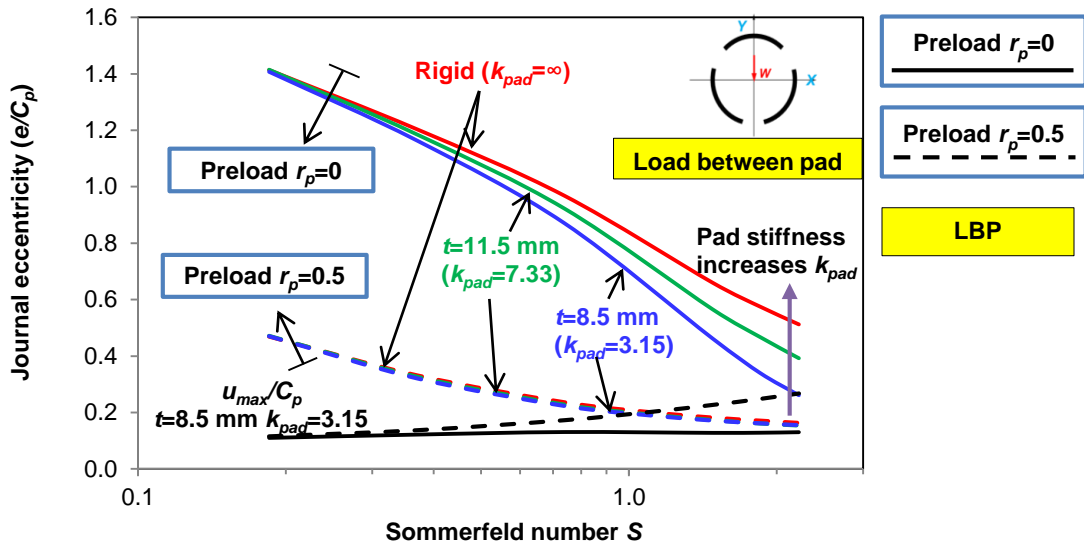
¹¹ $W/C_p=46$ MN/m, $W/(\Omega C_p)=36584 \sim 439006$ N·s/m, and $W/(\Omega^2 C_p)=29 \sim 4192$ kg.

$$S = \frac{\mu_s N L D}{W} \left(\frac{R}{C_p} \right)^2 \quad (\text{B.4})$$

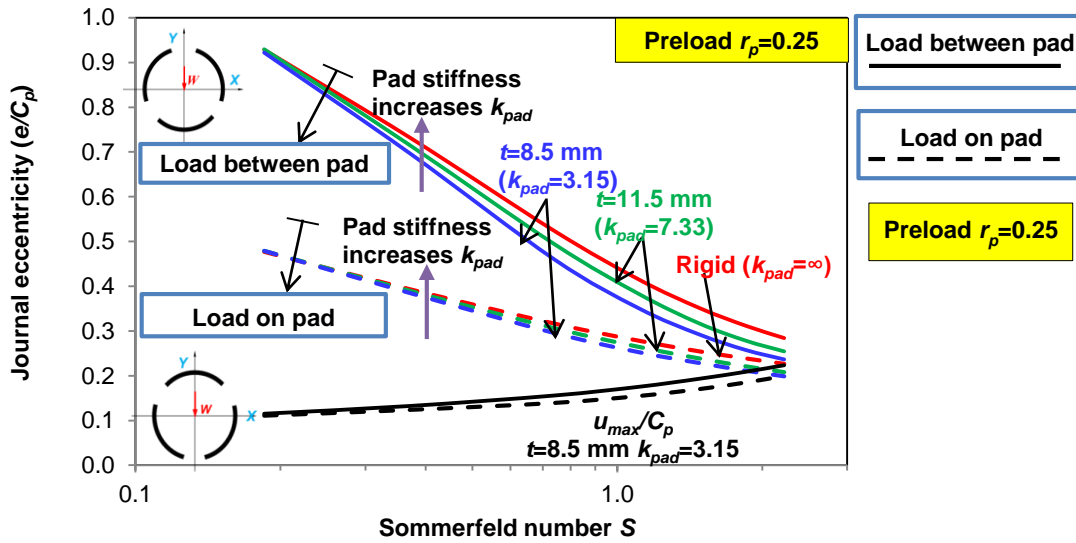
where $N = \Omega/60$ is the shaft rotational speed in revolutions per second, and μ_s is the lubricant viscosity at supply temperature. Since the static load is invariant, $W/(LD)=689$ kPa, S varies from 0.18 to 2.22 as the shaft speed increases from 1,000 rpm to 12,000 rpm.

For the LBP and LOP configurations and three pad preloads, $\bar{r}_p = 0, 0.25, 0.5$, Figure B. 1 depicts the journal eccentricity (e/C_p) and the maximum pad deformation (u_{max}/C_p) for the bearing with thin pads sets versus Sommerfeld number (S). At a large S and as the pad flexibility increases (k_{pad} decreases), the journal eccentricity decreases greatly for the LBP bearing with a null pad preload and the LOP bearing with 0.25 preload, in particular. Contrarily, the maximum pad deformation (u_{max}/C_p) increases with Sommerfeld number (S). For the LBP bearing with 0.5 preload, the maximum pad deformation (u_{max}/C_p) for the bearing with thin pads sets is even greater than the bearing journal eccentricity (e/C_p) at a large S (>1.1), but is still less than the pad clearance ($u_{max}/C_p=0.22$).

Figure B.2 depicts the fluid film thickness and pad deformation at bearing mid-plane for the LBP bearing with 0.5 preload, at $W/(LD)=689$ kPa and rotor speed $\Omega=12,000$ rpm. The minimum film thickness increases with an increase in pad flexibility. As the pad flexibility increases, the location of the minimum film thickness moves from the pad trailing edge towards the pad pivot. This leads to a smaller maximum fluid film temperature (see Figure 14 in Example 1).



(a) LBP, $\bar{r}_p = 0$ & 0.5



(b) LBP & LOP, $\bar{r}_p = 0.25$

Fig. B. 1 Three-pad TPJB journal eccentricity (e/C_p) and maximum pad deformation (u_{max}/C_p) vs. Sommerfeld number (S). Pad stiffness $k_{pad} = 3.15, 7.33, \infty$ (rigid) and pivot stiffness $k_{piv} = 16$. Pad preload: 0, 0.25 and 0.5. LBP and LOP configurations. Specific load $W(LD) = 689$ kPa, rotor speed $\Omega = 500$ rpm to 12,000 rpm[31].

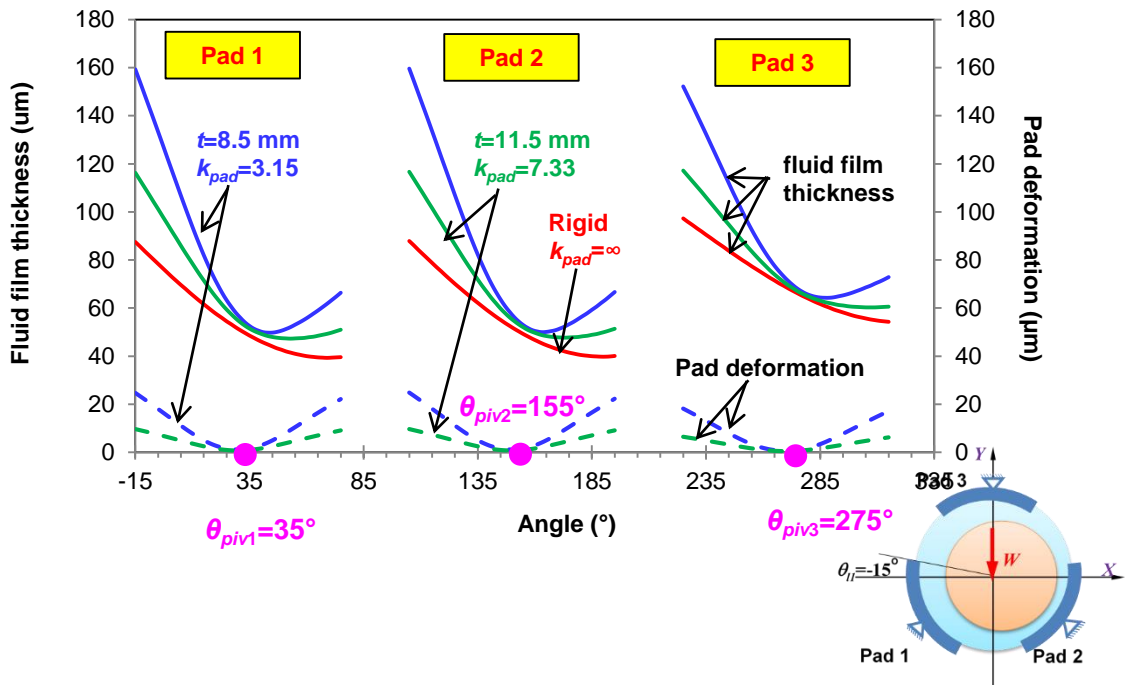


Fig. B. 2 Fluid film thickness and pad deformation at bearing mid-plane. Pad stiffness $k_{pad} = 3.15$ and pivot stiffness $k_{piv} = 16$. Pad preload $\bar{r}_p = 0.5$. LBP configurations. Specific load $W(LD)=689$ kPa, rotor speed $\Omega=12,000$ rpm and Sommerfeld number $S=2.22$.

Figure B.3 shows the pad surface mechanical deformation (u) due to the hydrodynamic fluid film pressure. Similarly, along the circumferential direction, the maximum pad deformation occurs at both the pad leading edge and the pad trailing edge (pivot offset=50%); while along the axial direction, the maximum pad deformation is at the pad mid-plane ($Z=0$). For the LBP bearings, as the pad preload increases from 0, to 0.25, to 0.5, the pad deformation increases since the fluid film pressure on the pad increases.

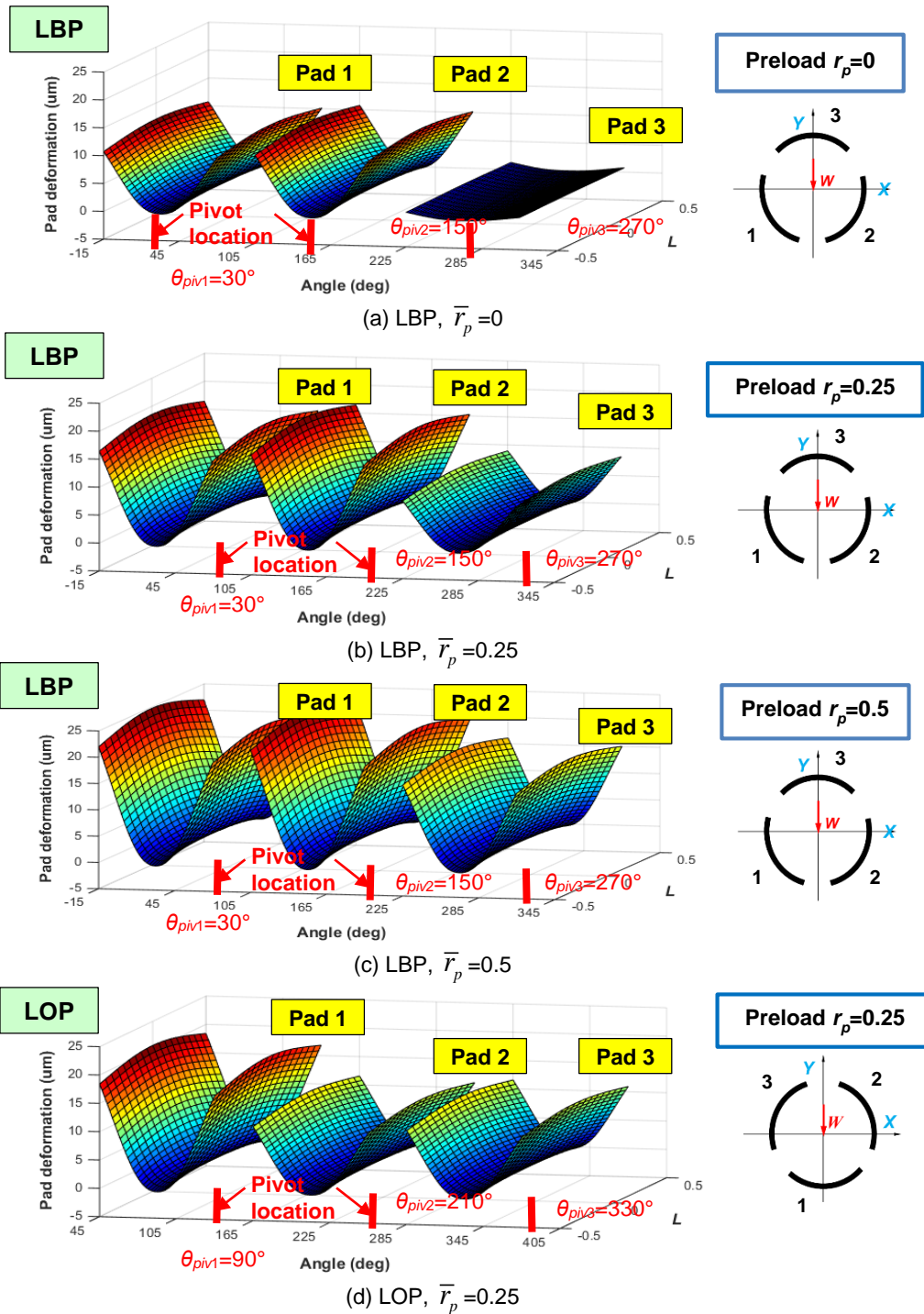


Fig. B. 3 Pad surface radial deformation. Pad stiffness $k_{pad} = 3.15$ and pivot stiffness $k_{piv} = 16$. Pad preload $\bar{r}_p = 0, 0.25$ and 0.5 . LOP and LBP configurations. Specific load $W/(LD) = 689$ kPa, rotor speed $\Omega = 12,000$ rpm ($S = 2.22$).

Figure B.4 depicts the drag friction coefficient $f = T_{orque} / (R_J W)$ increasing proportionally with S for both the LBP and LOP configurations. The bearing with the largest preload has more viscous drag. Pad flexibility has no effect on the drag friction (f), hence has no influence on the bearing drag power losses.

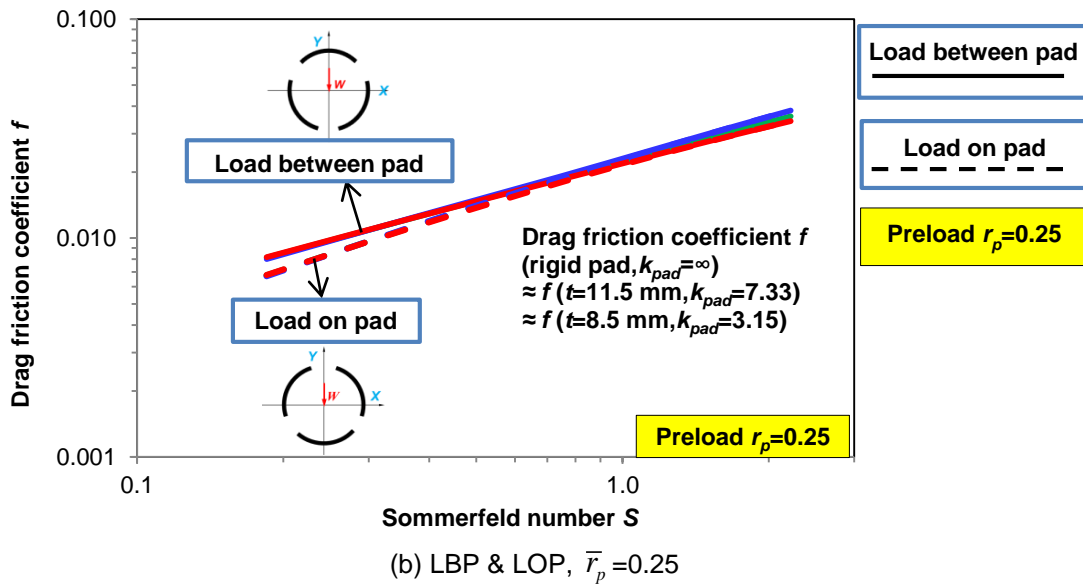
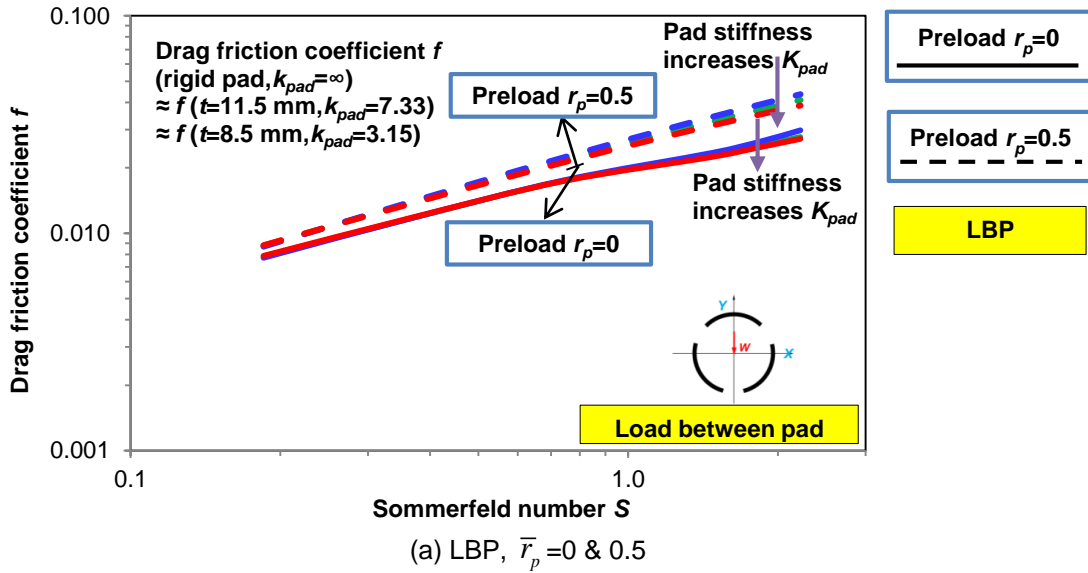


Fig. B. 4 Three-pad TPJB drag friction coefficient (f) vs. Sommerfeld number (S). Pad stiffness $k_{pad} = 3.15, 7.33, \infty$ (rigid) and pivot stiffness $k_{piv} = 16$. Pad preload: 0, 0.25 and 0.5. LBP and LOP configurations. Specific load $W/(LD)=689$ kPa, rotor speed $\Omega=500$ rpm to 12,000 rpm.

Figure B.5 to B.10 depict the (dimensionless) bearing force coefficients, k , c and m versus Sommerfeld number. The frequency range to obtain the force coefficients is up to twice the synchronous shaft speed: $0 \sim 2\Omega$ [43].

Figure B.5 depicts the dimensionless direct stiffnesses (k_{XX} , k_{YY}) for the LBP bearings with preload $\bar{r}_p = 0$ and 0.5, while Figure B.6 shows k_{XX} and k_{YY} for the LBP and LOP bearing with a 25% pad preload. Pad flexibility increases both k_{XX} and k_{YY} at a large Sommerfeld number ($S > 0.8$). For the LOP bearing, pad flexibility increases k_{XX} by up to 30% at $S = 2.22$. Recall that Fig. 15 in Example 1 depicts an increase in bearing stiffnesses due to pad flexibility at a smaller unit load. For the LOP TPJB, the stiffness along the unloaded direction (k_{XX}) is one order of magnitude lesser than the stiffness along the load direction (k_{YY}) at a Sommerfeld number less than 1 ($S < 1$).

For the LBP TPJB with a 50% pad preload and the LOP TPJB with a 25% pad preload, k_{XX} and k_{YY} increase with S . For the LBP TPJB with null preload, k_{XX} and k_{YY} decrease with an increase in S .

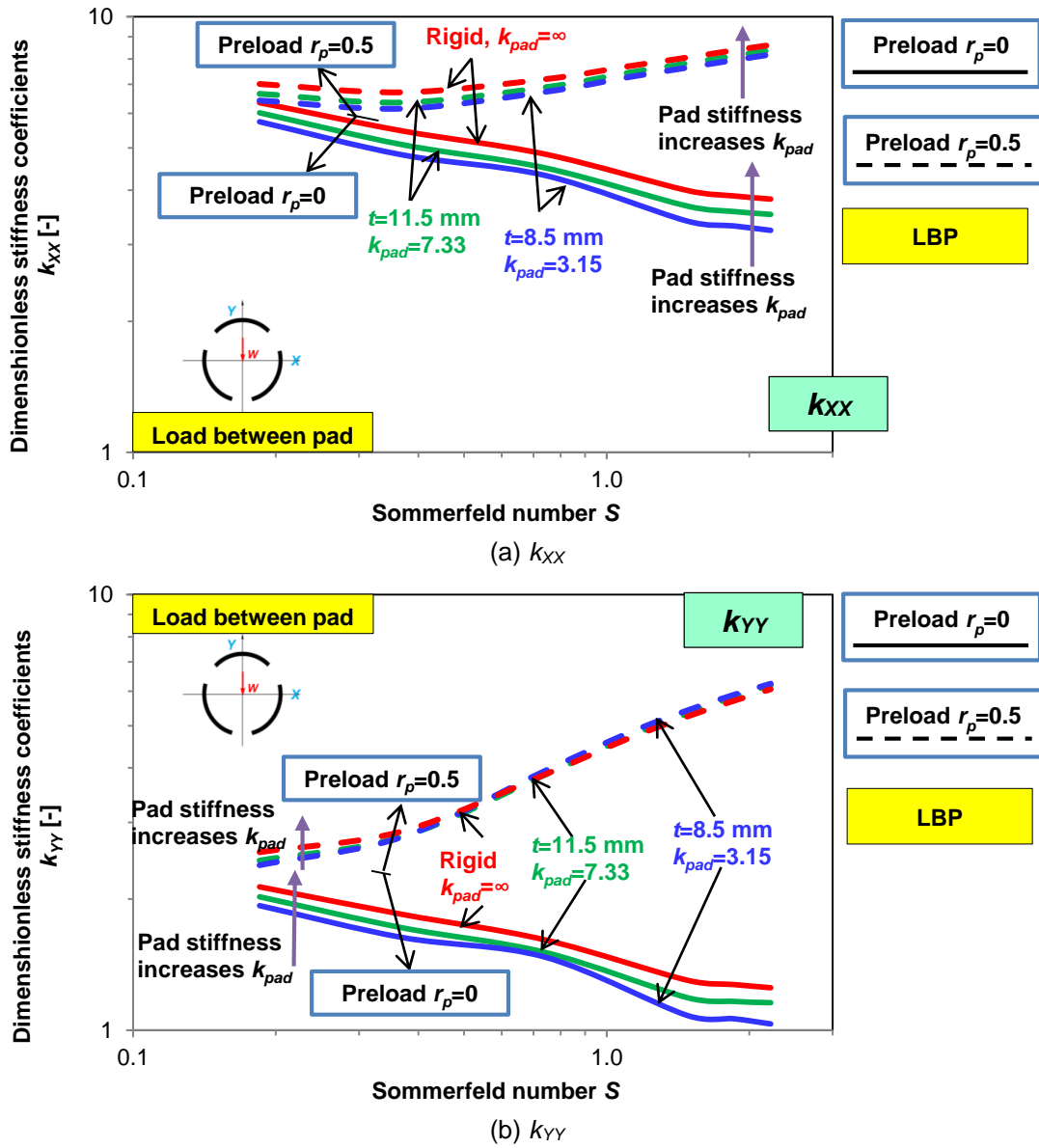


Fig. B. 5 Three-pad TPJB stiffness coefficients (k_{xx} , k_{yy}) vs. Sommerfeld number (S). Pad stiffness $k_{pad} = 3.15, 7.33, \infty$ (rigid) and pivot stiffness $k_{piv} = 16$. Pad preload $\bar{r}_p = 0, 0.5$. LBP configuration. Specific load $W/(LD)=689$ kPa, rotor speed $\Omega=500$ rpm to 12,000 rpm [31].

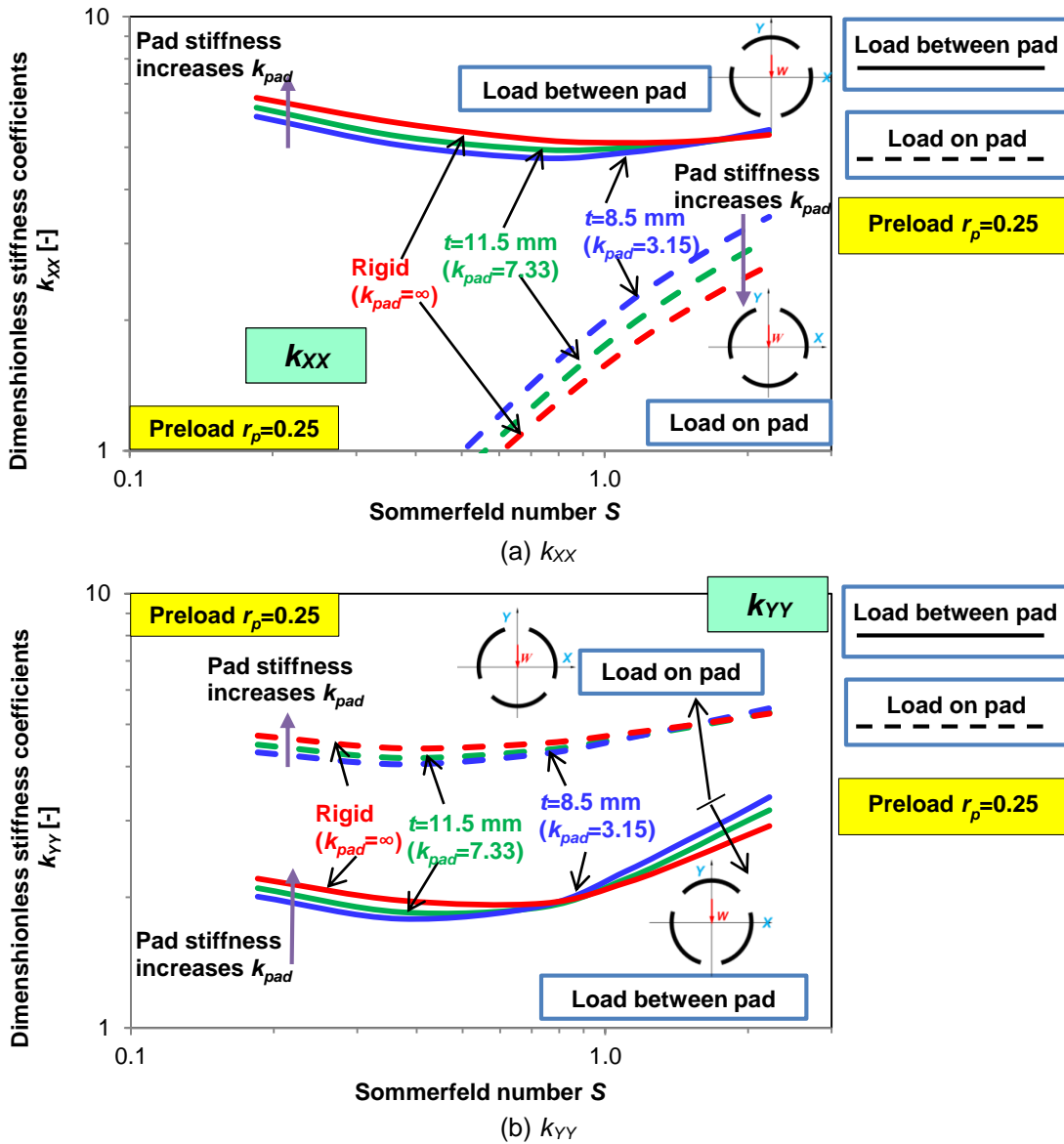
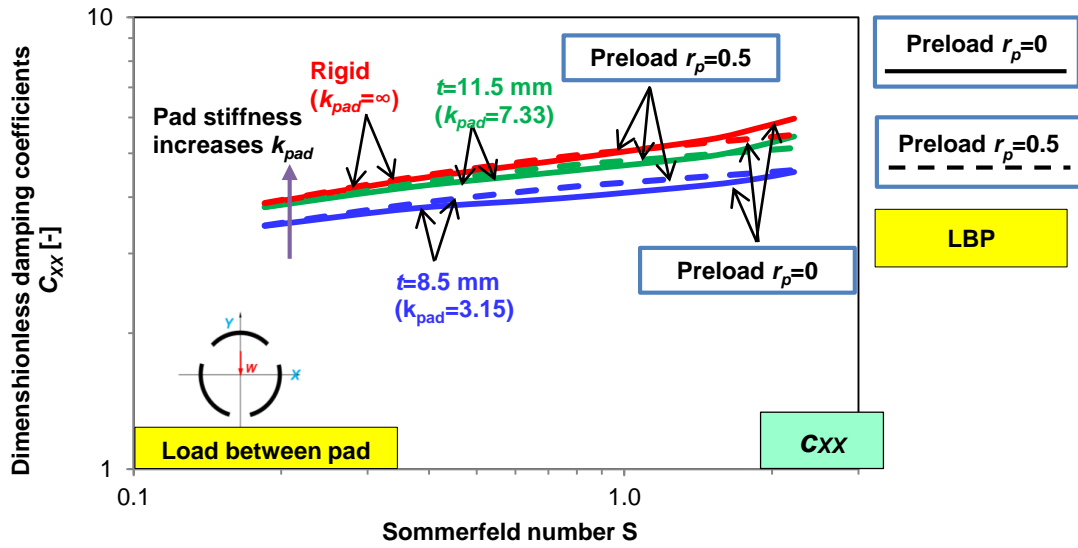


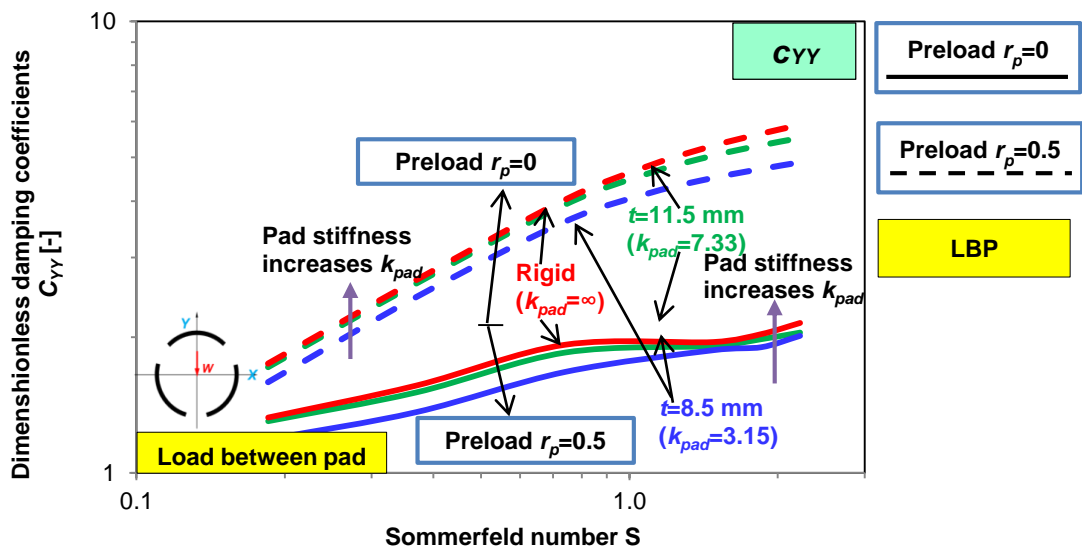
Fig. B. 6 Three-pad TPJB stiffness coefficients (k_{xx} , k_{yy}) vs. Sommerfeld number (S). Pad stiffness $k_{pad} = 3.15, 7.33, \infty$ (rigid) and pivot stiffness $k_{piv} = 16$. Pad preload $\bar{r}_p = 0.25$. LBP and LOP configurations. Specific load $W(LD) = 689$ kPa, rotor speed $\Omega = 500$ rpm to 12,000 rpm [31].

Figure B.7 depicts the direct damping coefficients (c_{XX} , c_{YY}) versus Sommerfeld number (S) for LBP bearings with pad preload $\bar{r}_p = 0$ and 0.5. Figure B.8 shows c_{XX} and c_{YY} for both LBP and LOP bearings with a 25% pad preload. The damping (c_{XX} , c_{YY}) coefficients increase with S ; however, for the LBP TPJB with null preload, c_{YY} decreases for $0.74 < S < 1.48$. As pad flexibility increases, the damping coefficients decrease dramatically by up to 24%, in particular for large Sommerfeld number ($S > 1.0$). Pad flexibility has a more pronounced effect on c_{XX} of a LBP TPJB with null pad preload ($\bar{r}_p = 0$).

Figure B.9 depicts the virtual mass coefficients (m_{YY} , m_{YY}) versus Sommerfeld number (S) for the LBP bearings with preload $\bar{r}_p = 0$ and 0.5, and Figure B.10 shows the mass coefficients (m_{YY} , m_{YY}) for the LBP and LOP bearings with a 25% pad preload. In general m_{YY} , $m_{YY} < 0$ denote the bearing stiffens as the excitation frequency increases. Pad flexibility has a more pronounced effect on m_{YY} , in particular for the LBP bearing with preload equal to either 0 or 0.25. Though the coefficients (m) do not approach zero as S increases, the physical virtual mass coefficients (M_{YY} , M_{YY}) approach to zero at a large S , thus indicating the dynamic stiffness $\text{Re}(Z_{YY})$ is frequency independent.



(a) c_{XX}



(b) c_{YY}

Fig. B. 7 Three-pad TPJB damping coefficients (c_{XX} , c_{YY}) vs. Sommerfeld number (S). Pad stiffness $k_{pad} = 3.15, 7.33, \infty$ (rigid) and pivot stiffness $k_{div} = 16$. Pad preload $\bar{r}_p = 0, 0.5$. LBP configuration. Specific load $W/(LD)=689$ kPa, rotor speed $\Omega=500$ rpm to 12,000 rpm [31].

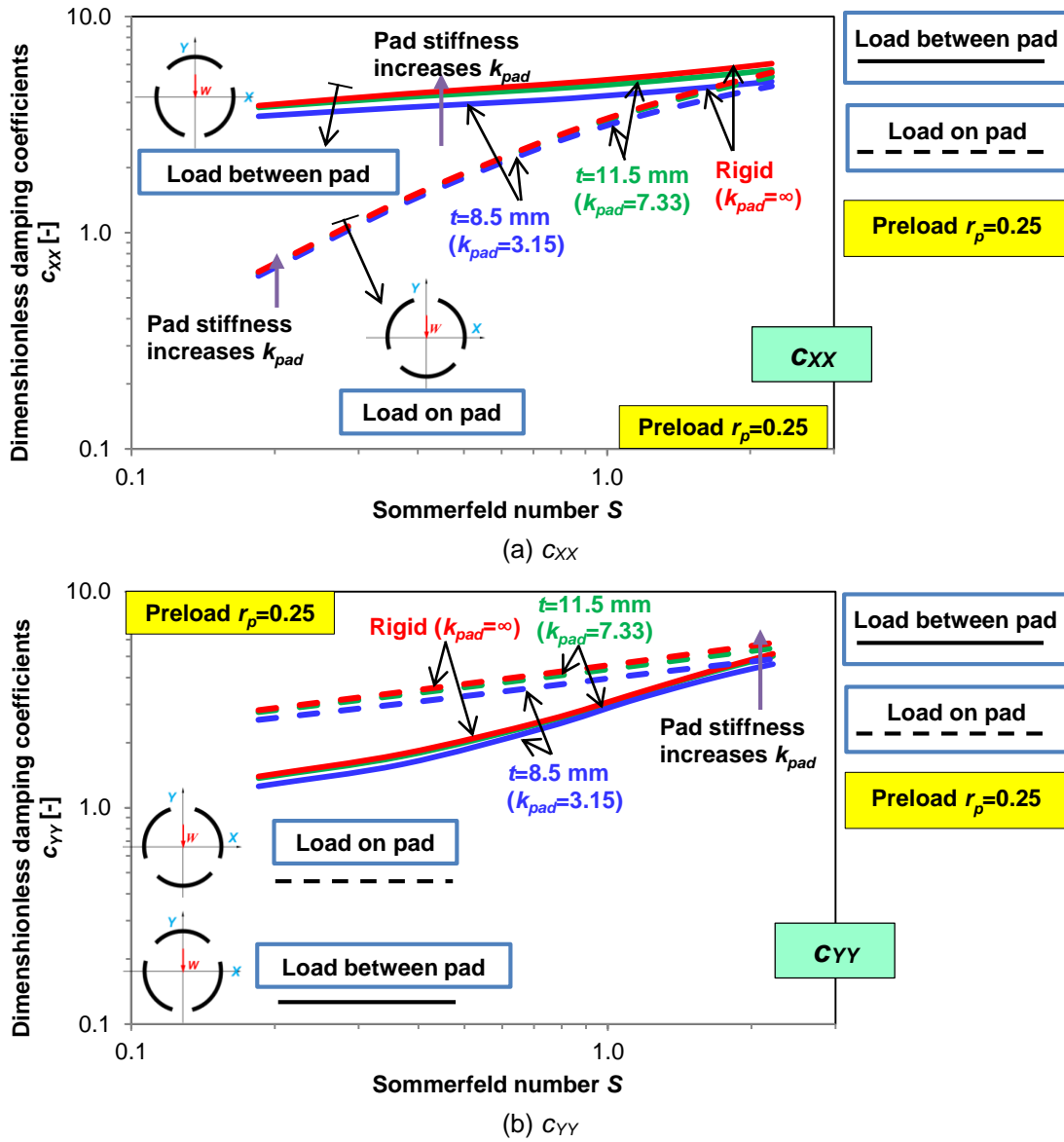
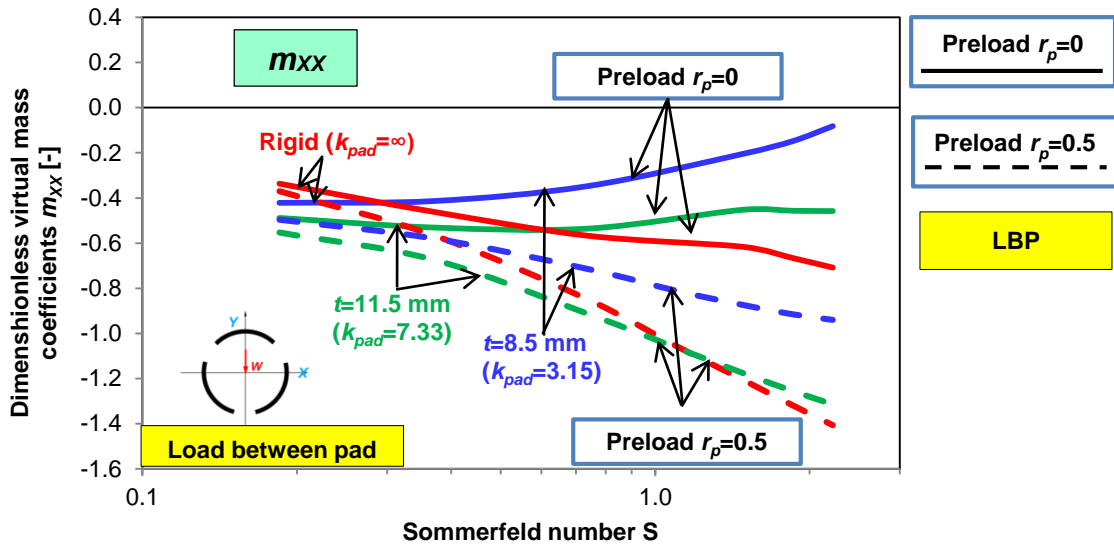
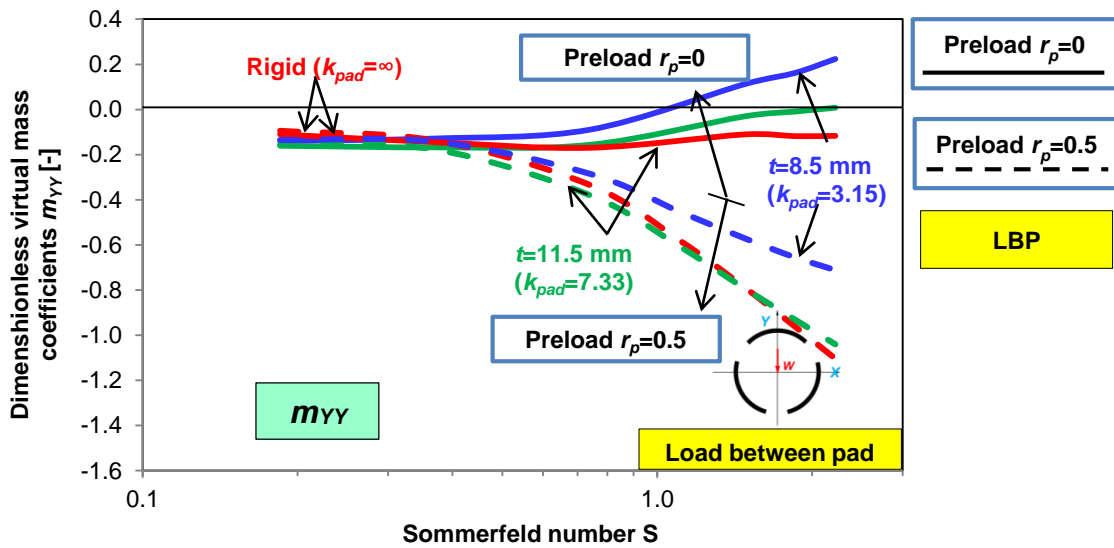


Fig. B. 8 Three-pad TPJB damping coefficients (c_{XX} , c_{YY}) vs. Sommerfeld number (S). Pad stiffness $k_{pad} = 3.15, 7.33, \infty$ (rigid) and pivot stiffness $k_{piv} = 16$. Pad preload $\bar{r}_p = 0.25$. LBP and LOP configurations. Specific load $W(LD) = 689$ kPa, rotor speed $\Omega = 500$ rpm to 12,000 rpm [31].

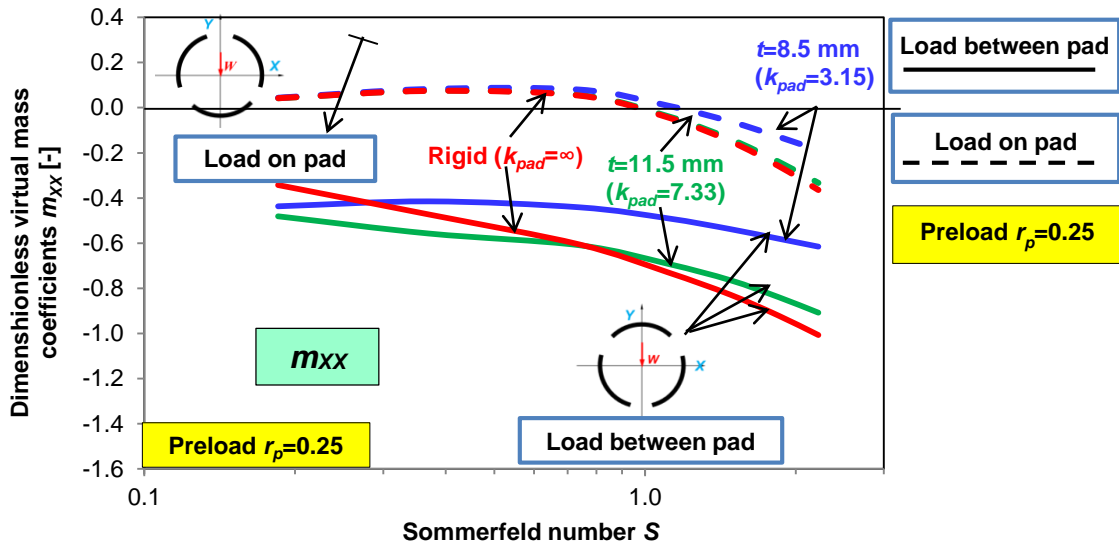


(a) m_{xx}

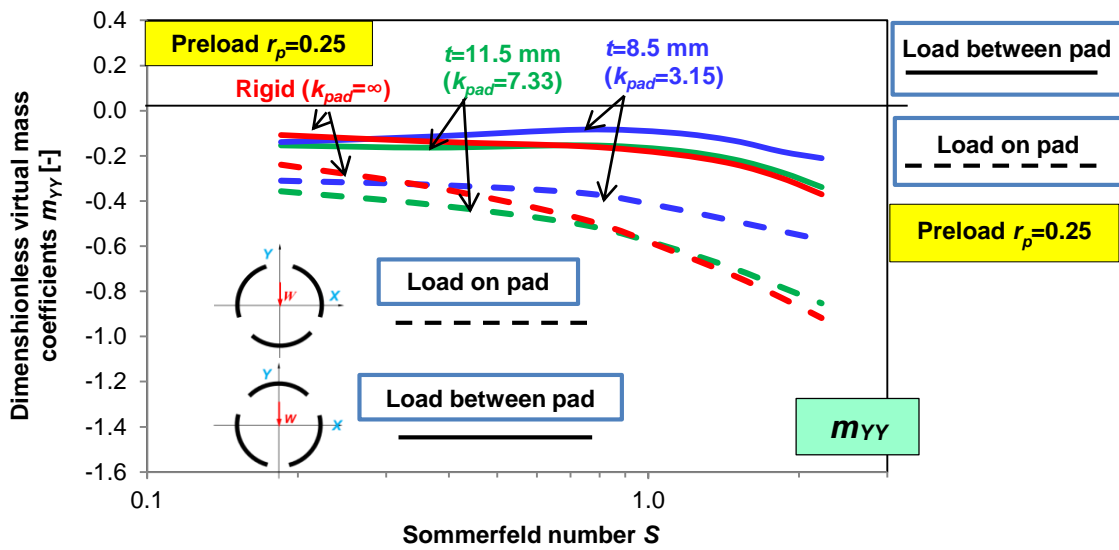


(b) m_{yy}

Fig. B. 9 Three-pad TPJB virtual mass coefficients (m_{xx} , m_{yy}) vs. Sommerfeld number (S). Pad stiffness $k_{pad} = 3.15, 7.33, \infty$ (rigid) and pivot stiffness $k_{piv} = 16$. Pad preload $\bar{r}_p = 0$ and 0.5 . LBP configuration. Specific load $W/(LD)=689$ kPa, rotor speed $\Omega=500$ rpm to $12,000$ rpm [31].



(a) m_{xx}



(b) m_{yy}

Fig. B. 10 Three-pad TPJB virtual mass coefficients (m_{xx} , m_{yy}) vs. Sommerfeld number (S). Pad stiffness $k_{pad} = 3.15, 7.33, \infty$ (rigid) and pivot stiffness $k_{piv} = 16$. Pad preload $\bar{r}_p = 0.25$. LBP and LOP configurations. Specific load $W(LD)=689$ kPa, rotor speed $\Omega=500$ rpm to 12,000 rpm [31].

Closure Pad flexibility shows a more pronounced effect on the journal eccentricity and the force coefficients of a TPJB with null pad preload than for the bearings with a physical pad preloads (0.25 and 0.5), in particular for operation with a small load or at a high surface speed ($S > 0.8$).

The bearing journal eccentricity decreases with the Sommerfeld number S . At a large $S > 0.8$, pad flexibility decreases greatly the bearing journal eccentricity for the LBP bearing with a null pad preload and the LOP bearing with 0.25 preload, in particular. Pad flexibility has no effect on the bearing viscous drag friction coefficient.

For the LOP and LBP bearings with a 25% pad preload, pad flexibility increases the stiffness coefficients (k_{XX} , k_{YY}) at large Sommerfeld number ($S > 0.8$). For the LBP bearing with null pad preload, pad flexibility reduces (k_{XX} , k_{YY}) by up to 17%.

As the pad flexibility increases, the damping coefficients (c_{XX} , c_{YY}) reduces at large Sommerfeld number ($S > 1.0$), in particular for the LBP bearing with null preload. Pad flexibility drops the damping coefficients by up to 24%.

APPENDIX C-EFFECT OF PAD FLEXIBILITY ON THE FORCE PERFORMANCE
OF FOUR-PAD TPJBS WITH TWO LOAD CONFIGURATIONS (LBP AND LOP)

[26]

This section presents a parametric study on the effect of pad flexibility on the forced performance of a four-pad TPJB presented in Ref. [26]. Table C.1 lists the bearing geometry and operating conditions.

Table C. 1 Parameters of the four-pad TPJB presented in Ref. [26]

Number of pads, N_{pad}	4
Configuration	LBP & LOP
Rotor diameter, D	120 mm
Pad axial length, L	60 mm
Pad arc angle, Θ_P	75°
Pivot offset	60%
Dimensionless preload, \bar{r}_p	0, 0.25
Bearing cold clearance, C_B	81.5 μm
Pad cold clearance, C_P	81.5 μm
Pad mass, m_P	0.98 kg
Pad moment of inertia, I_P	0.16 $\text{kg}\cdot\text{m}^2$
Pad material	Young's modulus, E Poisson's ratio, ν
	207 GPa 0.289
Pivot type	Spherical pivot
Supply oil pressure	1 bar
Inlet oil temperature	33.5 °C
Lubricant density	854 kg/m^3
Lubricant viscosity at 33.5 °C, μ_0	52.1 $\text{mPa}\cdot\text{s}$
Viscosity temperature coefficient, α	0.0342 $1/^\circ\text{C}$
Lubricant specific heat capacity at 70	1970 $\text{J}/(\text{kg}\cdot\text{K})$

Recall that the TPJB in Ref. [26] has stiff pads with a moderate stiff pivot ($K_{piv}=870$ MN/m). In this appendix, the pad thickness varies to change the pad flexibility. Table C. 2 lists the operating conditions and geometrical parameters for the TPJB model. As is discussed in Appendix B, pad flexibility shows a more pronounced effect on a TPJB with null preload. Thus, the following parametric study analyzes a TPJB with a null preload $\bar{r}_p=0$ operating at either LBP or LOP configurations.

Table C. 2 Cases to assess effect of pad flexibility on the performance of a TPJB.

Static specific load, $W/(LD)$	1,435 kPa
Journal speed, Ω	500 rpm – 6,000 rpm
Sommerfeld number ¹² , S	0.19 – 2.27
Pad preload, \bar{r}_p	0
Load configuration	LOP & LBP
Pad thickness, t	Rigid pad, 22.6 mm, 11.3 mm
Pivot stiffness, K_{piv}	870 MN/m

Define a dimensionless pivot stiffness as,

$$k_{piv} = \frac{K_{piv} C_p}{W} = 8.0 \quad (C.1)$$

where $K_{piv}=870$ MN/m is the dimensional pivot stiffness, $C_p=81.5$ μm is the cold pad clearance and $W=8,896$ N is the applied static load. According to Appendix A, define a dimensionless pad stiffness as

$$k_{pad} = \frac{C_p}{W / (LD)} K_{pad} = \frac{C_p}{u_t} \cdot \frac{\bar{p}LD}{W} = \frac{E_{eq} I}{R_{eq}^3} \cdot \frac{D}{R_{eq}} \frac{2}{[(\cos \theta_t - 2) \cos \theta_t + 1]} \left(\frac{C_p}{W} \right) \quad (C.2)^{13}$$

with $\theta_t=30^\circ$ is the arc length from the pivot to the pad trailing edge. Thus, the dimensionless pad stiffnesses are $k_{pad} = 4.1$ for a pad with a thickness of 11.3 mm, $k_{pad} = 24.4$ for another pad with a thickness of 22.6 mm¹⁴. $k_{pad} = \infty$ denotes a rigid pad.

Current predictions assume that the lubricant carries away all the heat generated in the bearing, i.e., adiabatic journal and pad surface. The lubricant inlet thermal mixing coefficient (λ) is assumed to be $\lambda=0.8$ in the prediction. Following the parametric study conducted by San Andrés *et al.* [42], the change in clearance due to an increase in film

¹² Since the static load is constant, $W/(LD)=1,435$ kPa, S varies from 0.19 to 2.27 as the shaft speed increases from 500 rpm to 6,000 rpm.

¹³ In Eq. (C.2), $R_{eq}=65.4$ mm for $k_{pad} = 4.1$ and $R_{eq}=70.6$ mm for $k_{pad} = 24.4$.

¹⁴The pad FE model does not include a Babbitt layer.

temperature is not considered, so as to limit the number of factors affecting bearing performance other than pad flexibility.

Figure C.1 depicts the journal eccentricity (e/C_p) and peak pad surface deformation (u_{max}/C_p) versus Sommerfeld number (S) for the TPJB under LBP and LOP configurations with null pad preload. The effect of pad flexibility on the journal eccentricity is not significant. At low Sommerfeld number ($S < 0.3$), pad flexibility slightly increases the journal eccentricity. The maximum pad deformation (u_{max}/C_p) for the LOP bearing is larger than that of the LBP bearing. At the largest S , the maximum pad deformation is 36% of the cold pad clearance.

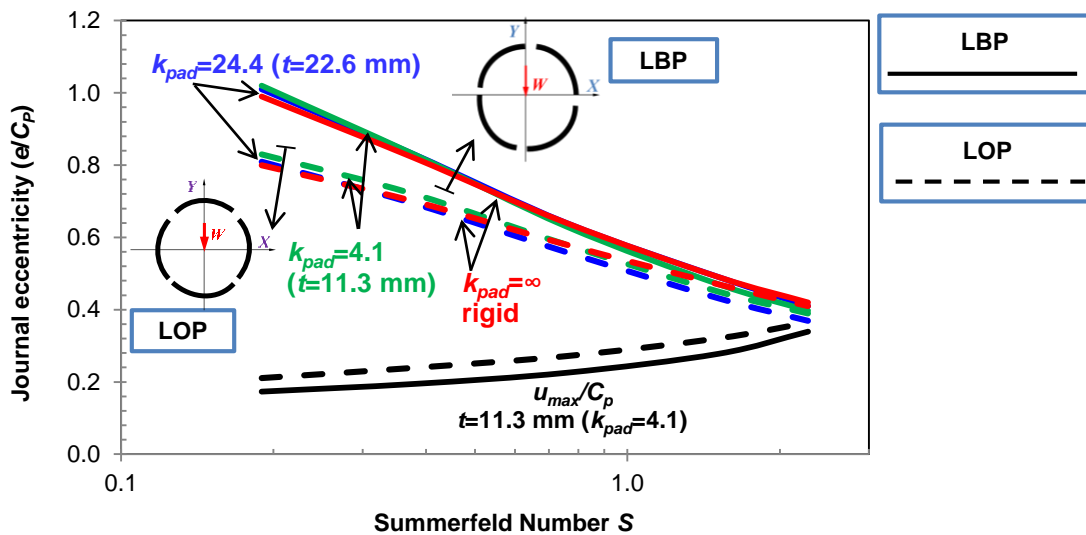


Fig. C. 1 Four-pad TPJB journal eccentricity (e/C_p) vs. Sommerfeld number (S). Pad stiffness $k_{pad} = 4.1, 24.4, \infty$ (rigid) and pivot stiffness $k_{piv} = 8.0$. Pad preload $\bar{r}_p = 0$. LBP and LOP configurations. Specific load $W/(LD) = 1,239$ kPa, rotor speed $\Omega = 500$ rpm to 6,000 rpm.

Figure C.2 shows the pad surface mechanical deformation (u) due to the hydrodynamic fluid film pressure for the TPJB with the most flexible pads ($k_{pad} = 4.1$). The maximum pad deformation locates at the pad mid-plane ($Z=0$) and the pad leading edge. Pad #1 for the LOP bearing is the most loaded pad and has the largest deformation at its leading edge. For the LBP bearing, due to geometric symmetry, the loaded two pads (#1 and 2) have the same pad deformation while the upper two pads (#3 and 4) have the same pad deformation as well.

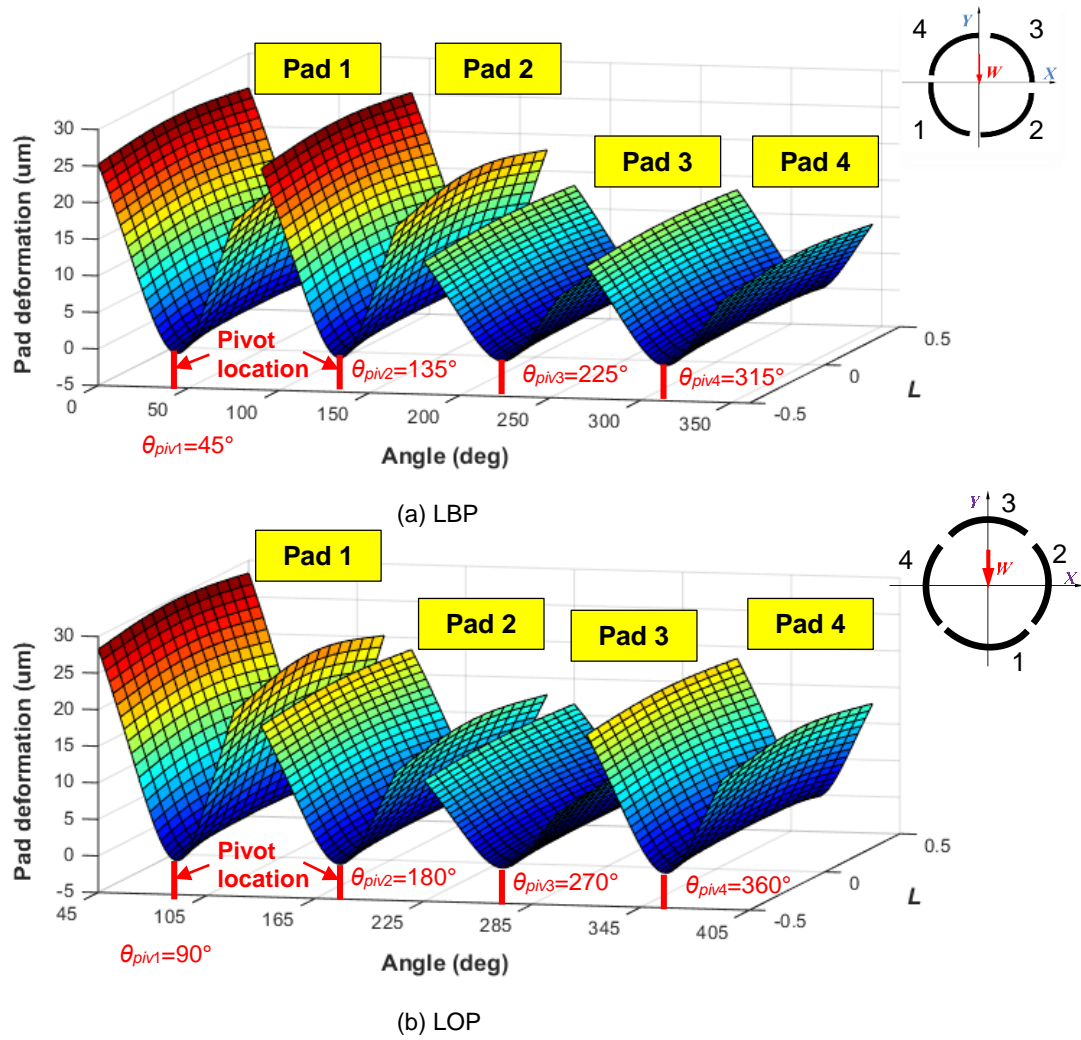


Fig. C. 2 Pad surface radial deformation. Pad stiffness $k_{pad} = 4.1$ and pivot stiffness $k_{piv} = 8.0$. Pad preload $\bar{F}_p = 0$. LOP and LBP configurations. Specific load $W/(LD) = 1,239$ kPa, rotor speed $\Omega = 6,000$ rpm ($S = 2.22$).

Figure C.3 shows the drag friction coefficients $f = T_{orque}/(R_j W)$ increasing with S . The load configuration difference and pad flexibility show no effect on the bearing drag friction coefficients, since the bearing drag torque (T_{orque}) varies little for all cases listed in Table C.2.

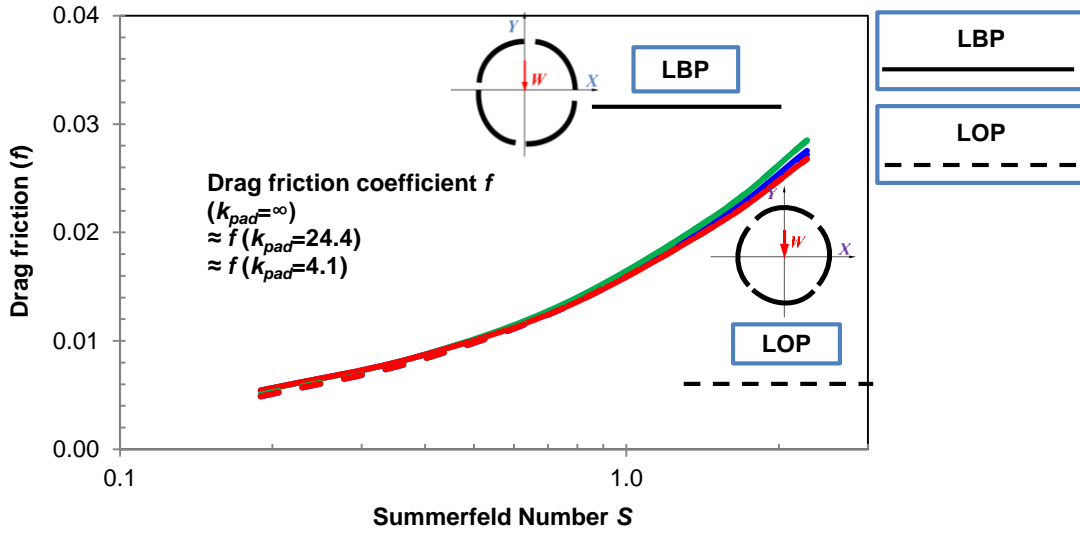


Fig. C. 3 Four-pad TPJB drag friction coefficient (f) vs. Sommerfeld number (S). Pad stiffness $k_{pad} = 4.1, 24.4, \infty$ (rigid) and $k_{piv} = 8.0$. Pad preload $\bar{r}_p = 0$. LBP and LOP configurations. Specific load $W/(LD)=1,239$ kPa, rotor speed $\Omega=500$ rpm to 6,000 rpm.

The dimensionless dynamic force coefficients are defined as¹⁵ [43]

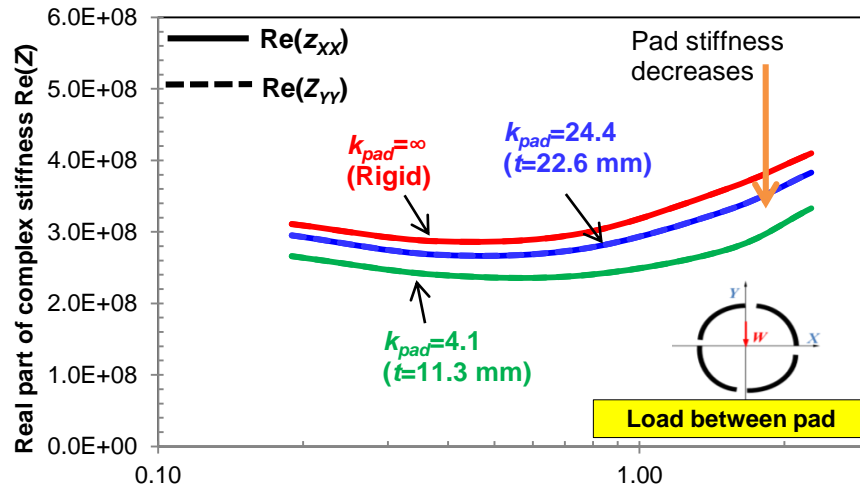
$$k_{ij} = \frac{K_{ij} C_p}{W}, c_{ij} = \frac{C_{ij} \Omega C_p}{W}, m_{ij} = \frac{M_{ij} \Omega^2 C_p}{W} \quad i, j = X, Y \quad (C.3)$$

where K , C and M are the bearing stiffness, damping and virtual mass coefficients derived from the complex stiffnesses using a $[K-C-M]$ model. C_p is the cold pad radial clearance, Ω is the rotor speed, and W is the static load applied to the bearing. The frequency range to obtain the force coefficients is up to twice the synchronous speed: $\omega=0 \sim \Omega$.

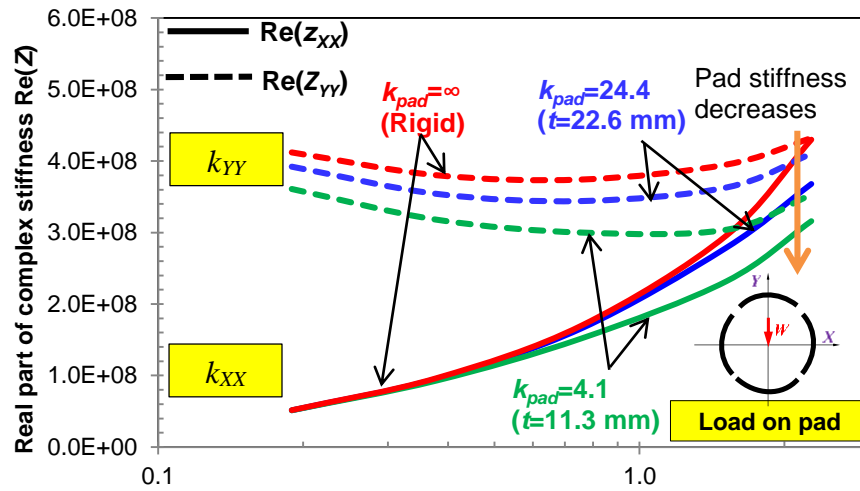
Figure C.4 depicts the real part of the complex stiffnesses, $\text{Re}(Z)=K-\omega^2 M$, reduced at synchronous speed ($\omega=\Omega$). Pad flexibility reduces $\text{Re}(Z)$, in particular for the LOP bearing.

¹⁵ $W/C_p=109$ MN/m, $W/(\Omega C_p)=173723 \sim 2084676$ N·s/m, and $W/(\Omega^2 C_p)=276 \sim 39814$ kg.

Figure C.5 shows the stiffness coefficients (k) of the TPJB versus Sommerfeld number (S). Pad flexibility reduces the bearing stiffnesses. Note that $k_{XX}=k_{YY}$ for the four-pad TPJB under a LBP configuration due to geometry symmetric. For the LBP bearing, pad flexibility reduces k by up to 12%. For the LOP bearing, pad flexibility shows a more pronounced effect on the stiffnesses along the load direction (k_{YY}). k_{YY} for the TPJB with rigid pad ($k_{pad} = \infty$) is up to 14% smaller than that for the TPJB with the most flexible pads ($k_{pad} = 4.1$). Pad flexibility increases slightly k_{XX} by 5% at the largest S . At a low Sommerfeld number ($S < 1$), k_{XX} is greatly less than k_{YY} .

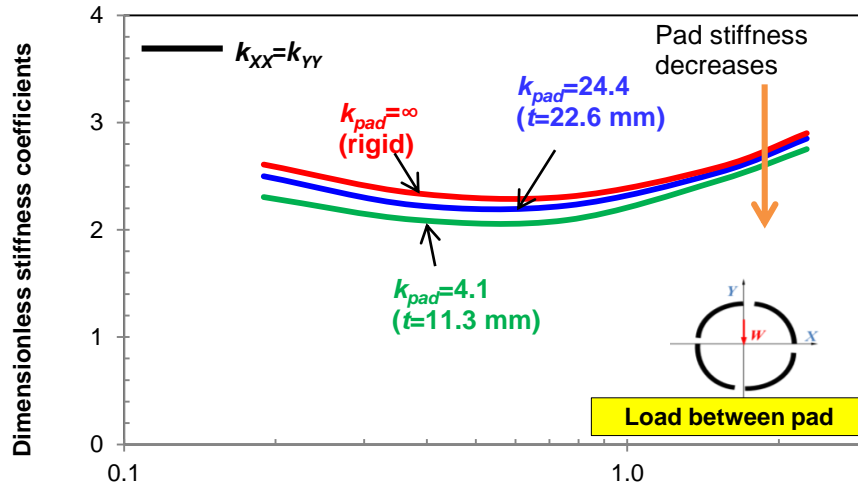


(a) LBP



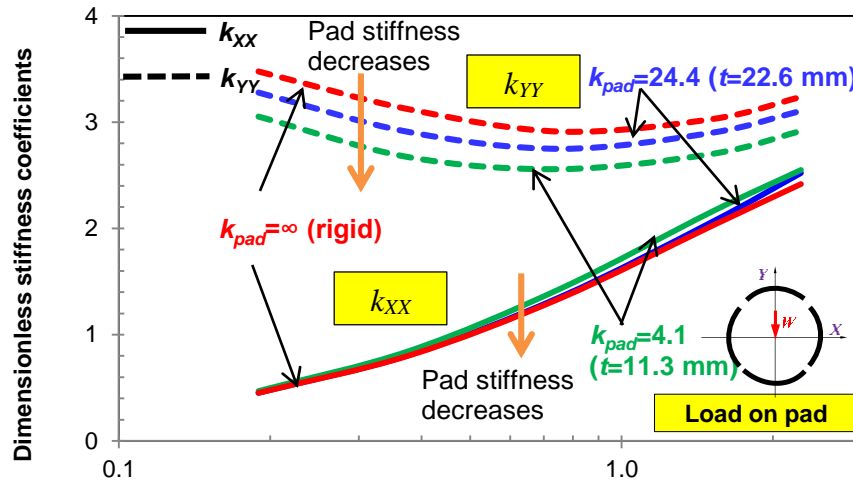
(b) LOP

Fig. C. 4 Four-pad TPJB dimensionless stiffnesses (k_{XX} and k_{YY}) vs. Sommerfeld number (S). Pad stiffness $k_{pad} = 4.1, 24.4, \infty$ (rigid) and pivot stiffness $k_{piv} = 8.0$. Pad preload $\bar{r}_p = 0$. LBP and LOP configurations. Specific load $W/(LD) = 1,239$ kPa, rotor speed $\Omega = 500$ rpm to 6,000 rpm.



Dimensionless stiffness coefficients

(a) LBP



Dimensionless stiffness coefficients

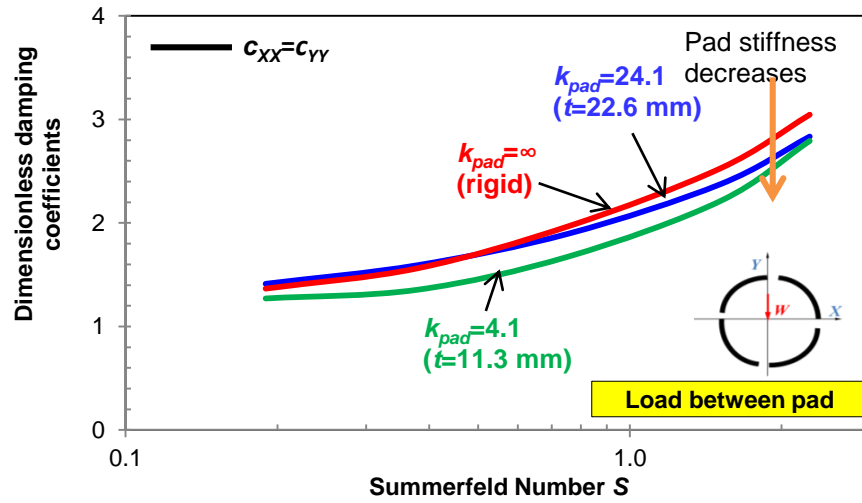
(b) LOP

Fig. C. 5 Four-pad TPJB dimensionless stiffnesses (k_{xx} and k_{yy}) vs. Sommerfeld number (S). Pad stiffness $k_{pad} = 4.1, 24.4, \infty$ (rigid) and pivot stiffness $k_{piv} = 8.0$. Pad preload $\bar{r}_p = 0$. LBP and LOP configurations. Specific load $W/(LD) = 1,239$ kPa, rotor speed $\Omega = 500$ rpm to 6,000 rpm.

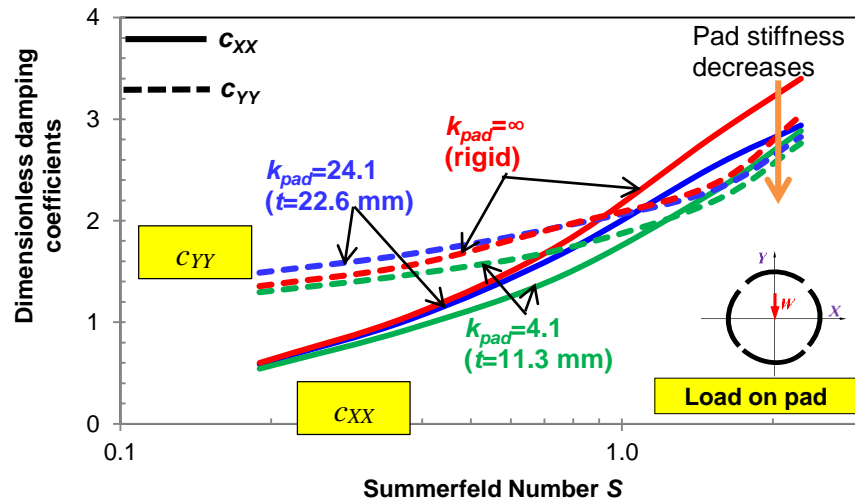
Figure C.6 shows the dimensionless damping coefficients (c) of the TPJB versus Sommerfeld number (S). Pad flexibility has a more pronounced effect on c_{xx} for the LOP bearing. At the largest Sommerfeld number, c_{xx} for the LOP bearing with rigid

pads is up to 19% larger than that with the softest pads ($k_{pad}=4.1$). For the LBP TPJB, pad flexibility reduces the damping coefficients by up to 15%.

Figure C.7 shows the dimensionless virtual mass coefficients (m) of the TPJB versus Sommerfeld number (S). A negative virtual mass indicates the bearing becomes stiffer as the excitation frequency increases ($\text{Re}(Z)=K-M\omega^2$). Increasing the pad flexibility tends to reduce the magnitude of bearing virtual mass coefficients, in particular at $S>0.8$.

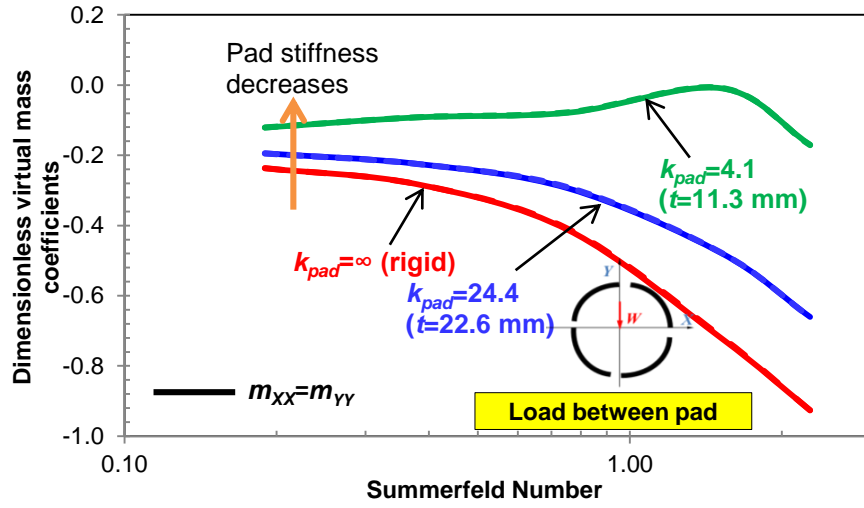


(a) LBP

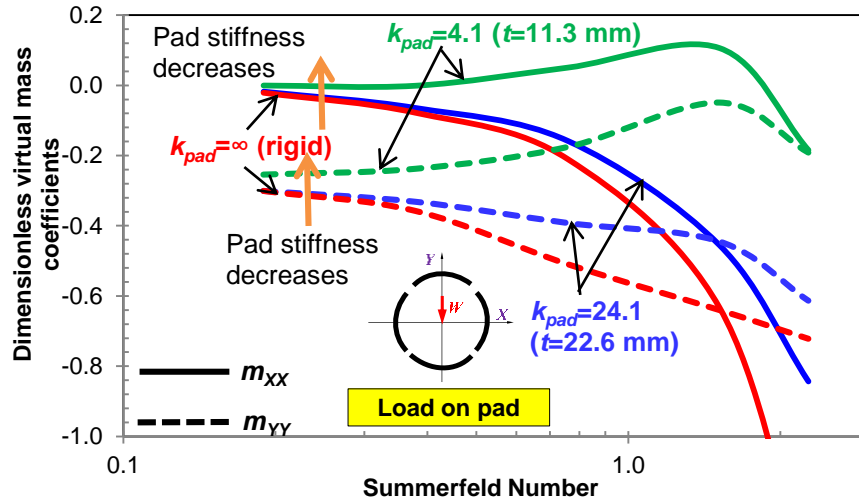


(b) LOP

Fig. C. 6 Four-pad TPJB dimensionless damping coefficients (c_{XX} and c_{YY}) vs. Sommerfeld number (S). Pad stiffness $k_{pad} = 4.1, 24.4, \infty$ (rigid) and pivot stiffness $k_{piv} = 8.0$. Pad preload $\bar{r}_p = 0$. LBP and LOP configurations. Specific load $W/(LD) = 1,239$ kPa, rotor speed $\Omega = 500$ rpm to 6,000 rpm.



(a) LBP



(b) LOP

Fig. C. 7 Four-pad TPJB dimensionless virtual mass coefficients (m_{xx} and m_{yy}) vs. Sommerfeld number (S). Pad stiffness $k_{pad} = 4.1, 24.4, \infty$ (rigid) and pivot stiffness $k_{piv} = 8.0$. Pad preload $\bar{r}_p = 0$. LBP and LOP configurations. Specific load $W/(LD) = 1,239$ kPa, rotor speed $\Omega = 500$ rpm to 6,000 rpm.

Closure For a four pad TPJB, pad flexibility shows little effect on the journal eccentricity and drag friction coefficient. The journal eccentricity (e/C_p) for the LBP bearing is larger than that for the LOP bearing at a small Sommerfeld number ($S < 1.0$). The maximum pad deformation at the leading and trailing edges (u_{max}) increases with the Sommerfeld number and is up to 36% of the cold pad clearance (C_p).

At the largest Sommerfeld number, the most loaded pad (#1) for the LOP bearing has the largest pad surface deformation. For the LBP bearing, the loaded two pads have the same pad surface deformation due to geometric symmetry.

Pad flexibility has a more pronounced effect on the dynamic force coefficients for the LOP bearing. The stiffness coefficients for the bearing with the softest pads ($k_{pad}=4.1$) are up to 14% smaller than those with rigid pads. At the largest Sommerfeld number, pad flexibility reduces the damping coefficients by up to 19%.